Universidade de Aveiro Departamento de Química
Ano 2024

Guilherme Brígido Rosa

Study of structure and properties of zeolites: 2D layered surfactant templated zeolites and EFAL species in H-ZSM-5 materials.

Estudo da estrutura e propriedades de zeólitos: zeólitos 2D lamelares e espécies EFAL em H-ZSM-5.

Universidade de Aveiro Departamento de Química
Ano 2024

Guilherme Brígido Rosa

Study of structure and properties of zeolites: 2D layered surfactant templated zeolites and EFAL species in H-ZSM-5 materials.

Estudo da estrutura e propriedades de zeólitos: zeólitos 2D lamelares e espécies EFAL em H-ZSM-5.

Dissertação apresentada à Universidade de Aveiro para cumprimento dos requisitos necessários à obtenção do grau de Mestre em Química, realizada sob a orientação científica do Doutor Paulo Claro, Professor associado com agregação do Departamento de Química da Universidade de Aveiro e da Doutora Mariana Sardo, investigadora auxiliar do Departamento de Química da Universidade de Aveiro.

Apoio financeiro do European Research Council (ERC), grant agreement 865974 no âmbito do programa Horizon 2020.

agradecimentos

No decorrer deste ano diversas pessoas contribuíram de forma direta ou indireta para o sucesso do trabalho apresentado nesta tese, sendo impossível de as enumerar todas. Começando pelas contribuições mais diretas, gostava de agradecer ao Professor Paulo Claro, por ter aceitado ouvir um aluno desconhecido que lhe foi bater à porta à procura de um projeto de licenciatura. Desde aí que me tem acompanhado e cultivado o meu interesse por tudo o que envolva espetroscopia e cálculos ab initio. Gostaria de agradecer também à professora Mariana Sardo, que de maneira semelhante, me abriu o seu gabinete para me convidar a expandir o meu horizonte a zeólitos e ao mundo do RMN de sólidos. Muito obrigado por toda a ajuda e acompanhamento prestado ao longo deste ano. De seguida tenho de agradecer a todo o pessoal da Team Specko, por me terem aceitado de braços abertos e prestado auxílio e conselhos sempre que preciso, especialmente na aquisição de espetros de RMN. Não poderia deixar de agradecer à Maria Celeste, que me ensinou a pôr as mãos na "massa" na parte da aquisição de espetros de infravermelho. Deixo também um enorme agradecimento à Dra. Mariya Shamzhy e o seu grupo de investigação, pela oportunidade incrível. Por mais curta que tenha sido a minha estadia, teve um impacto enorme na minha experiência científica e pessoal. Deixo um especial obrigado ao Dr. Martin Kubů, que me acompanhou e aconselhou diariamente ao longo de todas as sínteses e caracterizações feitas. Queria também agradecer pessoalmente ao Dr. Carlos Bornes, que me aconselhou ao longo de todo o ano tanto na área de zeólitos e futuro académico, como os melhores sítios a visitar em Praga e arredores. Não poderia deixar de agradecer a toda a minha família, em especial aos meus pais e irmão. Mesmo passando pouco tempo em casa, sempre de volta dos meus "hieróglifos", nunca me deixaram de apoiar e tranquilizar nas alturas mais difíceis. Por último, agradeço também aos meus amigos. Por mais que eu goste de química é sempre bom saber que neles tenho uma segunda casa sempre que preciso.

o júri

president

Doutora Maria do Amparo Ferreira Faustino
Professora Associada do Departamento de Química da Universidade de Aveiro

vogais

Doutor Carlos Bornes
Investigador do Department of Physical and Macromolecular Chemistry, Charles University Prague

Doutor Paulo Jorge de Almeida Ribeiro Claro
Professor Associado com Agregação do Departamento de Química da Universidade de Aveiro

palavras-chave

Zeólitos bidimensionais, Espécies EFAL, Espectroscopia vibracional, RMN do estado sólido, Química computacional

resumo

O objetivo principal desta tese de Mestrado foi a abordagem de algumas questões em aberto relacionadas com a estrutura e propriedades de zeólitos, recorrendo a várias técnicas de caracterização e dados experimentais anteriormente disponíveis referentes aos sistemas em estudo. Para este fim, duas linhas principais de pesquisa foram definidas. A primeira envolvendo a síntese de zeólitos 2D lamelares e os correspondentes gemini SDA bifuncionais com 3, 4 e 5 grupos amónio. Os materiais foram caracterizados por difração de raios-X para determinar a estrutura e por adsorção de nitrogénio para avaliar as suas propriedades texturais. A segunda linha de investigação foi o estudo de espécies EFAL em zeólitos do tipo H-ZSM-5. Para tal, amostras com diferentes graus de dealuminação foram analisadas recorrendo a espectroscopia vibracional (infravermelho e INS) e a RMN do estado sólido, para perceber o efeito dos vários tratamentos nas amostras, com um especial foco nas espécies EFAL formadas, assim como a sua estrutura. Toda esta análise foi suportada por simulações de teoria do funcional da densidade, para melhor relacionar os vários sinais e as suas variações com a entidade atómica correspondente.

keywords

Two dimensional zeolites, EFAL species, Vibrational spectroscopy, Solid-state NMR, Computational chemistry

abstract

The aim of this Master thesis was to address a few of the open questions related with the structure and properties of zeolites, utilizing a plethora of techniques and previous experimental data available on the target systems. For this purpose, two main research goals were established. The first is related with the synthesis of 2D layered surfactant templated zeolites and the corresponding gemini bifunctional structure directing agents with three, four and five ammonium groups. The materials were then characterized by X-ray diffraction for structure determination and nitrogen physisorption for textural properties. The second goal involves the study of EFAL species in H-ZSM-5 zeolites. For this purpose, samples with differing degrees of dealumination were analysed by vibrational spectroscopy (infrared and INS), as well as by solid-state NMR to attempt a better understanding of the effect of various sample treatments, with a special focus on the generated EFAL species and their possible structures. This was aided by density functional theory simulations to better correlate signals and their variations to their corresponding atomic moieties.

reconhecimento do uso de ferramentas IA

Reconhecimento do uso de tecnologias e ferramentas de Inteligência Artificial (IA) generativa, softwares e outras ferramentas de apoio.

Não foram utilizados no presente trabalho quaisquer conteúdos gerados por tecnologias de IA. Foram utilizados os softwares: Office365 (Microsoft, https://www.office.com) para a escrita do texto e representação de tabelas; TopSpin para a análise de espetros de RMN; CASTEP e Gaussian 16 para optimizações de estruturas e cálculo de espetros; Mantid para simulação de espetros INS; Chemcraft para visualizar estruturas e respetivos espetros de infravermelho; Jmol para a visualização de modos vibracionais em ficheiros .phonon; Origin para a representação de espetros e Chemsketch para ilustrar estruturas moleculares.

List of contents

List of Figures

List of Tables

Glossary

1D	one-dimensional.
2D	two-dimensional.
AO	atomic orbital.
B3LYP	Becke 3-parameter Lee-Yang-Parr.
CSA	chemical shift anisotropy.
DFT	density functional theory.
DPE	deprotonation energy.
DRIFTS	diffuse reflectance infrared Fourier transform spectroscopy.
EFAL	extra-framework aluminium.
FAAL	framework associated aluminium.
GTO	Gaussian type orbital.
H_0	Hammett acidity function.
HF	Hartree-Fock.
INS	inelastic neutron scattering.
K_a	acid dissociation constant.
MAS	magic angle spinning.
MP	Møller-Plesset.
NMR	nuclear magnetic resonance.
SDA	structure directing agent.
Si/Al	silicon to aluminium ratio.
SSNMR	solid-state nuclear magnetic resonance.
STO	Slater type orbitals.
TBPO	tributylphosphine oxide.
TMPO	trimethylphosphine oxide.
TRAPDOR	transfer of population in double resonance.
HZSM-5	H exchanged Zeolite Socony Mobil-5.
XRD	X-ray diffraction.
ICP-MS	inductive coupled plasma mass spectroscopy.
FTIR	Fourier transform infrared.
SEM	scanning and transmission electron microscopy.
TEM	transmission electron microscopy.

1. Introduction

1.1. Economic impact and applications of zeolites

Alex Fredrik Cronstedt first discovered zeolites in 1756, naming this material from the combination of the Greek words ‘zein’ (to boil) and ‘lithos’ (rock), as he observed that upon heating, the water inside them would bubble and boil leaving it as steam, giving the “illusion” that the mineral was boiling [1]. Not much research was performed on these materials for many years, being labelled as mere curiosities of not much scientific or practical interest, which is in complete contrast to the current reality [1].

In 2021 the global market size for zeolites was valued at 12.6 billion USD, with an expected annual growth around 6.2% until 2030 [2]. Looking at its current market revenue share, some of the more relevant applications are as detergent builders, where they allow the capture of ions responsible for water hardness or as adsorbents in various fields, with one of the most well-known being as pet litters for urine adsorption [2]. But by far, representing 47% of the total revenue, their application as catalysts is their most important role, especially as cracking and hydrocracking catalysts in the ever-growing petrochemical industry [2]. However, with the recent global push towards sustainability, research on new applications of zeolites has been on the rise. Their adsorption and ion exchange capabilities has led to their use in the retention of greenhouse gases, namely CO_2, and in water treatment and soil remediation, by adsorption of dyes, heavy metals and other recalcitrant pollutants [3]. An energy alternative for fossil fuels are biofuels, such as bioethanol and biodiesel and just as in fossil fuel production, zeolites are used as acid catalysts for biofuel synthesis. However, the chemical composition of the feedstock in both cases is distinct: while fossil fuels are derived from hydrocarbons, biofuels mainly come from carbohydrates and triglycerides, meaning the physiochemical properties of the zeolites need to be tuned differently to achieve maximum efficiency [3], [4].

All these applications are possible due to the various characteristics of these versatile materials, and so a deeper understanding of their structure and properties is vital for the optimization of current zeolites and the design of new and improved ones.

1.2. Structure and characterization of zeolites

Zeolites are aluminosilicate crystalline 3D frameworks, that possess the general formula: $\mathbf{M_{x/n}(AlO_2)_x(SiO_2)_y.wH_2O}$. **M** is the extra-framework cation with charge n, needed to counterbalance the framework's negative charge (concept developed ahead). **y/x** is the Si/Al (silicon to aluminium) ratio, while **w** is the number of water molecules residing inside the structure [3], [5].

The building blocks of these materials are TO_4 tetrahedra, illustrated in **Figure 1** (left), where T can either be Si^{4+} or Al^{3+}, which connect with each other by establishing covalent bonds through one shared oxygen atom. This limitation leads these corner sharing tetrahedra to form highly ordered structures, characterized by the presence of molecular size pores (usually between 0.4-1.3 nm), as seen in **Figure 1** (middle), which can be classified by the size of the n-rings defining them. The n-rings result from the tetrahedra binding to one another forming a "circle", although its shape can be distorted, where **n** is the number of TO_4 units. Small-pore zeolites have up to 8/9 membered rings; medium pore zeolites have up to 10 membered rings; large pore zeolites have 12 membered rings; and extra-large pore zeolites have membered rings with more than 12 TO_4 units [3], [5], [6].

Other important features of these structures are: **cages**, polyhedral structures with small enough pores (less than 6 membered rings) where only very small molecules such as water can enter; **cavities**, larger than cages, allowing bigger molecules to enter; and **channels**, which are the same as cavities, but extend along 1 dimension, enabling molecules to travel along them, and that can intersect with each other to form 2/3-dimensional systems, with one example in **Figure 1** (right) [3], [5].

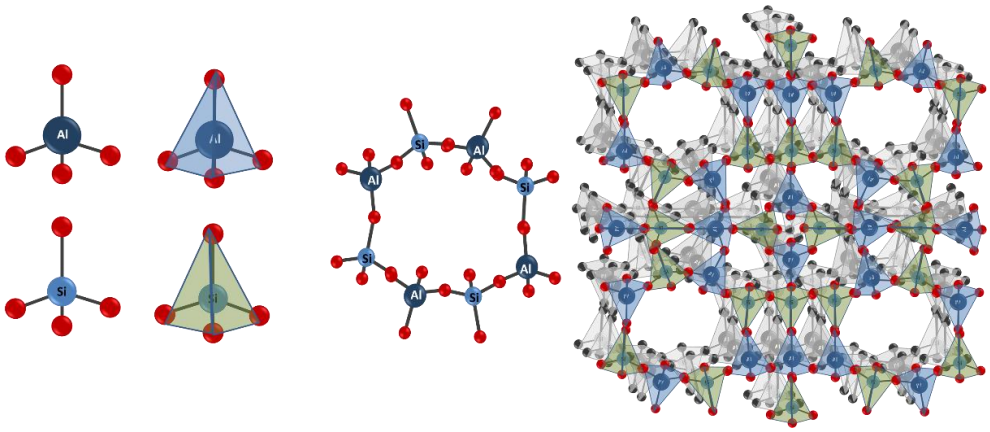

Figure 1. Building blocks of zeolite structures and their assembly: zeolitic tetrahedra bond to each other (left) forming n-membered rings (centre), whose association with each other forms the 3D crystalline structure (right). Adapted from [7].

All the features described give zeolites their molecular sieve properties, with smaller molecules being able to traverse the pores and enter the structure, while bigger ones are unable to enter. Compounds inside the structure can then establish interactions with the zeolite, either through van der Waals forces, becoming physiosorbed, or form chemical bonds, becoming chemisorbed, enabling various of the previously mentioned applications, like the removal of pollutants from liquid effluents.

The Si/Al ratio is extremely important, influencing several physicochemical properties of these materials. Among other synthesis conditions like temperature and time, this ratio influences the 3D structure of the resulting zeolite, allowing to tune pore volume, channel dimensionality, etc for the target application [3]. Zeolites can even be classified based on their silicon content, with Si/Al ratios higher than 5 yielding silicon rich zeolites, generally characterized by being hydrophobic and presenting high hydrothermal stability, while Si/Al ratios lower than 5 yield aluminium rich structures, which are highly hydrophilic, exhibit lower hydrothermal stability and have a higher cationic content [3], [5]. One of the limitations of these materials is that Al-O-Al arrangements are forbidden, through the so called Löwenstein rule, which forbids Si/Al ratios lower than 1 [8]. This is a topic of debate within the scientific community since some computational studies seem to have found exceptions to this rule, although they needed to be performed in anhydrous conditions, disregarding both cation solvation and hydrothermal synthesis conditions [8]. Since no zeolite with Si/Al < 1 has been observed experimentally, the general consensus is that Al-O-Al arrangements have not been observed [5].

Another vital aspect of zeolites is that while Si has a charge of +4, Al has a charge of +3, and so, for every Al tetrahedra, a negative charge is “added”, originating a negatively charged framework. This charge needs to be balanced by extra-framework cations, which can range from alkali, alkaline earth and alkylammonium, to ammonium cations and protons (H^+), residing in the channels, cavities and cages of the structure [3], [5]. This enables ion-exchange that in conjunction with adsorption allows, for example, the removal of ions responsible for water hardness when washing clothes.

The only other major property of zeolites yet to mention, is their acidity which is arguably one of the most important, since it is responsible for most of zeolite’s catalytic abilities.

1.3. Acidity in zeolites

1.3.1. Type of acidity

Nowadays there are two major concurrent theories used to describe acidic behaviour. In Bronsted's theory, an acid is defined as a species capable of releasing a proton, acting as a proton donor, while a base must have a free pair of electrons to share and capture a proton, acting as a proton acceptor [5], [6]. Thus, an acid-base reaction relies on a proton transfer, represented by the equation bellow:

$$HA + B \rightleftharpoons A^- + HB^+ \qquad (1)$$

$$Acid + Base \rightleftharpoons Conjugate\ base + Conjugate\ acid \qquad (2)$$

Concurrently, Lewis presented his own theory based on the compound's electronic properties, instead of its chemical composition. According to Lewis, an acid is any species capable of accepting an unshared pair of electrons on an empty orbital, acting as an electrophile, while a base must have a free pair of electrons to donate and form a covalent bond with the acid, acting as a nucleophile [5], [6]. In this case, the acid-base reaction can be represented by the equation:

$$A + \bar{B} \rightarrow A - B \qquad (3)$$

Lewis' theory encompasses Bronsted acid-base theory, where a Lewis base is also a Bronsted base, however a Bronsted acid is the result of a reaction between a Lewis base and acid, not being an acid itself. In fact, not only is the H^+ the acid in Lewis's theory, but it is one single example of a much larger group encompassing any cation and molecule containing atoms with incomplete octets or that can change their valence shell to accept an electron pair [5], [6]. Nevertheless, Bronsted's theory is very useful, and so both are commonly used, denoting which type of acidity is mentioned (either Lewis or Bronsted) when relevant as to not cause confusion. Because of this, zeolite acidity may be analysed based on both theories.

1.3.2. Origin of acidity

If these materials didn't contain any aluminium, there wouldn't be any charge imbalance, as is the case of silicalite, with chemical formula SiO_2. However, because there is a substitution of Si^{4+} by Al^{3+}, the framework becomes negatively charged and needs to be neutralized by extra-framework cations, usually metal cations, as mentioned in the previous section. This enables the introduction of Bronsted acidity in zeolites, by having H^+ stabilize

the framework. They can be inserted in various ways, normally involving post-synthesis modifications: direct proton-exchange of the metal cations; ammonium-exchange of the metal cations followed by calcination to decompose the ammonium into ammonia, which abandons the structure, and leaves the H^+ to attach to the surface; exchange with specific polyvalent cations that can produce protons via water hydrolysis; and exchange with specific metal cations that can oxidize hydrogen to generate protons [6]. These protons bond to the bridging oxygens connected to the aluminium, forming a bridging hydroxyl group as seen in **Figure 2**, the main source of Bronsted acidity and many of the catalytic capabilities of these materials.

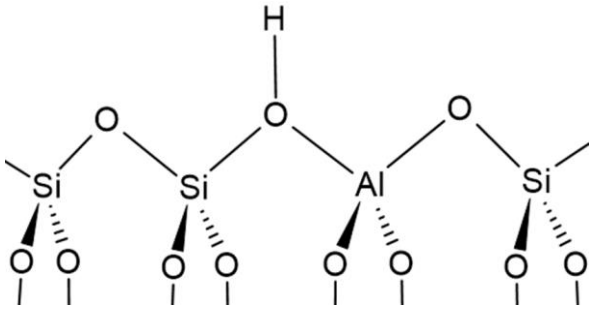

Figure 2. Bridging hydroxyl group's structure.

Lewis acidity in zeolites can also be achieved through various means. Isomorphic substitution of Si or Al by either titanium, vanadium, niobium, tin and zirconium; ion-exchange of extra-framework polyvalent cations or multiply-charged cations allows these species to act as Lewis acids [5], [6], [9]. However, by far the most studied Lewis acidity in these materials is that coming from aluminium species [5], [6], [9]. Even though Lewis acidity arising from aluminium species has been the focus of many studies, it still represents a grey area that isn't fully understood, with multiple possible structures with distinct nature contributing towards acidity. They are generated through post-synthesis treatments such as calcination, steaming (calcination at high temperatures in the presence of steam) or acid leaching [5], [6], [9]. The species generated from these treatments can generally be divided in three groups, extra-framework aluminium (EFAL), framework associated aluminium (FAAL) and framework aluminium [9].

EFALs are the most studied Lewis acid sites, and are defined as aluminium species that are completely separated from the zeolitic framework [5], [6], [9]. They are formed through the dealumination process, where Si-O-Al bonds are ruptured at elevated temperatures, releasing the aluminium from the framework. Although acid leaching causes dealumination, it also drag out the majority of the aluminium removed during the process,

and so steaming is the preferred method, since it bypasses this issue [5], [9]. The specific nature of these compounds is still a topic of study, not only dependent on the post-synthetic conditions (temperature, time, method, etc), but also on the zeolite, varying with its Si/Al ratio, structure, etc [9]. These species have distinct chemical natures and coordination, which is exemplified in **Figure 3**, with some suggestions being $Al(OH)^{2+}$, $Al(OH)_2^+$, AlOOH, Al_2O_3, $Al(OH)_3$, $Al(OH)_3(H_2O)_3$, $Al(OH)_2(H_2O)_3^+$, $Al(OH)(H_2O)_3^{2+}$, $Al_3(OH)_6^{3+}$, and other multinuclear clusters [5], [9].

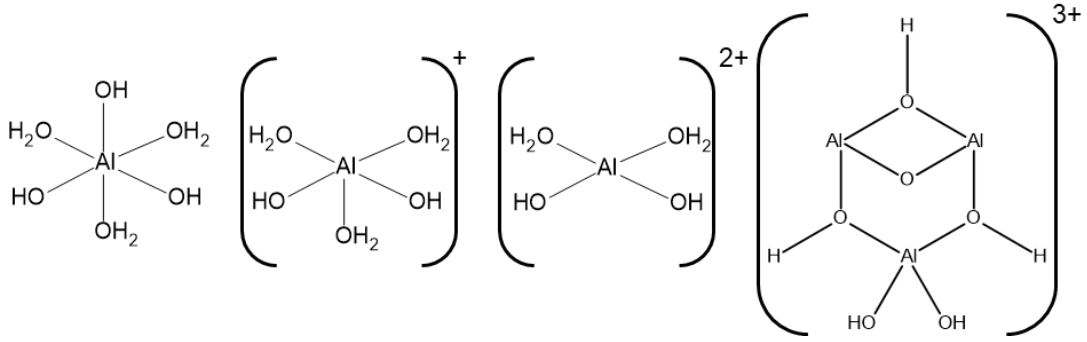

Figure 3. Proposed structures of some EFAL species, recreated from reference [9].

Thanks to the heterogeneity of EFALs, it is important to keep in mind that not only different species have distinct acid strength, but also that some EFALs may not even behave as Lewis acids at all, as is often assumed. As such, a direct correlation between the number of EFALs and the materials' acidity shouldn't always be taken for granted, and thorough studies to identify and characterize the specific species present are required [9].

By submitting the zeolite in its proton form to high temperatures, some of the tetrahedral aluminium is partially removed from the framework, not being entirely dislodged from it, forming framework associated aluminium [9]. They can then revert into fully associated aluminium by converting the zeolite into its ammonium form, losing their Lewis acidity. This allows the distinction between EFALs and framework associated aluminium, since if the zeolite is submitted to high temperature dehydration/conversion to ammonium form, the NMR (nuclear magnetic resonance) signal corresponding to EFALs will remain mostly unchanged, while the signals corresponding to framework associated aluminium will appear and disappear because of its reversible octahedral/tetrahedral coordination [9].

Finally, framework associated aluminium is the most poorly understood, although there are reports of its detection [6], [9]. Pre-existing defects in the framework, or defects caused by dehydration at high temperatures can dehydroxylate the Bronsted acid sites, allowing the now three-coordinated aluminium to act as a Lewis base [6], [9].

1.3.3. Studying acidity

All chemists are familiarized with evaluating the strength of a Bronsted acid in the liquid-phase, determined either by the dissociation constant (K_a) or by the Hammett acidity function (H_0). The acid interacts with the solvent, usually water, protonating it to generate H_3O^+, which is the major player in water-phase acidity, with the concentration of this species being dependent on acid concentration and on the acid's intrinsic strength, its tendency to release the proton. Homogeneity is guaranteed, since all acid molecules of the same "species" are equal, and are expected to be in equivalent environments while in solution [5], [6].

The behaviour is very different for solid-phase zeolites. First, there are different acid species present with distinct acid strengths, that can have different natures (Lewis vs Bronsted), meaning their distinct acid strength must be considered and cannot be generalized. This is exacerbated by the fact that since these are solid materials, they aren't usually in contact with a solvent, and therefore interact directly with the "base of interest", instead of the reaction being mediated mainly by water [5], [6]. Lastly, but very important, is the fact that, because of zeolite geometries, the acid sites are in distinct environments, ranging from being confined to a small cage, to being inside a large channel. This is very important as it influences the accessibility of molecules to these sites, with acid strength being irrelevant if the molecules can't reach the acid moieties. It also influences the environment of the acid site, leading to different interactions with the zeolitic framework, of both the acid and the reacting molecule [5], [6]. With all these caveats in mind, two distinct approaches to evaluate acid strength are considered: intrinsic and apparent acid strength.

1.3.4. Intrinsic acid strength

In this approach, only the tendency of the acid to release the proton is evaluated, as to establish an objective strength value for the acid site. The most clear-cut metric is the deprotonation energy (DPE), defined as the energy needed to separate the proton from the conjugated acid (**Figure 4**), meaning it depends solely on the acid strength. However, this constant can't be determined experimentally, and can only be estimated through computational methods by calculating the energy difference between the isolated zeolite base and proton in relation to the conjugated zeolite acid [5].

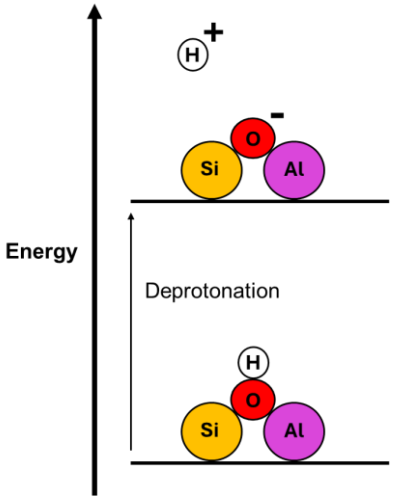

Figure 4. Energy diagram of Bronsted acid site deprotonation, inspired by [5].

Some earlier computational studies utilizing semiempirical methods suggested that higher Si-O-Al angles lead to stronger acidity by weakening the O-H bond, but later and more accurate Hartree-Fock and density functional theory (DFT) methods refuted this assumption [5], [6], [10].

Experimental approaches to evaluate intrinsic acid strength involve measuring the vibrational spectra or NMR chemical shifts of the bridging hydroxyl groups [5], [11]. In the case of vibrational spectra, the stronger the O-H bond (weaker acid strength) the higher its stretching frequency will be. When analysing the NMR spectra, higher ^{1}H chemical shifts of the bridging hydroxyl group are associated with stronger Bronsted acidity, and vice-versa. This analysis has some problems, namely, the influence of extra-framework species or hydrogen bonds between the zeolitic framework and these groups, shifting their vibrational frequencies and chemical shifts [5], [11]. This is exemplified in a study using a H-MFI zeolite representative, where two distinct ^{1}H chemical shifts and O-H stretching frequencies could be observed for free and for bridging hydroxyl groups establishing hydrogen bonds with the zeolitic framework. The higher stretching frequency and lower chemical shift corresponded to the free OH group, while the lower stretching frequency and higher chemical shift corresponded to the bonded OH group, meaning a reliable acid strength scale can't be set based on these bands and peaks, since the presence or absence of an interaction with the acid site can't always be guaranteed [5], [11].

1.3.5. Apparent acid strength

Even though intrinsic acidity is a useful metric, it gives an incomplete view of the acid-base reaction by only considering the acid moiety. Apparent acidity evaluates the full acid-base process, from the encounter of the acid and the base, up to the stabilization of the products. Because of its nature, apparent acidity studies use probe molecules, which are bases of varying strength that interact with the acid sites. One parameter that can be evaluated by apparent acidity is the accessibility of the acid site. This is done by utilizing a molecule of similar size to the compounds we want our zeolite to catalyse, allowing the probe to only interact with the acid sites the compounds themselves would be able to reach [5]. The use of probe molecules also enables a more complete view of the thermodynamic cycle resulting from an acid-base reaction illustrated in **Figure 5**. The initial step is the previously mentioned deprotonation of the acid site, followed by the protonation of the base. The higher the proton affinity of the base, the more readily it will accept the proton, represented by a higher absolute value of the energy released during this interaction, the protonation energy [5]. The final step is the stabilization of the conjugate acid through van der Waals forces and electrostatic interactions, not only with the newly formed conjugate base, but also with the surrounding framework. The stabilization is thus dependent on the nature of the base and on the framework surrounding it, both playing a heavy role on the selectivity and extension of the interaction between the molecule and the acid site, with stronger interactions being associated with higher absolute values of energy released during this step [5]. The reactions' extent and selectivity are also affected by stabilization of the reaction intermediaries by the zeolitic framework.

As can be seen, while intrinsic acidity only evaluates the acid site's strength, apparent acidity, by using probe molecules, also considers site accessibility, the properties of the basic molecule, and their interaction with the zeolitic structure.

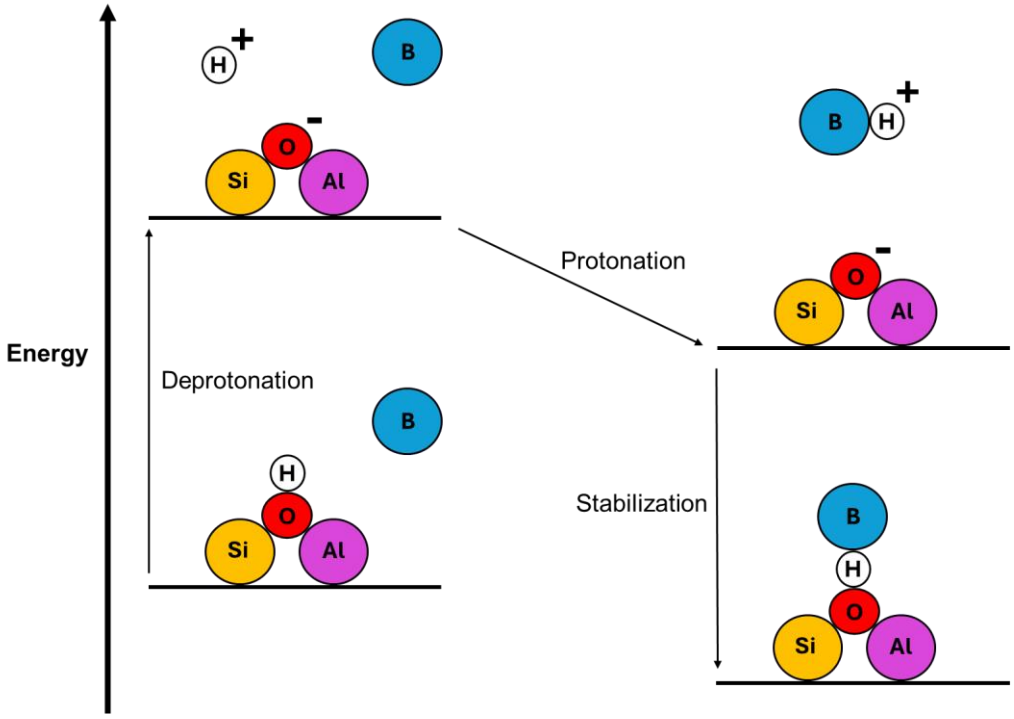

Figure 5. Full thermodynamic cycle of the acid-base reaction between a zeolite's Bronsted acid site with a basic probe molecule, represented in blue as B, inspired by [5].

1.3.6. Probe molecules

There are various factors to consider when selecting a probe molecule. We want it to only interact with the zeolite's acid sites, while being able to identify if they are Lewis or Bronsted, and if they have distinct apparent acidity. Normally we also want to select a compound similar to the reactant molecule for the intended zeolite application, both in size and reactivity. Different molecules offer different advantages and disadvantages, leading to the use of distinct species depending on the situation, such as ammonia, alkylamines, pyridine, ketones, alkylphosphines and alkylphosphine oxides [5].

Techniques such as adsorption calorimetric studies and temperature programmed desorption measure the enthalpy associated with the probe molecule adsorption and desorption respectively, although they can't breakdown the energetic contributions of each individual step [5]. On the other hand, vibrational (infrared, Raman, inelastic neutron scattering, etc) and NMR spectroscopy evaluate the changes in the adsorbed molecules' and active sites' spectra, resulting from changes in the vibrational modes and chemical shifts of the species involved in the adsorption process [5].

One specific example of the power of probe molecules is their use in the study of the distribution of internal and external acid sites. In two separate studies of HZSM-5, two different techniques, solid state NMR (SSNMR) and infrared spectroscopy, were used for this purpose [12]–[14]. Their basis is that smaller probes, such as pyridine (represented in **Figure 6ai**) and trimethylphosphine oxide (TMPO, represented in **Figure 6bI**) respectively, are small enough to travel along the zeolite's pores, not being able to discriminate between internal and surface acid sites. Their substituted versions on the other hand, 2,4,6-trimethylpyridine (or 2,4,6-collidine, represented in **Figure 6aii**) and tributylphosphine oxide (TBPO, represented in **Figure 6bII**) respectively, are large enough that their access to the framework structure is limited, only being able to interact with the surface external acid groups, allowing to distinguish their signal from internal acid groups. Both studies exploit this fact, which is seen in the spectra in **Figure 6** [12]–[14]**.**

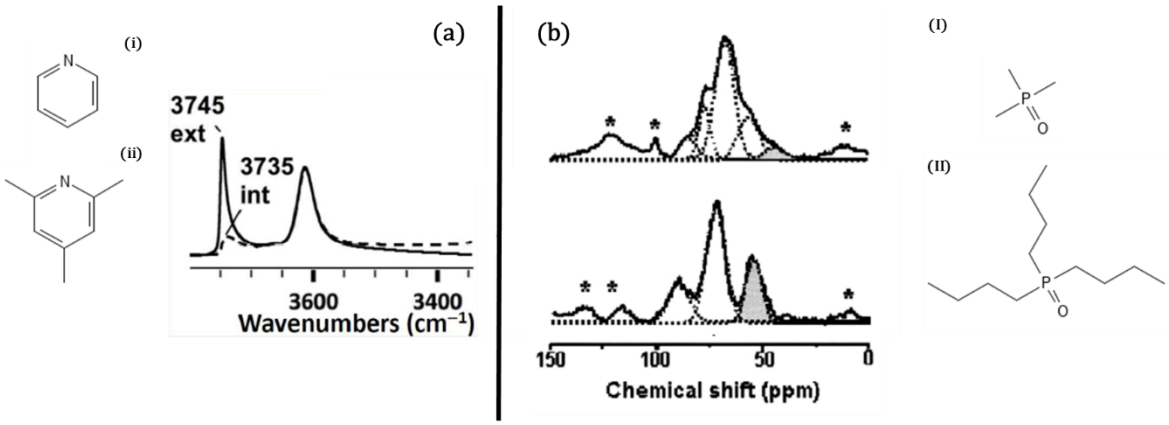

Figure 6. Study of HZSM-5 internal and external acid sites using probe molecules. (a) infrared spectra, with the full line representing the spectrum of probe free HZM-5, while the dashed line represents HZSM-5 loaded with 2,4,6-collidine (structure ii). Adapted from [12]. (b) ^{31}P MAS NMR spectra are represented, where the top spectrum is from HZSM-5 loaded with TMPO (structure I), while the bottom spectrum is from HZSM-5 loaded with TBPO (structure II). Adapted from [13], [14].

In the infrared study (**Figure 6a**) the full line represents the spectra of "pure" HZSM-5, containing two bands, one at around 3610 cm^{-1} corresponding to bridging hydroxyl groups, which are contained within the structure. The band at 3745 cm^{-1} corresponds to external silanol groups, and it presents a shoulder at 3735 cm^{-1}, arising from internal silanol nests. These are framework defects where metal removal (Al or Si) inside the framework results in the formation of silanol groups establishing a hydrogen bond network with each other. The dashed line represents the infrared spectrum of HZSM-5 loaded with 2,4,6-

collidine, and some obvious changes can be seen. The bands around 3610 cm^{-1} and 3735 cm^{-1} remain unchanged, as the large molecule couldn't reach these internal sites, while the external silanol bands' intensity decreased dramatically due to its interaction with collidine [12].

In the NMR study (**Figure 6b**), the signal of ^{31}P from the probe was measured, instead of directly measuring the signal from the acid group, as was done previously, however, similar results are achieved. The top spectrum is from HZSM-5 loaded with TMPO, which exhibits 5 peaks associated with interaction of the probe with acid sites. The bottom spectrum is from HZSM-5 loaded with TBPO, which only exhibits 3 peaks, which correspond to external acid sites, while the two missing peaks are from internal sites [14].

1.4. Tailoring transport and textural properties of zeolites

Until now the focus has been on typical 3D zeolites characterized by their well-defined microporosity (pores < 2 nm), and their regular rigid structures, making them ideal as molecular sieves and shape selective catalysts for small molecules [15], [16]. However, these advantages also have problems associated. When the reagents' or their products' dimensions start to enter the mesopore region (bigger than 2 nm) they are either unable to enter the zeolitic structure or once inside present very long diffusion times [16]. Another issue is that zeolite structure modification is very difficult, especially post synthesis. While there are more than 200 different recognized structures, the differences between them are minor when compared to the wide range of modifications available with other materials, from expansions and tunning of pore dimensions to formation of intricate composites [15].

This has motivated research into tailoring zeolites' textural and transport properties, with three main routes to achieve this (**Figure 7**): reduction of crystallite size, originating nanozeolites; introduction of mesoporosity, generating hierarchical zeolites; synthesis of lamellar structures, forming 2D zeolites [15]–[17].

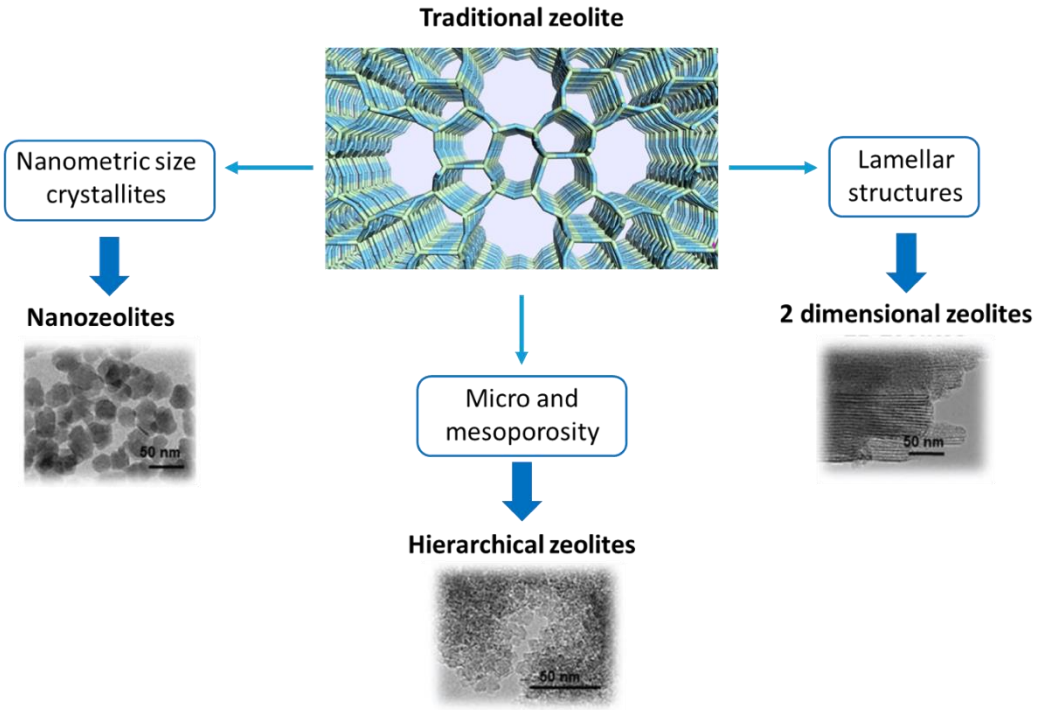

Figure 7. Approaches to tailor zeolites' textural and transport properties. Adapted from [16].

Nanozeolites are obtained in a similar process to the one traditionally used for their 3D counterparts, where gels containing aluminium and silicon sources, water, alkali cations

and organic structure directing agents (SDA) react under hydrothermal conditions, in the range of 60-200ºC, under basic pH and autogenous pressure. The aluminium and silicon sources provide the Al and Si necessary for the structure, the basic conditions ensured by the mineralization agents (usually NaOH or KOH) increase the solubility of the precursors and promote T-O-T bond formation and the SDA functions as a nucleation site that promotes the formation of micropores [16].

The distinction for nanozeolites is that nucleation is favoured over crystal growth, creating more growth centres which limits their final size, allowing for the formation of nanometric crystallites (smaller than 100 nm) [16]. This can be achieved by utilizing clear solutions or gels containing zeolite precursors as the reaction mixture, while at a lower synthesis temperature. The use of an excess of organic structure directing agents and a reduction in the alkali cation content also favours nanosized particles [16]. The main advantages of these materials are the increased external surface area leading to an increase in the ratio of external to internal active sites, increasing the number of sites available to bulky molecules that are unable to enter the zeolite. Another one is the decreased in the diffusion paths taken by molecules, which is advantageous for compounds that can enter or are formed inside the zeolite, but whose bulk leads to slow mass transport [16]. These are also used as precursors for the synthesis of membranes, composites, films and hierarchical structures, with various applications, from heterogenous catalysts to chemical sensors [16].

Hierarchical zeolites possess the typical zeolitic micropore system alongside a second pore size distribution which is usually in the mesopore range [16]. There is a multitude of ways these materials can be prepared, being divided into top-down and bottom-up approaches [16]. In the top-down approaches traditional 3D zeolites are treated post-synthesis to generate the mesopores. The typical example is dealumination, which by removing aluminium from the framework through steaming originates some mesoporosity [16]. In the bottom-up approach the mesopores are introduced during the synthesis process. One such method is the addition of certain polymers to the reaction mixture, which will then act as the mesoporous structure directing agent, alongside the typical microporous structure directing agents [16]. The presence of the mesopores enables the accessibility of bulkier molecules to the zeolite interior, while also increasing the overall mass transport of molecules. They also provide an ideal space for incorporating and grafting different components or phases such as metal oxides, allowing for great flexibility in the preparation of multifunctional materials [16].

1.4.1. 2D zeolites

A two-dimensional (2D) zeolite is defined by having crystallites in which one of its dimensions is less than a few nanometres thick, which corresponds normally to around one- or two-unit cells, having the shape of nanosheet layers [15]–[17]. These units are linked to each other not by covalent bonds, but by weak van der Waals forces or hydrogen bonds, which allows them to acquire a variety of arrangements while preserving the integrity of the original layers [15], [17]. These can them be further modified to not only increase their available arrangements, but also allow for intelligent chemical modifications.

The synthesis of these materials can be subdivided into 3 main approaches: direct hydrothermal synthesis of layered zeolite precursors; surfactant templated crystal growth; and the ADOR (assembly, disassembly, organization, reassembly) top-down approach [15], [16].

1.4.2. Synthesis and structure of 2D zeolites

Layered zeolite precursors

Just like many other branches in science, 2D zeolite precursors already existed and had been synthetized before their official discovery in the 1990s, with the existence of silicalite ilerite dating all the way back to 1964 [17]. The scientific community's interest in these materials really became cemented in 1990 with Mobil's discovery of the zeolite precursor of the MWW framework, MCM-22 (Mobil Composition of Matter) [15], [17].

When performing hydrothermal synthesis, thigh control of the synthesis conditions, namely the gel composition and the SDA used, allowed the formation of lamellar precursors, the layered zeolite precursors [15], [16]. For example, in MWW synthesis higher Si/Al ratios in alkaline mediums, roughly above 12, favour precursor formation, while lower ratios lead to the direct formation of the 3D form. This trend seems to be supported for other systems as most layered zeolites prepared in alkaline medium have a relatively high Si/Al ratio [15]. As such, it is proposed that surface Al atoms are majorly present in the $AlOH^-$ form, favouring the formation of Al-O-Si bonds, propagating the framework, while Si atoms are mainly present in the SiOH form, which is more favourable for crystallite growth termination [15].

The SDAs are not only inside the lamellar micropores, but also on the surface incomplete pores, intercalating the layers [15], [16]. Upon calcination the SDAs are removed and under these temperatures the surface silanols of distinct lamellar precursors condense into oxygen bridges, connecting the layers with the formation of tetrahedral silicon, although

as will be seen this doesn't always result in the formation of the traditional 3D zeolite [16]. As such there is a distinction between expanded and unexpanded structures, which can be detected with x-ray diffraction if the material is not dominated by intralayer reflections, as is the case of the MWW structure [15]. When looking at calcinated and non-calcinated structures without further modifications, three main arrangements are found as shown in **Figure 8**: ordered stacking, forming ordered multilayers; disordered staking, forming disordered multilayers and ordered staking with planes shifted in the ab plane [15], [16].

These forms only differ in their layer packing, and so it is expected that all other 2D zeolites can form these structures by control of the synthesis conditions [15]. However, of the 250 approved frameworks, only 20 have yielded precursor layered materials, of which the majority only presents three or fewer of these forms. As of now the discovery and arrangement of new 2D zeolites is mainly a trial-and-error process, with the hopes of finding rational solutions in the future [15], [16].

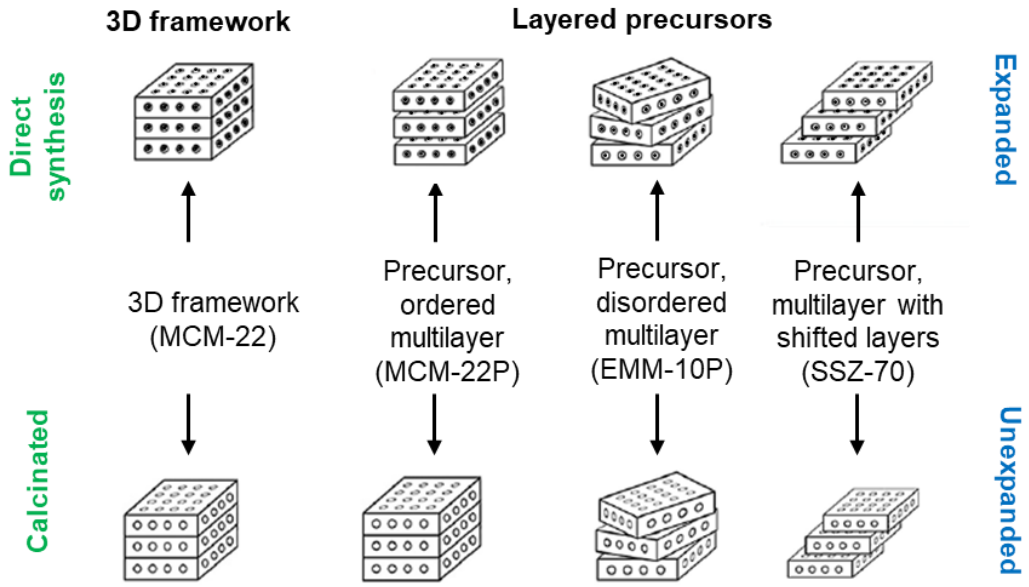

Figure 8. Layered precursors zeolite materials. Adapted from [15], [16].

Surfactant templated 2D zeolites

Finding the adequate synthesis conditions for the formation of layered precursors for different zeolites, if they even exist, is an arduous empirical process, which has been achieved for few structures [15], [16]. An alternative was first discovered in 2009 by Ryoo *et al.* with the use of a bifunctional structure directing agent (BSDA) to prepare lamellar forms of zeolites MTW and MFI [16], [18]. This BSDA was a multi-quaternary ammonium surfactant, where the hydrophilic head contains the ammonium groups separated by

organic bridges (C_6H_{12}), while the hydrophobic tail was a long hydrocarbon chain, with the structure of the original BSDA being $C_{22}H_{45}$-N^+($-CH_3$)$_2$-C_6H_{12}-N^+($-CH_3$)$_2$-C_6H_{13} ($C_{22\text{-}6\text{-}6}$) [15], [16], [18]. While the hydrophilic part fulfils the usual role of the SDA, filling and stabilizing the pore volumes, thus templating the crystallization, the hydrophobic one prevented crystal growth along one of the crystallographic directions (the b axis for MFI), thus forming layers instead of 3D structures [15], [16], [18]. It is important to highlight that while SDA are present in the surfaces of layered zeolite precursors, they do not stop the formation of the 3D structure by spacing the layers. The zeolite structure and reaction conditions simply allow for a pathway where the layers are formed without condensing, unless the sample is then calcinated. For surfactant templated zeolite, the presence of the BSDA is imperative, as the zeolitic layers would have condensed otherwise [15], [16].

Further investigation into the effects of the surfactants structure found that the minimum hydrocarbon chain length that still allows for layer formation is 10 carbons, with greater chain length increasing interlayer separation at the cost of higher crystallization times [16]. Control of the hydrophilic head on the other hand modulates the thickness of the layers, and here the SDAs can be further divided. One type is the typical surfactant as the one presented in the example given above, with one end of the molecule containing the long hydrocarbon chain. The gemini type is characterised by having long hydrocarbon chains on both extremities, with the same surfactant being able to space the zeolite nanosheet on both faces. However, both types show similar behaviours. The ammonium groups connected to the long alkyl chains don't act as SDA moieties, but as a linker between the hydrophobic spacer part of the molecule and the hydrophilic section, whose inner ammonium groups have sufficiently high molecular degrees of freedom to act as SDAs. And so, single long carbon chain BSDAs with 2, 3 and 4 ammonium groups and gemini BSDAs with 3, 4 and 5 ammonium groups originate layers 1, 2 and 3 micropores thick, whose thicknesses correspond respectively to around 1.5, 2.5 and 3.5 nm. Molecules with a lower number of ammonium groups were unable to generate nanosheet structures [16], [19]–[23].

The discovered structures for MFI frameworks are stacked multilamelar precursor with surfactant, unilamellar precursor with surfactant (house of cards or disordered), hexagonally ordered mesoporous materials, and self-pillared as are shown in **Figure 9** [15], [16]. This last one consists of stacks of layers intergrown with a second set at right angles, with both MFI and MEL topologies being present. It's the similarity between the frameworks (causing their differentiation by x-ray diffraction to be very tricky) that allows the appearance of both in the same reaction [15], [16]. Another interesting aspect is that no surfactant SDAs

were used in their original synthesis, utilizing instead tetrabutylphosphonium and tetrabutyl ammonium hydroxide [16].

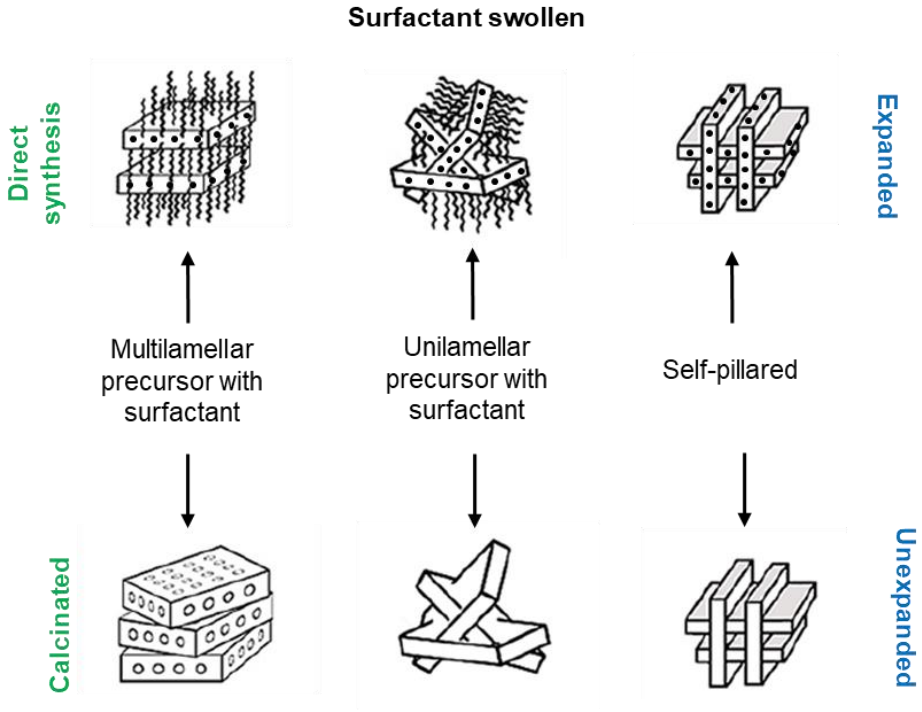

Figure 9. Surfactant swollen zeolite materials. Adapted from [15], [16].

ADOR

The previous approaches focused on direct synthesis, but a top-down methodology can also be used, where an already synthetized 3D zeolite is modified to produce the layered structures. The most prominent examples utilize germanosilicates such as UTL, UOV and SAZ-1, whose Ge-O bonds are labile enough to be hydrolysed in aqueous solutions at any pH, while leaving the rest of the structure intact [16]. Ge is in the structure's double-four rings and the rupture of the Ge-O bonds leads to the formation of zeolitic layers. The ADOR (assembly, disassembly, organization and reassembly) mechanism is applied in this approach as it allows for the preparation of materials not available by direct synthesis [15]. As the name suggests, the first step is the synthesis of the 3D germanosilicate, which is then disassembled by selective hydrolysis of the Ge-O bonds into layered materials. Then these can be modified or organized in a variety of ways, such as shifting the layers, removing debris material from the interlayer space, connecting layers with organic or inorganic pillars, etc. Finally, calcination causes the reassembly of the layers, yielding different materials depending on the organization step [16].

The ADOR protocol is a promising approach in the field although it still presents some challenges, such as its application to other types of zeolites other than germanosilicates.

1.4.3. 2D zeolite modifications

Synthetised layered precursors and surfactant templated zeolites already present enhanced accessibility and transport properties. However, their great tunability and potential for structural modification, not only allows to tune interlayer space or mesopores' shape, but also to add heteroatoms and create composite materials, making them far more flexible than their 3D counterpart, with a myriad of different modifications available, as is exemplified in **Figure 10**.

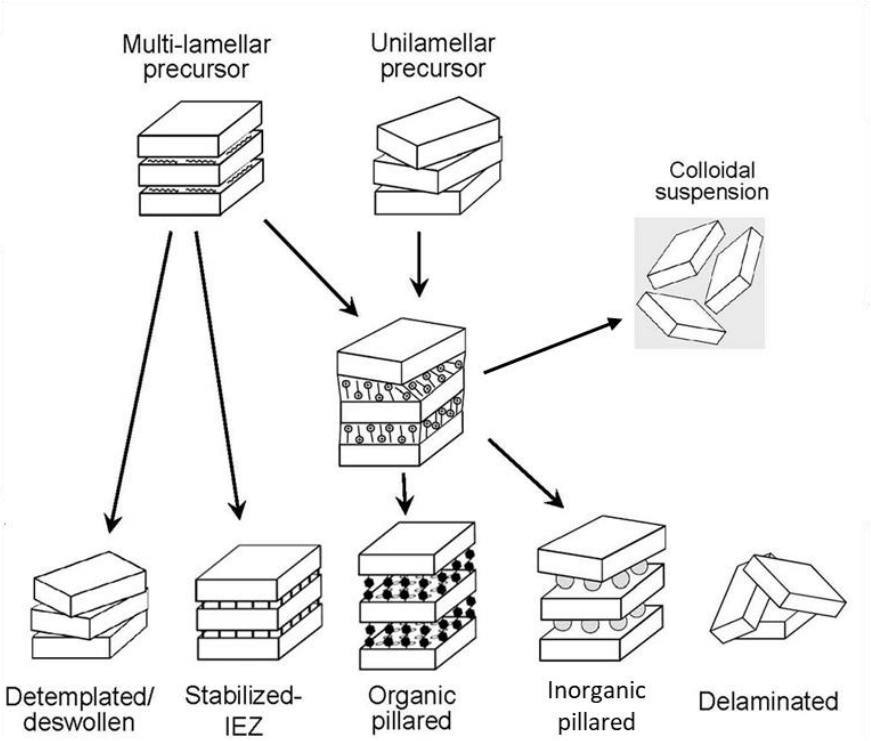

Figure 10. Post synthesis modifications of layered zeolites, taken from [16].

Sometimes it might be desirable to remove the SDA from the structure without condensing the surface silanols and bridging the layers. This can be achieved by washing the layered precursor with diluted HNO_3 solution under 80ºC. With the SDA removed, the layers will be randomly staked atop one another, without being covalently bonded, still

presenting the characteristic increased surface area and reduced micropore volume of 2D zeolites [16]. These materials are often called sub-zeolites, detemplated or deswollen.

In surfactant swollen zeolites, surfactant molecules vertically occupy the interlayer space, rupturing the intermolecular bonds between layers and expanding interlayer spacing. Typically, sweeling is performed in a high pH medium, as well as in the absence of small cations. The former favours surfactant aggregation in between the layers, while the latter avoids obstruction of the connection of surfactants into the interlayer space [15], [16]. An interpretation for why these conditions favour sweeling was given for MWW: since it has a low amount of surface silanols, at lower pH the surfaces are less polar, more hydrophobic, and so the surfactants lay horizontally in the interlayer space, causing little expansion. At high pH deprotonated silanols are formed, whose negative charge will attract surfactants, causing expansion. By using base salts with bigger cations, such as TPAOH and TBAOH, these cations will be less efficient in bonding to the deprotonated silanols, allowing bonding of surfactant molecules instead [15], [16]. The removal of surfactant from materials swollen post synthesis is much easier than from the intrinsic swollen surfactant templated zeolites, since in the latter the molecules also act as SDA confined in the micropores [16].

Surfactant swelling is a critical process as it allows many other modifications to be performed. For example, by calcining the swollen zeolite in the presence of certain compounds that do not degrade under calcination, not only will the surfactants be removed, but the compounds will condense, bonding to each other and the layers, forming pillars that maintain the interlayer distance [15], [16]. The pillars can be inorganic, with the most prominent example being TEOS (Tetraethyl orthosilicate), which although enhancing the materials porosity, the insertion of non-active amorphous silicon pillars is not ideal [15], [16]. To bypass this issue, research has been focused on incorporating active heteroatoms like Al, Ti, and Fe into the pillars, although there haven’t been major breakthroughs yet [15], [16]. The pillars could also be organic, with the insertion of organic molecules with functional groups that can function as active centres, although then these materials cannot be activated above 500 ºC as is often desired [15].

On the other hand, the distance between the as-synthesized layers with no swelling can be preserved by bridging the surface silanols of opposite layers with an Si atom [15], [16]. This results in O-Si$(R)_2$-O groups, extending the interlayer distance by 2 Si-O bonds in relation to the 3D form, with the resulting material being named interlayer expanded zeolite, IEZ [15], [16]. The synthesis involves silylation in acid media with (alkyl)$_2$Si$(OR)_2$, where

once inserted, the Si atoms usually only connect to the zeolite by two bonds, and the alkyl groups are free, slightly narrowing the pore entrance [15].

Delaminated zeolites are composed of randomly oriented layers taking a “house-of-cards” morphology as represented in **Figure 10**, creating fixed mesopores, which maximizes surface area and active site accessibility [15], [16]. They were first obtained by sonicating, coagulating, isolating and then calcinating swollen MWW, however this approach hasn’t been applicable to most of the other zeolites, with NSI, FER and RWR precursors being some of the few edge cases [15], [16].

Finally, exfoliation of swollen MWW and MFI zeolites disperses the layers, creating a colloidal solution, which has been useful for zeolite membrane preparation [15], [16]. The first procedure involved extrusion with a polymer, followed by organic solvent extraction and surfactant removal, although later a method was developed which simply required treatment with a TBAOH solution and centrifugation [15].

1.4.4. 2D vs 3D

The nanosheets of the various 2D forms and their arrangements have a high ratio of surface area to total area, which can be up to 50% compared to the typical 2% in micron-sized 3d zeolites. They also possess the traditional zeolite microporosity in the intralayer pores, while the interlayer spaces form mesopores of tuneable size and shape [15]–[17]. Together these properties endow these materials with a high number of active acid sites in the external surface, mesopores and in the micropores mouths in comparison to those enclosed in the micropores [15]–[17]. Therefore, 2D zeolites have much better accessibility to the acid sites, as well as enhanced diffusion properties, especially for bulkier molecules [16], [17]. It is important to consider that these acid sites are in less confined spaces than those of 3D zeolites sites, located in enclosed angstrom sized pores, and so their strength and affinity will be different [15]–[17]. As of now it is difficult to say if they are strictly better or worse, as there are mixed reports, dependent on the specific circumstances, but enhanced performance in certain reactions has been achieved, especially with delaminated and pillared zeolite materials [15], [17].

The other hallmark characteristic of 2D zeolites is their potential for modification, allowing for a level of structural and compositional flexibility as well as multi-functionalization not possible on rigid 3D zeolites [15]–[17].

However, the downsides associated with these materials must also be considered. The synthesis and modification steps needed to produce these materials increases the time, labour and cost of production when compared to the simple and relatively inexpensive synthesis of 3D zeolites, which might not be scalable to the industrial scale [15], [16]. The intrinsic acidity and number of acid sites is also distinct between the two types of materials, increasing in some cases, and decreasing in others, with the consensus being that ,at the moment, 3D zeolites' activity is still overall superior [15], [16].

1.5. Techniques to study acidity in zeolites

1.5.1. Solid-state nuclear magnetic resonance

Nuclear magnetic resonance (NMR) is a spectroscopic technique which utilizes radio frequency radiation and magnetic fields to manipulate the spin of atomic nuclei. The nuclei's signal will not only be dependent on its nature but also on its chemical environment (among other factors), allowing the differentiation between distinct atoms of the same element. A more in-depth discussion of the theory behind this technique as well as some experimental considerations has already been performed in the monography previously presented on the 08/01/2024 for this thesis [24]. Such a detailed and thorough section was not included in this document as it was too extensive. Moreover, reading the following material is also recommended [25]–[35].

The most relevant nuclei playing a significant role in zeolite's acidic groups are H, Si and Al, and so their NMR spectra will yield complementary information regarding zeolite acidity, each with its challenges and advantages.

^{29}Si NMR

The NMR active isotope of silicon is ^{29}Si, possessing spin I = $\frac{1}{2}$ it does not present quadrupolar coupling, however MAS and decoupling techniques are necessary to remove dipolar coupling and chemical shift anisotropy (CSA). Although it presents a low natural abundance of 4.7%, ^{29}Si spectra have high spectral resolution thanks to relative narrow resonant lines [26].

Silicon within the zeolite framework is part of TO_4 groups, and it isn't directly involved in either Bronsted or Lewis acidity, however, it's NMR spectra can still provide useful information. In its second sphere of coordination, the centre of the four tetrahedra can either be occupied by silicon or by aluminium, therefore silicon atoms are labelled Si(nAl), with n=0,1,2,3 or 4 depending on the number of aluminium atoms. These different chemical environments lead to signals that are detectable inside a typical chemical shift range between -80 and -120 ppm, where higher n value give rise to higher chemical shifts (lower ppm in absolute values) [25], [26]. Since peak area is proportional to concentration, the Si/Al ratio can be estimated based on the different n peaks following equation 4, where $I_{Si(nAl)}$ is the intensity of the peak corresponding to the Si(nAl) groups, although it only applies to materials with Si/Al ratios lower than 10 [25], [26], [36].

$$\frac{Si}{Al} = \frac{\sum_{n=0}^{4} I_{Si(nAl)}}{\sum_{n=0}^{4} \frac{n I_{Si(nAl)}}{4}} \qquad (4)$$

Silicon atoms at the external surfaces of the crystallites, and present in framework defects such as silanol nests have OH groups substituting either OSi or OAl groups, which will also influence the position of the NMR peak. The presence of the OH groups shifts the signal to higher ppm values (lower in absolute value) as opposed to the group where the OH did not replace a OSi group, and can be distinguished by a higher intensity enhancement in cross-polarization spectra, since peak intensity in this technique is dependent on the proximity to protons [25]. In **Figure 11** both the effect of different n numbers and the presence of OH groups can be visible in the ^{29}Si MAS NMR spectra of a HZSM-5 zeolite [25].

Moreover, in addition to evaluating the silicon environment of a given material, this technique allows to follow the degree of dealumination of a sample, as signal intensities from Si(nAl) groups with n≥1 will decrease with increasing dealumination degree.

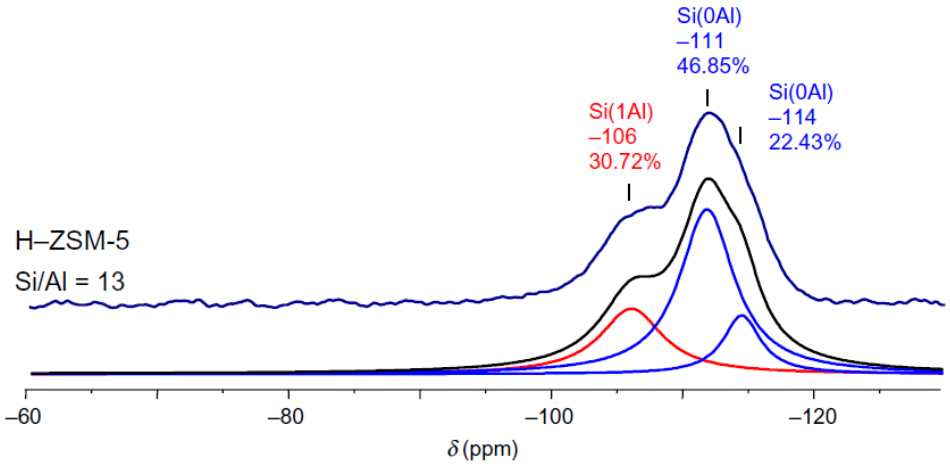

Figure 11. ^{29}Si MAS NMR spectrum of HZSM-5 with a Si/Al ratio of 13. The top blue line represents the real NMR spectra. The red and blue lines underneath it represent the peak deconvolution of the distinct silicon chemical environments (one aluminium and no aluminium respectively). Corresponding percentages of each peak area are also given. The black line represents the sum of the deconvoluted peaks. Taken from [25].

^{1}H NMR

The NMR active isotope of hydrogen is ^{1}H, possessing spin I = $\frac{1}{2}$, high gyromagnetic ratio and 100% natural abundance, making ^{1}H NMR have one of the highest sensitivities and lower acquisition times of any other NMR-active isotope. It does however possess a narrow chemical shift range, which limits its spectral resolution [25].

^{1}H MAS NMR spectra of dehydrated zeolites have characteristic signals in the range from 0 to 16 ppm, where AlOH groups present chemical shifts between -0.5-1.0 ppm, silanol groups present in the external crystallite surfaces and framework defect present signals at 1.2-2.2 ppm, while bridging hydroxyl group hydrogens exhibit resonances between 3.6-4.3 ppm. Has was mentioned previously, hydrogen bonding shifts the ^{1}H NMR signals to higher chemical shift values, and therefore when hydrogen bonded AlOH groups present chemical shifts between 2.4-6.2, silanol groups in silanol nests present signals around 10-16 ppm, while bridging hydroxyl group hydrogens exhibit resonances between 4.6-8.0 ppm [25], [37].

Having identified the ^{1}H NMR peaks as arising from framework aluminium or EFAL, their concentrations can be determined: relative concentration by direct peak comparison, and absolute concentration by adding an internal standard to the sample prior to acquisition of the NMR data. This is very useful to follow the dealumination process and evaluate the various acidic species present [25].

^{27}Al NMR

The NMR active isotope of aluminium is ^{27}Al, possessing spin I = $\frac{5}{2}$ it presents quadrupolar coupling, alongside dipolar coupling and chemical shift anisotropy. This nucleus' natural abundance is 100% and has generally fast relaxation times allowing for good quality spectra to be acquired with typically short measurement times [26]. The analysis of ^{27}Al NMR experiments is very useful for the study of zeolite acidity since aluminium atoms are present in zeolites' acid sites, presenting different structures depending on its Bronsted or Lewis nature. As such, it enables the detection of different types of aluminium structures such as framework aluminium and different EFALs, as well as their quantification.

Framework aluminium is always in the tetrahedral environment $Al(OSi)_4$, since Löwenstein's rule forbids Al-O-Al pairings [8]. The typical chemical shifts corresponding to these tetrahedral species is between 55 and 68 ppm [25], [26]. The other typical aluminium species in zeolites are EFAL, which have a more diverse signal distribution owing to their varied nature. They all appear at lower chemical shifts, with octahedral EFAL appearing around -10 to 15 ppm, and penta-coordinated and distorted tetra-coordinated EFAL appearing around 30 to 50 ppm [25], [26], [38].

One issue arising due to the fact that ^{27}Al is a quadrupolar nuclei, is related with the second-order quadrupolar interaction that is not totally averaged out with MAS, and so,

species with high quadrupolar interactions will present severe line broadening. This line broadening can get so intense that some signals start overlapping, hiding the less intense features, generating “invisible aluminium” species. Stronger quadrupolar interactions are often associated with more asymmetric geometries, and species such as aluminium clusters, oxide hydrates and penta-coordinated and distorted tetra-coordinated EFAL tend to exhibit stronger line broadening [25], [26]. The presence or absence of water in the zeolite is also important to take into consideration, since it can interact with framework aluminium and coordinate with EFAL species to increase their stability and symmetry, thereby reducing the quadrupolar interaction [25]. Other methods to reduce the quadrupolar interaction and detect “invisible aluminium” is to increase the magnetic field strength, since this interaction decreases with the square of the field strength, or the use of transfer of population in double resonance technique, TRAPDOR [26].

1.5.2. Vibrational spectroscopy

Vibrational spectroscopy is based on the interaction of chemical bonds with energy causing a vibrational energy level transition, which can be detected. As different bonds will have distinct energy levels, various molecular features can be detected and understood with this technique. This technique can be divided in two main approaches, modulation of the energy levels with either electromagnetic radiation or with neutrons. As before, a more in-depth discussion of the theory behind this spectroscopy has already been performed in the monography previously presented for this thesis [24]. Such a detailed and thorough section was not included in this document as it was too extensive. Moreover, reading the following material is also recommended [39], [40].

Infrared and Raman spectroscopy

Raman and infrared (IR) spectroscopies probe the molecules’ vibrational states, but as they do it in different ways, they present different selection rules, revealing distinct but complementary information, where some inactive modes in infrared can be viewed through Raman and vice-versa.

In IR spectroscopy, a photon with energy matching the energy gap between vibrational states hits the molecule, being absorbed and promoting said transition, allowing its detection. The energy difference between vibrational states corresponds to frequencies in the infrared region, hence infrared spectroscopy. However, for this type of phenomenon to occur, the vibration in question must cause the molecule’s dipole moment to change. This

selection rule explains why the asymmetric stretching in CO_2 is visible in infrared spectroscopy, while the symmetric stretching is not, dipole moment stays constant [39], [41].

Raman spectroscopy isn't based on light absorption, but on its inelastic diffusion. Light with frequency much higher than any of the vibrational transitions is irradiated on the sample, allowing it to enter a prohibited virtual state, which will quickly decay into an allowed lower energy state. Usually, it will revert to the original vibrational state, Rayleigh scattering, but occasionally it will transition either to a lower energy state, anti-Stokes scattering, or to a higher energy state, Stokes scattering. Then, by measuring the difference between the absorbed and emitted light, the energy gap can be measured. The selection rule in this case is that the vibration must cause the molecule's polarizability to change, and so, in reverse to infrared spectroscopy, the asymmetric stretching in CO_2 is not visible in Raman spectroscopy, while the symmetric stretching is, polarizability changes during the vibration [40], [41].

One example of the application of these techniques in zeolites is the use of infrared spectroscopy for the detection of different OH acid groups, and quantification based on band intensity. As previously mentioned, stronger OH bonds (weaker Bronsted acidity) exhibit higher stretching frequencies, which has allowed to delineate rough spectral regions corresponding to different OH bands, which are listed in **Table 1** [12], [38], [42], [43].

This type of analysis requires thermal activation in vacuo at high temperatures to ensure removal of molecules adsorbed in the structure's channels that could perturb the OH groups' vibrations, namely the template molecules and water [12], [43]. In a study performed by Zachariou *et al.*, DRIFTS spectra (Diffuse Reflectance Infrared Fourier Transform Spectroscopy) of HZSM-5 zeolite were obtained, as seen in **Figure 12** [43].

Table 1. Spectral regions of different OH bands in zeolites [12], [38], [42], [43]

Type of OH group	Spectral region (cm^{-1})
Isolated EFAL	3775-3840
Silanol	3675-3775
H-bonded EFAL	3650-3700
Isolated Bronsted site	3575-3675
H-bonded Bronsted site	3400-3575

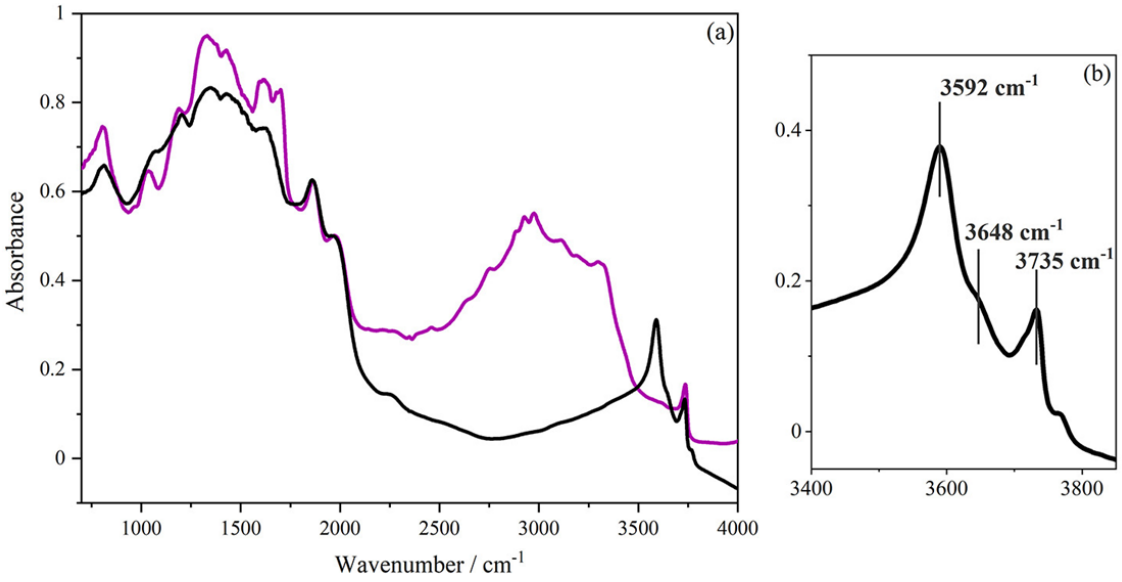

Figure 12. DRIFTS spectra of HZSM-5. (a) the purple and black line represent the sample's spectra before and after thermal treatment at 350 ºC under nitrogen atmosphere respectively. (b) zoom on the OH bands region of treated samples [43].

Figure 12a shows the spectra of the zeolite sample before and after thermal treatment, in purple and black respectively, where in this case the interference of the template molecules can be clearly visible with the absence of the intense band at 3592 cm^{-1}. Although not the case, in different zeolite samples there could be other bands present in the range between 2600 and 3500 cm^{-1} which would be hidden due to the template molecules enormous band, once again highlighting the importance of the thermal treatment and the vacuum. Focusing on the treated sample's spectrum in the region of interest, **Figure 12b**, two main bands can clearly be identified, one at 3592 cm^{-1} assigned to Bronsted acid groups and another at 3735 cm^{-1} assigned to silanol groups at the exterior of the zeolite's surface [43]. The presence of a low frequency tail also reflects the presence of internal silanol nests [12], [43]. Although not as intense, a peak at 3648 cm^{-1}, visible as a shoulder, was assigned to bonded EFAL species [43]. Although not assigned, there is also a small shoulder at around 3775 cm^{-1} which could arise from free EFAL species.

Inelastic neutron scattering

In the previous techniques the vibrational states were studied using photons, while in inelastic neutron scattering (INS) neutrons are used because of their useful properties.

Neutrons are non-charged subatomic particles with mass 1.009 u.m.a., presenting particle-wave duality ($\lambda = \frac{h}{p}$), typical of quantum particles, which is utilized in this technique [44], [45].

In an INS experiment the energy and wavelength of the emitted neutrons is selected by varying their velocity, based on equation 5.

$$E = \frac{1}{2}mv^2 = (\frac{hk}{2\pi})^2 \times \frac{1}{2m} \qquad (5)$$

Where **k**=$\frac{2\pi}{\lambda}$ is the neutron's wavevector, $\boldsymbol{\lambda}$ its wavelength, **m** its mass, $\boldsymbol{v}$ its velocity and **h** Plank's constant. The neutrons will then collide with the sample's atomic nuclei, interacting via the strong force, causing the neutrons to scatter. Because of this there are no selection rules in INS spectroscopy, all 3N-6 modes of vibration are active, unlike in Raman and infrared spectroscopies where the interaction occurs between light and electrons [44], [45].

The inelastic scattering of the neutrons will not only have transferred energy to the sample, $E_t = E_f - E_i$, but also momentum (Q), $Q_t = k_f - k_i$,since they have mass. The intensity of any i band in the INS spectra is dependent on the energy and momentum transfer and is illustrated in equation 21 [44], [45].

$$S(Q, nv_i) \propto \frac{(QU_i)^{2n}}{n!} e^{-(QU_{total})^2} \sigma_{v_i} \qquad (6)$$

Where $\boldsymbol{v_i}$ is the ith vibrational mode with frequency v, **Q** is the momentum transfer and $\mathbf{U_i}$ is the root mean square displacement of the ith mode atoms. The exponential term is the Debye-Waler factor, which contains $\mathbf{U_{total}}$, the total root mean square displacement of all atoms in all vibrations. Its magnitude is determined by the thermal movement in the molecule, and if it becomes too big it can cause the spectra to be more difficult to analyse, so samples tend to be recorded bellow 30K. Finally, $\boldsymbol{\sigma_{v_i}}$ is the total scattering cross section of the elements in vibration i, being an element and isotope dependent constant [44], [45]. For example, hydrogen's (^{1}H) σ is 82.03 barns (1 barn= 10^{-28} m^{-2}), deuterium's (^{2}H) σ is 7.64 barns, silicon's (^{29}Si) σ is 2.78 barn and aluminium's (^{27}Al) σ is 1.503 barns [46]. Thanks to the combination of a large cross section, and the fact that it has one of the largest amplitudes of vibration due to its low weight, hydrogen's bands will be the most intense in the spectra, and unless its concentration in the sample relative to other elements is quite low, they will drown all other bands [44], [45].

Another advantage of INS spectroscopy is that by knowing the neutron scattering cross section of the moving nuclei, the transition energies and atomic displacements of the vibrational modes, the intensities of the INS spectra can be predicted with great accuracy.

Since the cross sections are nuclei constants, and the energies and displacements are readily obtained from quantum calculations, an astounding agreement between experimental and predicted spectra is achieved [44].

In another study performed by Zachariou *et al.*, INS spectra of HZSM-5 zeolite were taken using pyridine as a probe molecule to evaluate the acid sites in the sample, which are displayed in **Figure 13** [43].

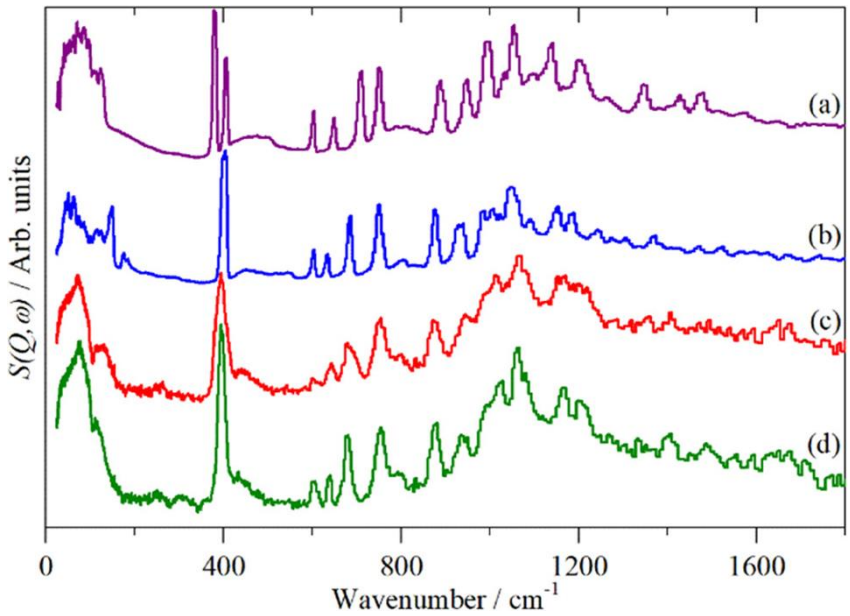

Figure 13. INS spectra of (a) pyridine; (b) pyridinium chloride; (c) dried HZSM-5 at 373 K after pyridine adsorption; (d) same HZSM-5 sample as in (c) after desorption at 523 K [43].

Although HZSM-5 contains protons, their concentration is scarce, especially when compared with pyridine, and so INS allows to analyse changes more clearly in the adsorbed pyridine's bands. Depending on the type of acid site, pyridine will take on different forms: if interacting with a Lewis site, it will remain in its molecular form, but if it reacts with a Bronsted site, it will accept a proton, becoming chemisorbed in the form of a pyridinium ion. As such, by comparing the sample's spectra to the reference compounds (**Figure 13a** and **b**), the main form of the adsorbed pyridine and the principal acid type interaction can be inferred. The main differences between the spectra of the different pyridine forms are the doublet at 378 and 406 cm^{-1} from pyridine, while pyridinium chloride only has a peak at 404 cm^{-1}, and pyridine's sharp peak at 991 cm^{-1}, while in pyridinium chloride it is only present as a shoulder at 1047 cm^{-1}. Looking at **Figure 13c** and **13d**, loaded HZSM-5 sample before and after desorption, they both resemble more closely spectrum **(b)**, indicating that pyridine is mostly

chemisorbed on Bronsted sites, however, the broader peaks in spectrum **(c)** that become sharper in spectrum **(d)** after desorption, indicate the presence of excess pyridine that becomes physiosorbed in the sample. Further analysis concluded that if any pyridine was adsorbed on Lewis sites, it was masked by the excess physiosorbed pyridine [43].

1.5.3. Computational methods

Computational chemistry is a branch of chemistry where experiments are run on computers with specific molecular models, allowing to simulate the structure and properties of different compounds, materials, and reactions. The combination of these results with experimental data is a powerful tool in the study of any complex system as is the case of zeolites [47]–[49]. With the constant evolution of computational power, heralded by Moore's Law, more demanding but accurate models have been coming to the forefront, namely ab initio methods [50].

Ab initio is a Latin expression meaning "from the beginning" and it refers to methods with no experimental parametrization, based solely on quantum mechanics and solving the time-independent Schrödinger equation, represented in equation 22. [50]–[52].

$$H\psi = E\psi \qquad (7)$$

H is the Hamiltonian, a mathematical operator describing the total energy of the system, $\boldsymbol{\psi}$ is the wavefunction, the mathematical descriptor of the system and **E** is the system's energy. At the base of any computation will be the variational principle which states that the energy calculated from any trial wavefunction will be bigger or equal to the system's real energy [51]. This implies that the trial wavefunction that minimizes the systems energy will always be the closest solution to the real value, and so the problem becomes a minimization.

One issue is that no analytical solution for this equation can be obtained for any multi-electron system, as it becomes too complex to solve, illustrated with the ever-increasing complexity of the Hamiltonian for a generic system in equations 23. Here **n** and **e** refer to nuclei and electrons respectively, **T** and **V** are the kinetic energy and potential energy operators, **M**, **Z**, **R** and **m**, **e**, **r** are the mass, charge and distance relative to the nuclei and electron respectively.

$$H = T^n + V^{nn} + T^e + V^{ee} + V^{ne} + \cdots \qquad (8)$$

$$H = \sum_{I=1}^{N_n} -\frac{\nabla_{R_I}^2}{2M_I} + \sum_{I=1}^{N_n}\sum_{J>1}^{N_n}\frac{Z_I Z_J}{|R_I - R_J|} + \sum_{i=1}^{N_e} -\frac{\nabla_{r_i}^2}{2m_i} + \sum_{i=1}^{N_e}\sum_{j>1}^{N_e}\frac{e^2}{|r_i - r_j|} + \sum_{i=1}^{N_e}\sum_{I=1}^{N_n}\frac{-Z_I e}{|r_i - R_I|} + \cdots \quad (8')$$

As such, some approximations must be made to simplify the computation without compromising accuracy too much. The Born-Oppenheimer approximation arises from the fact that the mass of the nucleus is more than 1000 times bigger than the mass of the electron, meaning the latter will move much more rapidly and quickly adjust to changing nuclear positions. Thus, the wavefunction can be separated into electronic and nuclear components which can be treated separately, allowing to determine the electronic energy as a function of fixed nuclear positions, forming a potential energy surface [50], [51].

Another approximation is the Hartree-Fock (HF) method, where instead of computing the complex polyelectronic wavefunction, the “Schrödinger” equation is solved n times (where n is the number of electrons) for the n monoelectronic functions, molecular orbitals, naming these equations Hartree equations. The polyelectronic wavefunction is then obtained by calculating the anti-symmetrized product of the monoelectronic functions, called the Slater monodeterminant, guaranteeing the inclusion of the electron exchange interaction, which is the interaction between matching spin electrons (Pauli’s exclusion principle). The advantage of this approach is that solving n times the Hartree equation is much simpler than solving the Schrödinger equation once [50], [51]. One problem is the electro-electron repulsion term of the Hamiltonian, which is incompatible with the “single” electron treatment. As such it was substituted with an effective repulsion term, where instead of considering each individual electron, an effective field is constructed from the average position of the other electrons. This gives rise to the iterative self-consistent field, where a set of initial monoelectronic wavefunctions are guessed, and the effective field is obtained from them. Then the Hartree equations are solved using the obtained field, producing new wavefunctions, which originate a new field, and so on. This process is repeated until the new wavefunctions are the same as those in the last step, the field is self-consistent and convergence is reached [50], [51]. One issue with using the effective field is that it doesn’t account for the correlation interaction, a non-classical instantaneous interaction between the individual electrons, meaning the predicted energy, in the best-case scenario, will always be greater than the exact energy by the electron correlation energy. This marks a dividing line between Hartree-Fock methods, which use the aforementioned approximations, and Post-Hartree-Fock methods, which attempt to include electron correlation through different approaches, which include Møller-Plesset theory (MP2, MP4, etc) and coupled cluster method. The drawback of these is the much higher computational burden when compared with simple Hartree-Fock methods, illustrated in **Figure 14**, as they scale at n^5 and n^7 respectively with n being the number of electrons, while Hartree-Fock scales at n^4 (3 spacial dimensions and spin) [50], [51].

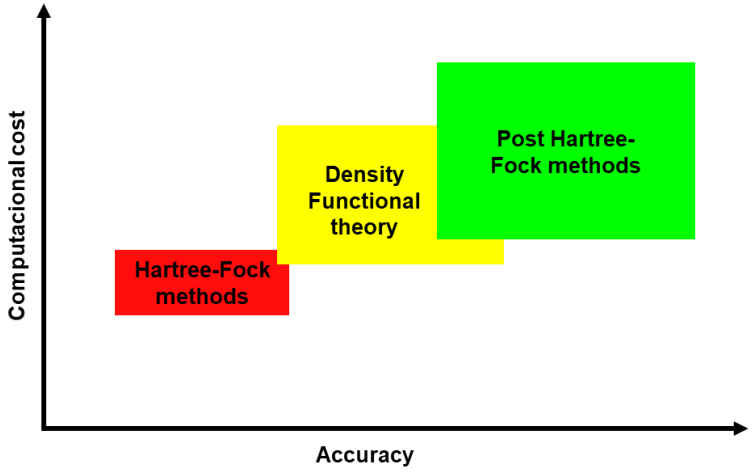

Figure 14. Computational burden vs accuracy scheme of Hartree-Fock (red), density functional theory (yellow) and post Hartree-Fock (green) methods.

In **Figure 14** there is an intermediary group between simple and post Hartree-Fock, called Density functional theory (DFT). The electron density function, $[\boldsymbol{\rho}(\boldsymbol{r})]$, is dependent on only 3 variables, the position in space, while the polyelectronic wavefunction is dependent on the position of each electron, 3n variables, meaning the computation could become much simpler if it could be done using electron density instead of wavefunctions. As it turns out this can be done, with the Hohenberg-Kohn theorem stating that there is a functional of electron density, **E**, that gives the systems electronic energy if the input density corresponds to the ground state, represented by equation 9 [50], [51].

$$E[\rho(r)] \geq E_{eletronic} \qquad (9)$$

$$E[\rho(r)] = T^{e}[\rho(r)] + V^{ne}[\rho(r)] + V^{ee}[\rho(r)] + E^{exchange-correlation}[\rho(r)] \qquad (9')$$

One problem with DFT is that although the full **E** functional has been proven to exists, only the first three functionals in equation 9', kinetic energy, electron-nuclei and electron-electron potential energy respectively, are known, with the exact form of the exchange and correlation functionals still being undiscovered to this day. Even though now we don't have an exact equation for our chemical system, there are approximations for the missing functionals that, surprisingly, give quite accurate results, nesting DFT right in the middle of the accuracy vs computational burden balance. One example is the B3LYP method, where Becke's exchange functional is used alongside 3 parameter Lee-Yang-Parr correlation function [50], [51].

Besides the chosen method, the accuracy and computational time will also depend on the size of the system and the selected basis set, which is a group of functions that describe the atomic orbitals (AO), that are then linearly combined to compute the system's molecular orbitals in simple and post Hartree-Fock methods, or electron density in DFT. The number and type of functions of the basis set will dictate the calculation's accuracy and computational time. An example of a basis set is the 6-311++G(d,p) (or 6-311++G**). Here G indicates that Gaussian type orbital (GTO) functions were used to describe the AOs. Although Slater type orbitals (STO) more closely resemble the real orbitals, they are very computationally expensive, making it much more efficient to compute multiple GTOs and combine them for a more accurate function. 6-311 indicates that the split-valence approach was taken, where a combination of 6 GTOs where use to describe the core orbitals, while a combination of 3 GTOs and 2 different individual GTOs were used for the inner valence and outer valence orbitals respectively. Finally, further modifications can be made to better approximate the system to reality, like considering the polarization of the orbitals by the surroundings, giving them more flexibility, and the existence of diffuse orbitals, done by including (d,p) (or **) and ++ terms respectively [50]–[52].

2. Foreword and goals

The main goal of this Master thesis was to address a few of the open questions related with the structure and properties of zeolites, continuing the work that has been developed in the research groups SPECKO and CS+, within CICECO – Aveiro Institute of Materials and, in addition, fostering the collaboration with the group led by Prof. Mariya Shamzhy at the Charles University in Prague, specialised in engineering solid catalysts.

The foremost challenge was to embrace the plethora of techniques and previous experimental data available on the target systems, correlating the input from different collaborators, adding new experimental results, and contributing to a global view of the problem. Overall, this included the use of computational tools (for discrete and periodic systems), solid-state NMR spectroscopy, vibrational spectroscopy (in both the optical and neutron flavours), and the synthesis of 2D zeolites, with their subsequent characterization (through x-ray and nitrogen adsorption methods). A set of analytical techniques and experiments that can hardly be fitted within a master thesis period.

In this way, some of the results presented and discussed in this work have been obtained by other researchers, either previously or in the course of the collaborations mentioned above. This is the case, e.g., for some of the calculations and the experimental inelastic neutron scattering spectra. This is clearly stated in each case, either giving a reference to the project or assigning the credits directly in the text.

For this purpose, two main research goals were established:

1. Synthesis and characterization of 2D layered surfactant templated zeolites with differing nanosheet thickness. As a recent chapter in the zeolite field of research, there is still much to learn about how these materials can be made, their properties and how they can be fine-tuned for specific applications. With this goal in mind, I spent 6 weeks at Charles University in Prague, where in collaboration with the group of Prof. Mariya Shamzhy, I attempted the synthesis of 2D layered ZSM-5 zeolites with differing thicknesses and the corresponding gemini bifunctional structure directing agents with three, four and five ammonium groups. The materials were then characterized by X-ray diffraction (XRD) for structure determination and nitrogen physisorption for textural properties. Due to time constraints and an ambitious workplan, I was not able to conclude all the necessary measurements and synthesis and part of the work is still underway.

2. Study of EFAL species in H-ZSM-5 zeolites. For this end, five samples were chosen, H-ZSM-5 in pristine form to act as the blank material with barely any EFAL species; H-ZSM-5 steamed at 450 and 600 °C to introduce EFAL species and account for different

degrees of dealumination; H-ZSM-5 dealuminated by strong acid leaching (3 M HNO_3) to compare different dealumination approaches and finally silicalite-1 was also studied, as it represents the same type of framework as the previous samples (MFI) while containing no aluminium in its composition. They were all analysed by vibrational spectroscopy (infrared and INS), as well as by solid-state NMR to try to better understand the effect of the various treatments on the samples, with a special focus on the generated EFAL species and their possible structures. To aid in this endeavour, density functional theory simulations of the H-ZSM-5 framework, possible EFAL structures and their respective vibrational spectra were performed. The goal was to be able to do experimental spectral assignment, allowing to more clearly correlate signals and their variations to their corresponding atomic moieties.

3. Materials and methods

3.1. Materials

3.1.1. 2D zeolites

3.1.1.1. Synthesis of bifunctional directing agents

Three bifunctional structure directing agents were chosen for the synthesis of the 2D layered MFI, namely $[CH_3(CH_2)_{17}N^+(CH_3)_2(CH_2)_6N^+(CH_3)_2(CH_2)_6N^+(CH_3)_2(CH_2)_{17}CH_3]Br_3$; $[CH_3(CH_2)_{17}N^+(CH_3)_2(CH_2)_6N^+(CH_3)_2(CH_2)_6N^+(CH_3)_2(CH_2)_6N^+(CH_3)_2(CH_2)_{17}CH_3]Br_4$; $[CH_3(CH_2)_{17}N^+(CH_3)_2(CH_2)_6N^+(CH_3)_2(CH_2)_6N^+(CH_3)_2(CH_2)_6N^+(CH_3)_2(CH_2)_6N^+(CH_3)_2(CH_2)_{17}CH_3]Br_5$, hereby labelled as 18-N_3-18, 18-N_4-18 and 18-N_5-18 respectively, with their molecular structures illustrated bellow. Their synthesis were based on available literature procedures (compounds' reactions schematized in appendix A) [19].

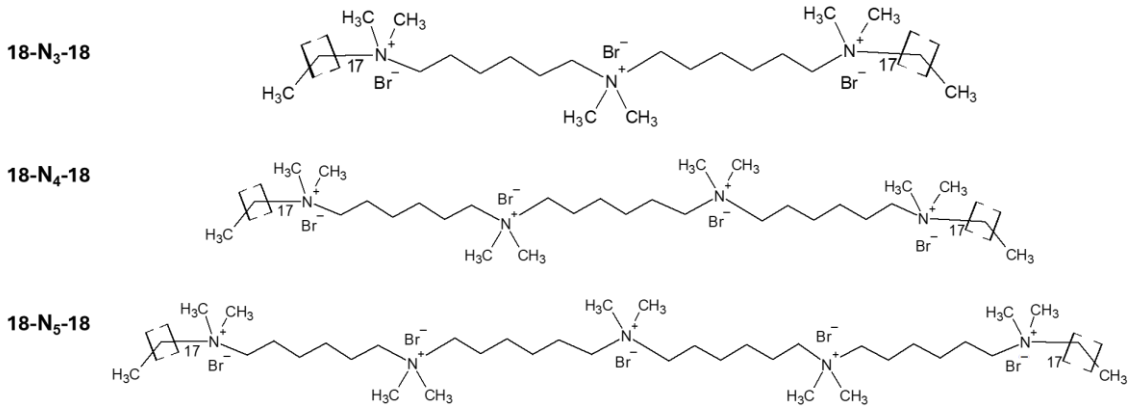

Figure 15. Molecular structure of the target bifunctional structure directing agents.

18-N_3-18 SDA was prepared via a three-step reaction process. First $[CH_3(CH_2)_{17}N^+(CH_3)_2(CH_2)_6Br]Br^-$ (hereby labelled as 18-N-Br) was prepared by adding 0.113 mol of 1,6-dibromohexane (Sigma Aldrich, 96%) and 0.0113 mol of N,N'-dimethyloctadecylamine (TCI Chemical, >85%) to a solvent mixture of 167 mL of acetonitrile (HPLC grade, Sigma Aldrich, >99%) and 167 mL of toluene (Lach-Ner, p.a.), which was heated at 60 °C in an oil bath with agitation under reflux for 24 hours. The reaction mixture was then cooled to room temperature and the excess solvent removed in a rotary evaporator at 45 °C, reducing the pressure to 50 mbar. An appreciable amount of solvent was still present which had all the solid dissolved, so the mixture was left in the fridge for 3h. Then the resulting solid was filtered and washed with diethyl ether (VWR chemicals, >99%) using a vacuum pump and left overnight in a vacuum oven at room temperature. The second step was $[CH_3(CH_2)_{17}N^+(CH_3)_2(CH_2)_6N(CH_3)_2]Br^-$ synthesis

(hereby labelled as 18-N-N), done by adding 0.0150 mol of 1-bromooctadecane (Sigma Aldrich, 97%) and 0.150 mol of N,N,N',N'-tetramethyl-1,6-diaminohexane (TCI Chemicals, >98%) to a solvent mixture of 150 mL of acetonitrile and 150 mL of toluene, which was heated at 60 °C in an oil bath with agitation under reflux for 24 hours. The reaction mixture was then cooled to room temperature and the excess solvent removed in a rotary evaporator at 45 °C, reducing the pressure to 50 mbar. Just as in the previous reaction the mixture had to be left in the fridge for 3 h to crystalize the solid fraction. Then the resulting solid was filtered and washed with diethyl ether using a vacuum pump and left overnight in a vacuum oven at room temperature. For the final step equimolar amounts of 18-N-Br and 18-N-N were dissolved in acetonitrile (using between 800-1800% weight per total organic reactants) and left to react at 60 °C in an oil bath with agitation under reflux for 24 h. The solvent was then removed in a rotary evaporator at 45 °C, reducing the pressure to 50 mbar, and the resulting white solid was filtered using a vacuum pump, and left overnight in a vacuum oven at room temperature, obtaining 18-N_3-18. Solution state ^{1}H NMR (using $CDCL_3$ as solvent) was applied to 18-N-Br, 18-N-N and 18-N_3-18 to follow the reaction process.

18-N_4-18 was prepared by two approaches, a two-step and a three-step pathway. The first step is the same for both, and is the procedure described above to synthetize 18-N-Br. For the two-step pathway 0.0050 mol of 18-N-Br and 0.0010 mol of N,N,N',N'-tetramethyl-1,6-diaminohexane were then dissolved in acetonitrile, using 1600% weight per total organic reactant, heating the mixture to 60 ºC in an oil bath with agitation under reflux for 24 h. An excess of 18-N-Br was used to ensure that every mol of N,N,N',N'-tetramethyl-1,6-diaminohexane reacted with 2 mol of 18-N-Br, forming the desired 18-N_4-18. The solvent was then removed in a rotary evaporator at 45 °C, reducing the pressure to 50 mbar, and the resulting white solid was filtered using a vacuum pump, and left overnight in a vacuum oven at room temperature. In the three-step pathway, 0.010 mol of 18-N-Br and 0.010 mol of N,N,N',N'-tetramethyl-1,6-diaminohexane were dissolved in acetonitrile, using 1200% weight per total organic reactant, heating the mixture to 60 ºC in an oil bath with agitation under reflux for 24 h. The solvent was then removed in a rotary evaporator at 45 °C, reducing the pressure to 50 mbar, and the resulting white solid, $[CH_3(CH_2)_{17}N^+(CH_3)_2(CH_2)_6N^+(CH_3)_2(CH_2)_6N(CH_3)_2]Br_2$ (hereby labelled as 18-N-N-N), was filtered using a vacuum pump, and left overnight in a vacuum oven at room temperature. In the final step equimolar amounts of 18-N-Br and 18-N-N-N were dissolved in 1200% weight of acetonitrile per total organic reactant, heating the mixture to 60 ºC in an oil bath with agitation under reflux for 24 h. The solvent was then removed in a rotary evaporator at 45

°C, reducing the pressure to 50 mbar, and the resulting white solid, was filtered using a vacuum pump, and left overnight in a vacuum oven at room temperature. The rationale behind this approach is that by only using equimolar amounts the final solid product should contain only the desired 18-N_4-18, and no excess reagent (18-N-Br in the two-step pathway).

For the synthesis of 18-N_5-18 both 18-N-Br and 18-N-N were synthetized following the previously described procedures. Then 0.05 mol of N,N,N',N'-tetramethyl-1,6-diaminohexane and 0.05 mol of 1,6-dibromohexane were dissolved in a mixture of 125 mL of acetonitrile and 125 mL of toluene, reacting at 60 ºC in an oil bath with agitation under reflux for 24 h. The resulting solid, $[Br(CH_2)_6N^+(CH_3)_2(CH_2)_6N(CH_3)_2]Br$ (hereby labelled as Br-N-N) was washed with diethyl ether under a vacuum pump and put in vacuum oven at room temperature. Then I added equimolar amounts of 18-N-N and Br-N-N to 800% weight per total organic reactants of acetonitrile, reacting them at 60 ºC in an oil bath with agitation under reflux for 24 h. The resulting solid $[CH_3(CH_2)_{17}N^+(CH_3)_2(CH_2)_6N^+(CH_3)_2(CH_2)_6N^+(CH_3)_2(CH_2)_6N(CH_3)_2]Br_3$ (hereby labelled as 18-N-N-N-N) was washed with acetonitrile under a vacuum pump and put in vacuum oven at room temperature. Finally equimolar amounts of 18-N-Br and 18-N-N-N-N were added to 1200% weight per total organic reactants of acetonitrile, reacting them at 60 ºC in an oil bath with agitation under reflux for 24 h. The resulting 18-N_5-18 white solid was washed with acetonitrile under a vacuum pump and put in vacuum oven at room temperature.

3.1.1.2. Synthesis and calcination of 2D layered surfactant templated zeolites

The 2D layered surfactant templated zeolites were synthetized following the procedure described by Ryong Ryoo *et al*. [19]. To avoid possible Si contamination from glass, plastic beakers were used, adding the following reactants in this order: 43.912 g of distilled water; 0.5194 g of NaOH (Lach-Ner, p.a.); 0.1649 g of sodium aluminate (Na_2O %weight=42.5; Al_2O_3 %weight=53; Riedel-de Haën); 7.144 g of TEOS (Thermo Scientific, 98%); 6.318 g of ethanol absolute (VWR Chemicals, 100%) and 1.796, 2.153 or 2.507 g of 18-N_3-18, 18-N_4-18, or 18-N_5-18 SDA, obtaining gels with molar composition of 6.67 Na_2O: 0.75 Al_2O_3: 30 SiO_2: 1.5 SDA: 240 ethanol: 2132 water. The mixture was then left to age in an oil bath (beaker covered with parafilm to avoid ethanol evaporation) for 6 h at 60 ºC with agitation. After aging the gel was transferred to a 90 mL Teflon liner inside a stainless stell autoclave, which was put under rotation inside an oven at 145 ºC. At various points during the synthesis, small samples of the gel were taken to be analysed by x-ray to follow the reaction, with the shortest and longest successful reaction times being 8 and 11 days

respectively. When the crystallization was finished the Teflon liner contents were centrifuged and dried in an oven at 60 ºC to obtain the solid product. Finally, calcination was performed at 550 ºC for 6 h with 1 ºC/min ramp to remove the organic SDA.

The traditional 3D ZSM-5 zeolite was synthetized by adding the following reactants in this order: 64.35 g of distilled water; 0.529 g of KOH (Lach-Ner, p.a.); 1.508 g of tetrapropylammonium bromide (TPABr); 0.12 g of $Al(NO_3)_3.9H_2O$ (VWR Chemicals, 99%) and 3.31 of TEOS (Thermo Scientific, 98%). The gel was then left to age at room temperature (beaker covered with parafilm to avoid ethanol loss) for 5h with agitation. After aging the gel was transferred to a 90 mL Teflon liner inside a stainless stell autoclave, which was put under rotation inside an oven at 175 ºC for 2 days. When the crystallization was finished the Teflon liner contents were centrifuged and dried in an oven at 60 ºC to obtain the solid product. Finally, calcination was performed at 550 ºC for 6 h with 1 ºC/min ramp to remove the organic SDA.

3.1.2. MFI zeolites

The studied MFI zeolites were previously prepared by former PhD student Carlos Bornes, following the following procedures.

For 100% silica MFI framework material, hereby labelled simply as silicalite, 1.50 g of tetrapropylammonium bromide (TPABr, 98 wt%, Aldrich) was added and dissolved in 14.70 mL of distilled water. Then 5.60 g of tetrapropylammonium hydroxide (1 M TPAOH in water, Aldrich), 6.48 g of tetraethylorthosilicte (98 wt%, Aldrich) and 5.60 g of ethanol were added, with the resulting gel being aged for 6h with agitation at room temperature. After aging the gel was added to a Teflon liner inside an autoclave inside an oven at 180 °C, were it reacted for 4 days without agitation. The resulting solid was obtained by centrifugation, thorough washing with water and drying at 80 °C. To remove the organic SDA calcination was performed at 550 °C for 8h, with a heating rate of 3 °C/min.

For the different ZSM-5 samples, ammonium exchanged ZSM-5 (CBV3024E) with Si/Al ratio of 15 was obtained from Zeolyst International and subsequently calcined at 500 °C under 5 L/h of air flow. To minimize the amount of formed EFAL species the calcination was performed in two-steps: ramping of 2 °C/min from room temperature to 200 °C, where it was kept for 1 hour, followed by ramping of 2 °C/min from 200 °C to 500 °C, where it was kept for 6 h. Some of the resulting H-ZSM-5 sample, labelled as z15-ns (non-steamed), were exposed to a 2.3 L/h flow of water vapour for 2 h at 450 and 600 °C, with the resulting samples being denoted as z15-450 and z15-600. The acid-leached sample, z15-ns-hno3, was obtained by refluxing the H-ZSM-5 zeolite with 3 M of HNO_3 under stirring conditions

at a temperature of 60 ºC for 3 h. The sample was recovered by centrifugation and washed thoroughly with deionized water. The procedure was repeated three times, after which the sample was calcined at 500 ºC.

3.2. Methods

3.2.1. X-ray diffraction

The structure, crystallinity and phase purity of the prepared zeolites were determined by powder X-ray diffraction using a Bruker D8 Advance diffractometer equipped with energy dispersive detector LYNXEYE XE-T using Cu Kα radiation in Bragg-Brentano geometry. Measurements were carried out in the range from 3 to 40°. Samples were prepared by grinding of dried zeolites into fine powder, which was then transferred into plastic holders and put into the instrument. Only mid synthesis or non-calcined samples were analysed.

3.2.2. Nitrogen physisorption

Nitrogen adsorption/desorption isotherms were measured on a Micromeritics 3Flex volumetric Surface Area Analyzer at -196 °C to determine surface area, micropore volume and total pore volume. Before measurements, all samples were outgassed under the turbomolecular pump vacuum using a Micromeritics Smart Vac Prep instrument; starting at an ambient temperature up to 110 °C with a heating rate 1 °C/min until the residual pressure of 13.3 Pa was achieved. After heating at 110 °C for 1 h, the temperature was increased to 250 °C (1 °C/min) and maintained for 8 h. The specific surface area (SBET) was calculated by the BET method [53], [54] using adsorption data in the range of a relative pressure p/p0 = 0.05-0.20. The t-plot method [53], [55] was used to evaluate the volume of micropores (Vmic) and external surface area (Sext). The adsorbed amount at relative pressure p/p0 = 0.95 reflects the total adsorption capacity (Vtot).

3.2.3. Diffuse Reflectance Fourier Transform Spectroscopy

The experimental DRIFT (Diffuse Reflectance Fourier Transform) spectra were obtained using a Jasco model 4x spectrophotometer, equipped with Jasco's DRIFT accessory model DR PRO 410MX. Both the background and samples' spectra were taken in absorbance mode with a resolution of 2 cm^{-1} and 256 scans in the wavenumber region 4000 to 350 cm^{-1}. The analysed samples were diluted in high purity KBr, using 50 mg for 2.5 g of sample.

3.2.4. Inelastic Neutron scattering spectroscopy

The INS spectra were measured using Lagrange, the neutron vibrational spectrometer installed on the hot source of the high-flux reactor at the Institut Laue–Langevin in Grenoble during the missions of projects DIR-170 and DIR-290 by their respective teams [56], [57]. Samples, with about 2 g mass, where sealed in an aluminium cell and adapted to a stick with vacuum line access. Prior to measurement, the samples were kept in a cryofurnace at 90 ºC and 10^{-5} bar during 6h to dehydrate. The INS spectra were recorded at 10 K over the range of energy transfer from 100 to 1500 cm^{-1} with the Cu220 monochromator, which has an energy resolution of $\Delta E/E \approx 2\%$.

3.2.5. Solid state NMR measurements

^{1}H and ^{27}Al spectra were acquired on a Bruker Avance III 700 spectrometer operating at B_0 field of 16.4 T, with ^{1}H and ^{27}Al Larmor frequencies of 700.1 and 182.4 respectively. ^{29}Si spectra were acquired on a Bruker Avance III 400 spectrometer operating at B_0 field of 9.4 T with Larmor frequency of 79.5 MHz. All experiments were recorded on double-resonance 4 mm Bruker MAS probes except for the ^{27}Al 3Q MAS spectra, acquired on a double-resonance 1.3 mm Bruker MAS probe (B_0=16.4 T). The samples were packed into ZrO_2 rotors with Kel-F (4 mm) or Vespel (1.3 mm) caps in the B_0 fields of 9.4 and 16.4 T, respectively. Spinning rates between 5 and 50 kHz were employed to record all spectra. Chemical shifts are quoted in ppm using the following secondary references: solid adamantane (1.85 ppm), aqueous solution of $Al(NO_3)_3$ (0 ppm) and solid Q8M8 (-109.68 ppm for the furthest upfield resonance) for ^{1}H, ^{27}Al and ^{29}Si, respectively. The deconvolution and simulation of the NMR spectra were carried out using the program Origin.

^{1}H single-pulse MAS NMR spectra were acquired at a spinning rate of 15 kHz using a 3 µs pulse (90° flip-angle) that corresponds to a radio frequency (rf) field strength of *ca.* 83 kHz and a recycle delay (RD) of 5 s. The ^{1}H spectra were acquired for both the fully hydrated (placed in a relative humidity 100% saturator for 48 h prior to NMR measurement) and dehydrated (90 ºC) zeolites.

^{27}Al single-pulse MAS NMR spectra were acquired at a spinning rate of 15 kHz using a quantitative pulse of *ca.* 0.33 µs (10° flip angle) corresponding to a rf field strength of 83 kHz and a recycle delay of 2 s. ^{29}Si single-pulse MAS NMR spectra were acquired at a spinning rate of 5 kHz using a 3 µs pulse (40° flip angle) corresponding to a rf field strength of *ca.* 40 kHz, and a RD of 60 s.

^{27}Al 3Q (triple quantum) MAS experiments were recorded with a MAS rate of 50 kHz and a z-filter sequence for the triple quantum correlations. A ^{27}Al 90º selective pulse with 16.6 µs length and 5 kHz rf field was employed. The multiple-quantum excitation and

reconversion blocks used a rf equal to 156 kHz, and their length was optimized directly on each sample and was around 3 and 1 μs respectively. RD was set to 200 μs and 64 indirect transients were collected with a spectral window equal to 50 kHz (rotor synchronized acquisition).

3.2.6. DFT optimization and spectra simulation

MFI framework

Periodic density functional theory (DFT) calculations were carried out using the plane wave pseudopotential method, as implemented in the CASTEP code (version 17.21), running on SCARF High Performance Computing cluster under the access of Dr. Mariela Nolasco [58]–[60]. Exchange and correlation were approximated using the PBE functional within the generalized gradient approximation (GGA) [61]. The plane-wave cut-off energy was 830 eV. Brillouin zone sampling of electronic states was performed on the 1 × 1× 1 Monkhorst-Pack grid. The equilibrium structure, an essential prerequisite for lattice dynamics calculations, was obtained by BFGS geometry optimization, after which the residual forces converged to ±0.00087 eV.$Å^{-1}$. Phonon frequencies were obtained by diagonalization of the dynamical matrix, computed using density-functional perturbation theory. The atomic displacements in each mode, which are part of the CASTEP output, enable visualization of the modes to aid assignments and are also all that is required to generate the INS spectrum using the program AbINS ([62], a part of Mantid package [63]).

The structure provided for optimization and spectra simulation corresponded to a segment of the MFI framework with a total of 578 atoms and a Si/Al ratio of 191, containing one Bronsted acid site.

EFAL

The selection of various structures to simulate possible EFALs was based on the more prominent proposed species in the literature, being represented in **Figure 16** [9], [64], [65]. All the calculations for structure optimization and simulation of the vibrational spectra were done utilising the software Gaussian 16 in the Argus computational cluster [66]. The theoretical model and basis set chosen were, respectably, B3LYP (Becke Lee-Yang-Parr) and 6-311++g(d,p) (also known as 6-311++g**), considering their relative accuracy and speed of computation [67], [68]. All optimized structures were considered as real minimums, with no imaginary frequencies. The obtained theoretical frequencies were scaled by a factor of 0.96 to compensate some of the model's approximations, and better simulate the experimental spectra. The scaling factor value for the specific combination of theoretical

model and basis set used was not found on the literature [69], and so the value used had to be based on similar models and sets. As such, 0.96 was taken as a safe estimate. The atomic displacements in each mode enable visualization of the modes to aid assignments and are also all that is required to generate the INS spectrum using the program AbINS ([62], a part of Mantid package [63]).

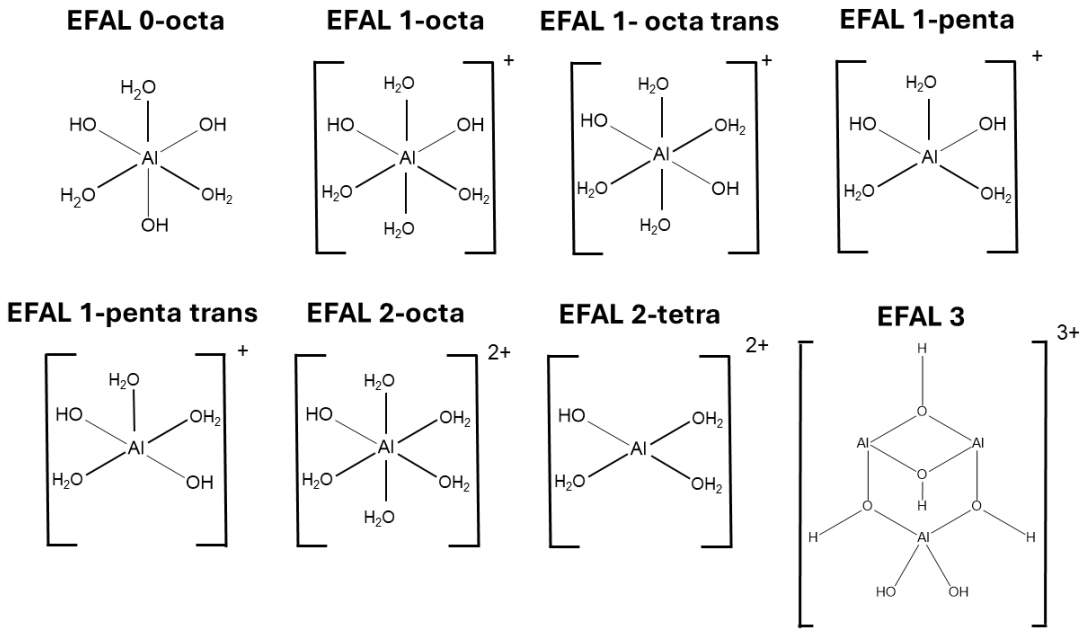

Figure 16. Structures of the simulated possible EFALs.

4. Results and discussion

4.1. 2D layered zeolites: synthesis and characterization

4.1.1. Bifunctional structure directing agents

The synthesis of the three bifunctional SDAs, 18-N_3-18, 18-N_4-18 and 18-N_5-18 was carried out, followed by the acquisition of liquid state ^{1}H NMR for the two first synthesis of 18-N-Br and 18-N-N (batches i and ii), as well as for the first 18-N_3-18 synthesis (batch i) to follow the reaction (spectra in appendix B). The spectra of both batches present good agreement between each other, and when compared with 18-N_3-18, the latter shows fewer distinct peaks, a sign that the reaction proceeded as intended. This is because this molecule has higher symmetry than the other two, and so, instead of their reaction generating a more complicated spectra, previously chemically inequivalent protons now present the same chemical shift.

With these promising results and the procedure staying the same, no further NMR data were acquired to follow the reaction. However, when the reaction yields were calculated, shown in **Table 2**, some issues arose.

Table 2. Yields of the various reactions performed for SDA synthesis; represented as percentages (%).Three batches of 18-N_3-18 (i,ii and vi), two of 18-N_4-18 (iii and iv) and one of 18-n5-18 (vi) were obtained, in which the necessary intermediary products were synthetized, with their respective yields also being presented.

	18-N-Br	18-N-N	18-N_3-18	18-N-N-N	18-N_4-18	Br-N-N	18-N-N-N-N	18-N_5-18
batch i	17.1	16.6	46.4	———	———	———	———	———
batch ii	85.8	77.4	51.8	———	———	———	———	———
batch iii	43.1	35.9	———	———	57.1	———	———	———
batch iv	183.1	127.5	———	73.9	129.6	———	———	———
batch v	151.0	197.2	———	———	———	93.5	47.4	73.0
batch vi	186.3	106.8	92.8	———	———	———	———	———

Although fluctuating significantly, the yields for the first three batches are reasonable. From batch iv onwards however, all 18-N-Br and 18-N-N yields were above 100%. No changes were made to the procedure, equipment or reagents used between batches, making this discrepancy quite strange. This is concerning, as it possibly jeopardizes all the following SDAs synthesis steps. Indeed, looking at the remaining yields they are quite high, with the third attempt at 18-N_3-18 presenting almost double the yield as the previous tries (92.79%), and 18-N_4-18 prepared via the three-step pathway (batch iv) presenting a yield above 120%. Unfortunately, because of time constraints it wasn't possible

to perform liquid-state NMR and other tests on the anomalous samples, as well as tightly control replicas of the synthesis to try and ascertain possible causes of such discrepancies.

4.1.2. 2D layered surfactant templated zeolites' synthesis and structure analysis

Various 2D layered zeolites synthesis utilizing the various prepared SDAs were attempted. Two of them used 18-N_3-18, as during the aging of the first one the gel was accidently overheated, leading it to boil and spill over slightly. The gel was recovered and still used for hydrothermal synthesis, but a parallel reaction using the same SDA was also performed to "correct" the accident. However, a leak occurred in the oven during this second synthesis, losing some of the gel's liquid fraction. There were two syntheses using the different 18-N_4-18, the two-step and three-step pathway respectively. One synthesis was also performed utilizing 18-N_5-18. Other syntheses were started, but I couldn't be present to follow and finish them, with their characterization not being performed in time to include in this work. Three synthesis of traditional 3D ZSM-5 were also performed.

All of them were followed by taking small samples and analysing by XRD, from which all the 3D zeolites presented the expected fully crystalline spectra of ZSM-5 after 2 days. For the 2D layered zeolite synthesis only the one using the two-step 18-N_4-18 and 18-N_3-18 which didn't leak presented XRD patterns with any level of crystallinity, after 8 and 11 days respectively. All the other synthesis yielded completely amorphous products. This once again highlights the anomality that occurred during SDA synthesis, as only the reactions utilizing the SDA from batches i through iii were successful, with all other originating non-crystalline solids.

The crystalline samples have their XRD patterns illustrated bellow (Figure 17).

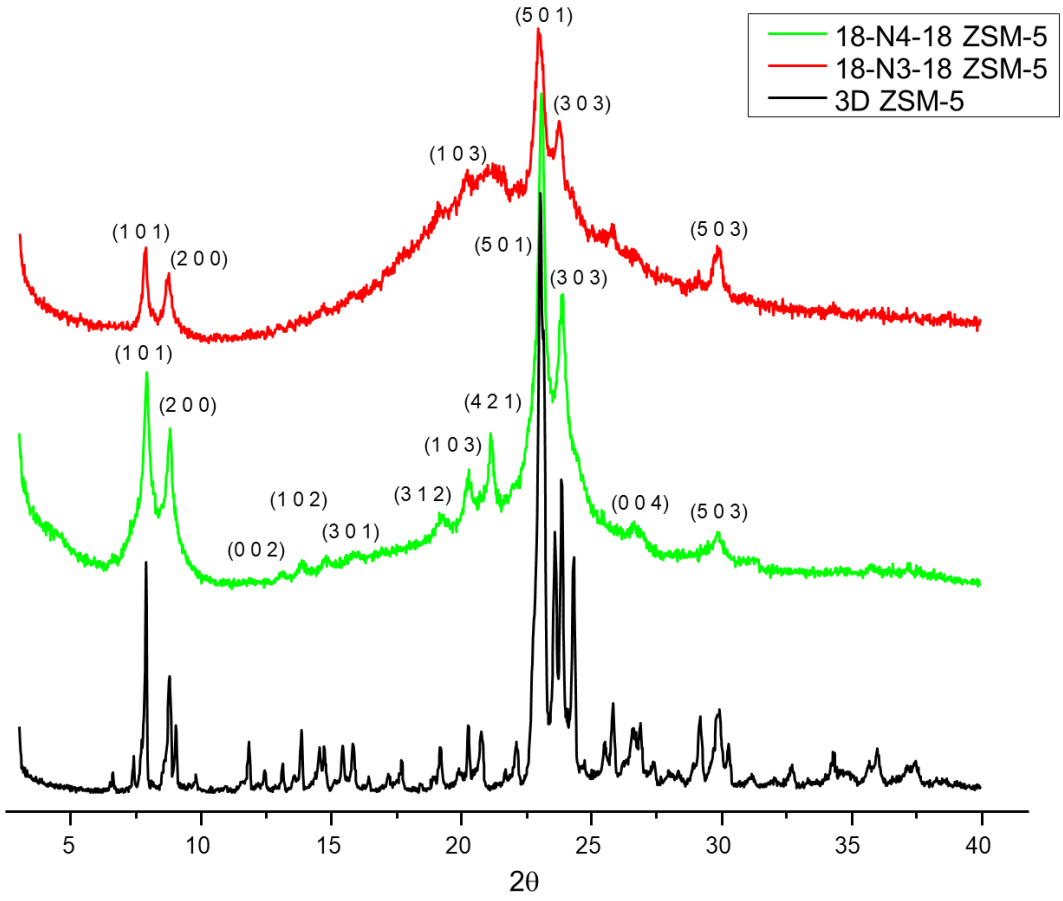

Figure 17. XRD patterns of 3D ZSM-5 and 2D layered ZSM-5 utilizing 18-N_3-18 and 18-N_4-18 as SDA. Miller indices have been highlighted for the peaks of 2D zeolites.

From now on the zeolite samples will be identified by their corresponding SDAs or as 3D for the traditional 3D framework. Looking first at 3D's pattern, it matches well with data available in the literature, indicating that its synthesis was successful [18], [21], [23], [70]. In the 2D samples' patterns is clearly visible that 18-N_3-18 is only semi-crystalline, presenting some clearly defined bands, above the big broad one centred around 22°. One possible explanation is the incident that occurred during aging, which may have changed the reagents ratios, as well as partially degraded the SDA. 18-N_4-18 on the other hand seems to be much more crystalline, presenting better defined bands and a lower "baseline".

Previous studies have shown that the ZSM-5 nanolayers wide side is parallel to the ac plane of the crystal's unit cell, presenting h0l reflexions with very sharp peaks since these planes are mostly unaltered from the 3D framework. The layer's thinner side is aligned along the b axis with a minimum average thickness of 1.5 nm, corresponding to a single micropore layer. As such, hkl planes with k≠0 will be absent or very ill defined since the zeolite nanosheets are very thin along this direction [18], [19]. The samples' reflections, shown

near their respective peaks in **Figure 17**, were assigned based on comparison with simulated XRD data from ZSM-5 containing tetrapropylammonium, being the closest available analogue to the 3D ZSM-5 sample [70]. It can be clearly seen that the expected pattern with only h0l peaks is observed, matching with ones available in the literature [23]. The only exceptions are the (3 1 2) and (4 2 1) reflections visible for 18-N_4-18, which could be due to the presence of the SDA, since the sample wasn't calcined before analysis. Once again, due to time constraints XRD couldn't be performed for the calcined samples.

Taking into account the different arrangements of the layers (multilamellar, unilamellar/disordered, pillared, hexagonal, etc) the XRD patterns most closely resemble the ones from multilamellar and/or unilamellar structures when compared to layers in hexagonal arrangements, whose peaks were much broader and less defined [19], [23]. This is interesting as the synthesis procedure followed was for the hexagonal assembly. Looking at the differences between the two approaches, one was synthesis time which shouldn't be the defining factor as the reactions were followed at least every two days by XRD and stopped based on those results, and not on the procedures time. The other difference is in the gel composition, where the multilamellar procedure's gel had a 100 Si/Al ratio, 1.0 mol of SDA, 1070 mol of water and 0 mol of ethanol compared to 20 Si/Al ratio, 1.5 mol of SDA, 2132 mol of water and 240 mol of ethanol.

Nevertheless, the obtained materials are 2D layered ZSM-5, and so they were taken for further characterization.

4.1.3. Nitrogen physisorption analysis

By looking at the shape of the isotherm, a material can be classified into different archetypal types, yielding information about the sample's structure [71]. Bellow in **Figure 18** are represented the nitrogen isotherms of the 18-N_3-18, 18-N_4-18 and 3D zeolite samples.

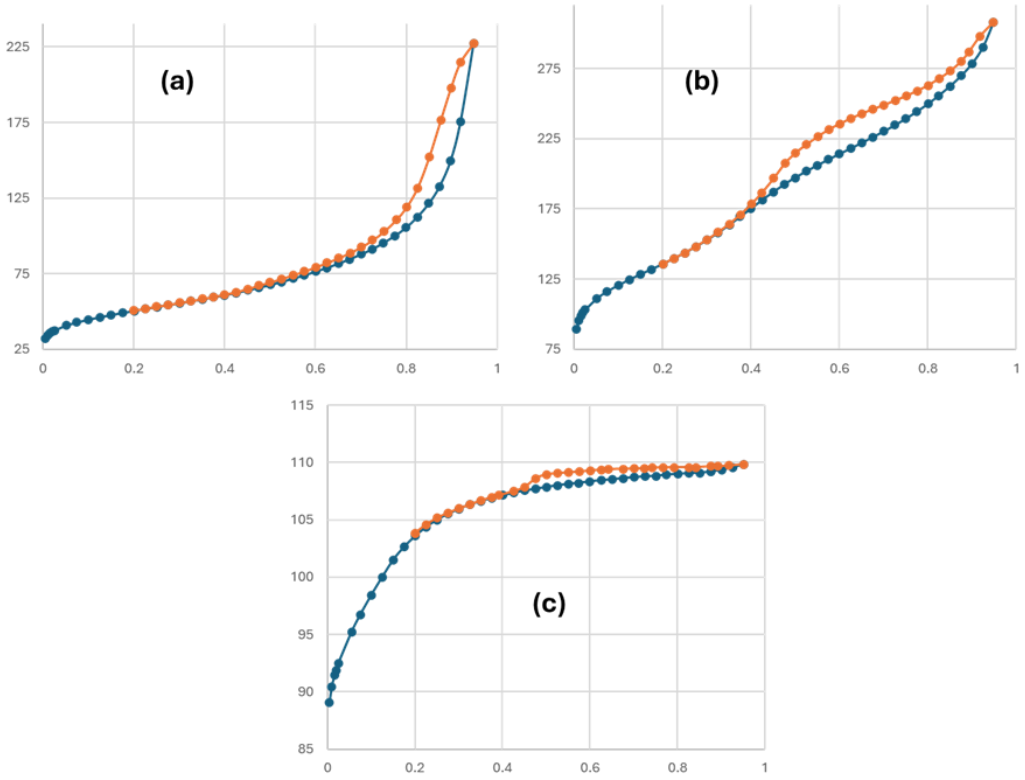

Figure 18. N_2 isotherms of 18-N_3-18 (a), 18-N_4-18 (b) and 3D (c) samples. The y-axis represents the quantity of nitrogen adsorbed (cm^3/g STP) and the x-axis relative pressure (p/p°). The blue and orange points represent the adsorption and desorption lines respectively.

3D ZSM-5 presents a type I isotherm, characteristic of microporous materials, with a step gas uptake rapidly reaching a plateau due to micropore filling. More specifically, it presents a type Ib isotherm, characteristic of materials with a broader pore size distribution, wider micropores and possibly some small mesopores, causing pore saturation to occur at higher pressures than in type Ia isotherm [71]. ZSM-5 seems to usually display a type Ia isotherm, which has narrower micropore distribution and dimensions than type Ib, although type Ib materials can also be found, supporting the successful synthesis indicated previously by XRD [23], [72]–[75].

Looking at the 18-N_3-18 and 18-N_4-18 isotherms, they clearly present hysteresis loops, which are a combination of H3 and H4 type hysteresis loops, with 18-N_3-18 presenting a stronger H3 behaviour than 18-N_4-18. Both H3 and H4 are often associated with “non-rigid aggregates of plate-like particles”, which is exactly the structure of the expected nanosheets [71]. For these types of samples both loops normally present a more pronounced gas uptake at low pressures due to micropore filling. The biggest difference between the two loop types is the behaviour at higher pressures, resulting from the

presence of ordered mesostructures in H4 type samples, be it more traditional mesopores or interlayer/interparticle mesopores [21], [71]. Looking at examples from other groups, multilamelar and pillared assemblies of nanosheets have more regular structures with a narrower distribution of mesopores sizes, presenting isotherms closer to type H4, while unilamellar and self-pillared assemblies have a more disordered assembly of 2D nanosheet layers, with a broader mesopore size distribution (although not random), being closer to type H3 [18], [21], [23]. Hexagonally ordered assemblies seem to present distinct behaviour, with their isotherms being similar to type IVa which instead of plateauing at higher pressures, gas adsorption steeply increase [71]. This 3 step shape is explained as micropore filling, followed by capillary condensation in the mesopores, and ending with a sharp gas intake due to condensation in the interparticle void volume [19]. Based on this, both 2D zeolites seem to have a unilamellar/ disordered structure, with 18-N_4-18 seeming to be a mixture of unilamellar and multilamellar. Transmission electron microscopy (TEM) would be needed to confirm these assignments, however due to time constraints it was not possible to acquire such data.

Based on the isotherms data, the specific surface area (SBET), the volume of micropores (V_{mic}), external surface area (S_{ext}) and total adsorption capacity (V_{tot}) were determined, being presented in **Table 3**.

Table 3. N_2 isotherm analysis.

Zeolite samples	SBET m^2/g	Sext m^2/g	Vmic cm^3/g	Vtot cm^3/g
18-N_3-18	178	127	0.02	0.35
18-N_4-18	477	340	0.06	0.47
3D	354	19	0.16	0.17

Comparing my samples with data from similar materials, the values for 3D zeolite seem to be within the expected intervals: SBET surface around 311-420 m^2/g; V_{mic} close to 0.101-0.149 cm^3/g and V_{tot} around 0.184-0.222 cm^3/g [23], [43], [74], [75]. The 2D samples however show a very big deviation. For materials using gemini SDAs with three ammonium groups, or single carbon chain surfactant SDAs with two ammonium groups, SBET surfaces of 520-1190 m^2/g and V_{tot} of 0.96-1.58 cm^3/g are reported, which are significantly bigger than the values obtained for 18-N_3-18 [18], [19], [23]. For materials using gemini SDAs with four ammonium groups, SBET surfaces of 940-1060 m^2/g and V_{tot} of 1.24-1.48 cm^3/g are reported, again significantly bigger than the obtained values for 18-N_4-18 [19].

For 18-N_3-18 the presence of the amorphous phase detected by XRD could help explain this discrepancy, greatly reducing micro-and mesopore volume as well as their respective surface area. In the case of 18-N_4-18, its synthesis used the solid from the two-step pathway, which utilized an excess of solid reagent 18-N-Br. As such, it is expected that the final solid contains at minimum the added amount of 18-N-Br minus the amount of N,N,N',N'-tetramethyl-1,6-diaminohexane (limiting reagent), which was five times less. This rationale was considered in the presented 57% yield (the yield considering all the final solid as the desired product is 185%), were from 2.29 g of the total solid product, at least 1.58 g are from 18-N-Br. This is problematic as for "typical" surfactant SDA, the minimal number of ammonium groups needed for the molecule to act as a porogenic agent is two, with a lower number not allowing the generation of a zeolite framework, but forming a non-porous layered silicate phase [18], [20], [23]. As such a possible cause for the anomaly in my sample is that when it came to add the SDA during synthesis, the amount of 18-N_4-18 was much lower than expected, adding a lot of 18-N-Br instead. The 18-N_4-18 present generated ZSM-5 nanosheets, which gave rise to the intense peaks matching the expected XRD pattern. Looking at literature reports, different silicate phases can be formed depending on the single ammonium group molecule in question, but the structures usually are not amorphous, yielding well defined peaks in XRD. This could allow their presence to not became immediately obvious in the XRD patterns, as the sample would still be crystalline. It could also be the origin of the peaks from apparent reflexions with $k \neq 0$ [20], [76]. Their non-porous nature will however reduce the pore volume and surface area of the resulting solid.

Comparing my own samples with each other, the BET surface area, which includes internal surface area in the presence of micropores, should increase with decreasing particle size. As such, the transition from a 3D framework to the 2D layered form should lead to surface area increase, and so the relation seen should be SBET surface area 18-N_3-18 > 18-N_4-18 >3D. With the amorphous part contaminating the 18-N_3-18 sample the pattern is broken, still holding up for 18-N_4-18 and 3D samples. The mesopore and micropore volume changes should also follow a clear pattern. The 3D structure has the expected low mesopore and high micropore volume, while 18-N_4-18, with the formation of nanosheets can be thought as the 3D structure sliced into various layers, leading to less micropore and more mesopore volume. Since 18-N_3-18 has even thinner nanosheets its mesopore volume should be even higher, and micropore volume even lower. The micropore tendency is observed, and the mesopore one is followed by 3D and 18-N_4-18, but once again 18-N_3-18 breaks the pattern.

4.2. EFAL and H-ZSM-5: some insights

4.2.1. H-ZSM5 and EFAL simulations

From the CASTEP simulation of the ZSM-5 framework, the following infrared and INS spectra were obtained (**Figure 19**).

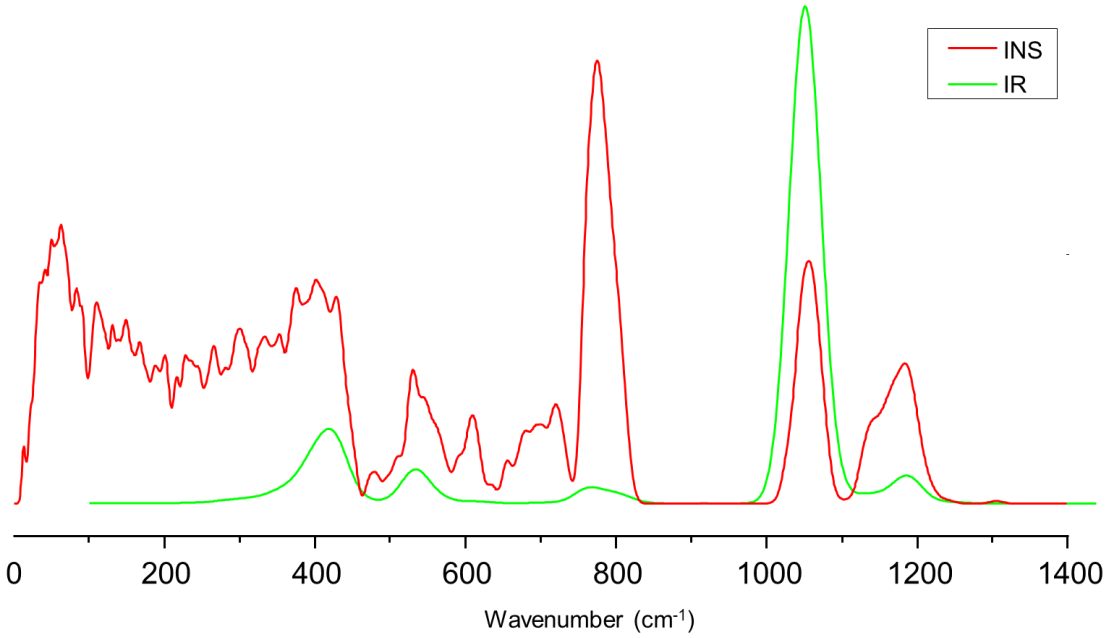

Figure 19. Simulated infrared and INS spectra of H-ZSM-5.

As previously mentioned, one advantage of INS is the level of accuracy to which we can predict the spectral intensities, but it also enables the decomposition of the spectrum into the contributions of each element, clearly identifying which species are involved in which vibrational mode. This is relevant as the modelled framework has 191 silicon atoms for a single aluminium atom, a Si/Al ratio much bigger than the 15 from the studied samples, and so the signal from aluminium will be underestimated. For this reason, I adjusted the spectra in **Figure 20** to be the sum of the Si and O contributions, plus the original signal from Al multiplied by 12.73. This approximation is far from ideal, as silicalite's (pure silica MFI framework) orthorhombic unit cell has 96 total tetrahedral sites, with 12 crystallographic inequivalent ones [77]. When aluminium atoms start being introduced, the symmetry is further broken down, creating more inequivalent sites that at the highest extreme may create 96 inequivalent T sites. Thus, not only will the aluminium be introduced in inequivalent positions, yielding slightly differing vibrational modes, but they will also influence the other atoms vibrations. Still, it allows for a better understanding of the scale with which aluminium contributes to the overall spectrum, being a useful approximation.

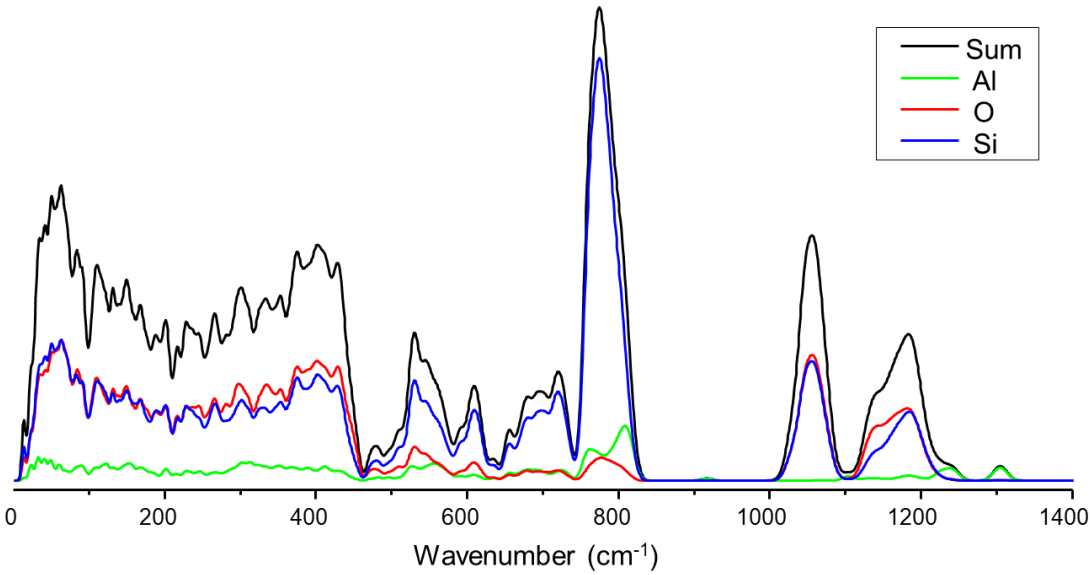

Figure 20. Deconvolution of H-ZSM-5's simulated INS spectrum into its atomic contributions. Si/Al ratio has been "corrected" to 15 by scaling Al signal by 12.73.

Focusing on the region above 400 cm^{-1}, spectrum assignment of the major vibrational modes was performed, where the JMOL software allowed to visualize the CASTEP file containing the vibrational mode and respective frequency. The assignment is presented in **Table 4** and is consistent with others made in the literature, although the identification of more localized vibrations, like in the double five-membered rings for example, was too ambiguous to claim with certainty [42], [43], [47], [78].

Table 4. Vibrational modes of the simulated H-ZSM-5 framework.

IR (cm^{-1})	Vibration	INS (cm^{-1})
	O-T-O bending	401
421	O-T-O bending	
531	O-T-O bending	530
	O-T-O bending	544
	O-T-O bending	609
	O-T-O bending	655
	O-T-O bending	679
	Symmetric T-O-T stretching	695
	Symmetric T-O-T stretching	720
767	Symmetric T-O-T stretching	774
1051	Assynmetric T-O-T stretching	1055
	Assynmetric T-O-T stretching	1142
1188	Assynmetric T-O-T stretching	1183
	Assymetric O-Al-O stretching (local)	1237

Regarding the EFAL structures, all converged successfully while maintaining the desired geometries, and their respective infrared and INS spectra were generated (available in appendix C).

4.2.2. Infrared and INS spectroscopy results

When comparing the calculated spectra with the experimental ones (shown in **Figure 21**) there seems to be a good general agreement, thus allowing a sound and mostly direct assignment of the observed vibrational bands.

For comparison, the z15-ns sample was chosen for infrared spectra while for INS z15-600 was chosen, as it was the H-ZSM-5 sample with higher signal to noise ratio (discussed further in INS section).

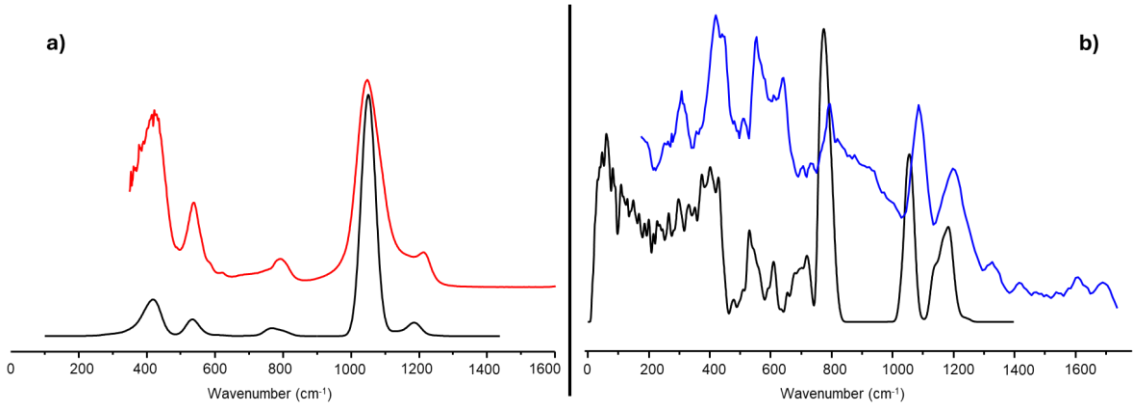

Figure 21. Comparison between calculated (black) and experimental (coloured) spectra for H-ZSM-5 zeolite. Calculated spectra from CASTEP model. For illustration purposes only, the experimental spectra refer to: a) INS of z15-600 sample after dehydration; b) Infrared of z15-ns sample.

Infrared spectroscopy

The obtained DRIFT spectra of the MFI samples are represented in **Figure 22**. Starting by performing spectral assignment of the major bands, the ones around 452 cm^{-1} and 546 cm^{-1} correspond to O-T-O bending (where T is either Si or Al); the ones close to 796 cm^{-1} to symmetric T-O-T stretching and the bands around 1098 and 1219 cm^{-1} to asymmetric T-O-T stretching [42], [43], [47], [78], [79]. Since the available setup didn't allow for measurement of dehydrated samples, the bands around 1628 cm^{-1} most likely arise from water inside the structure. The bands between 1800 and 2000 cm^{-1} correspond to overtones and or combination bands of the aforementioned stretching modes [80]. Around 2970 cm^{-1} small peaks normally attributed to alkyl stretching can be seen, which shouldn't be present in a zeolite sample. They most likely arise from some SDA and its fragments that weren't

fully removed after the calcination and washing. The OH stretching region from 3000 to 3800 cm^{-1} is a very broad band due to the presence of water in the samples, hindering the study of the OH vibrational modes arising from EFALs, hydroxyl nests and bridging hydroxyl groups.

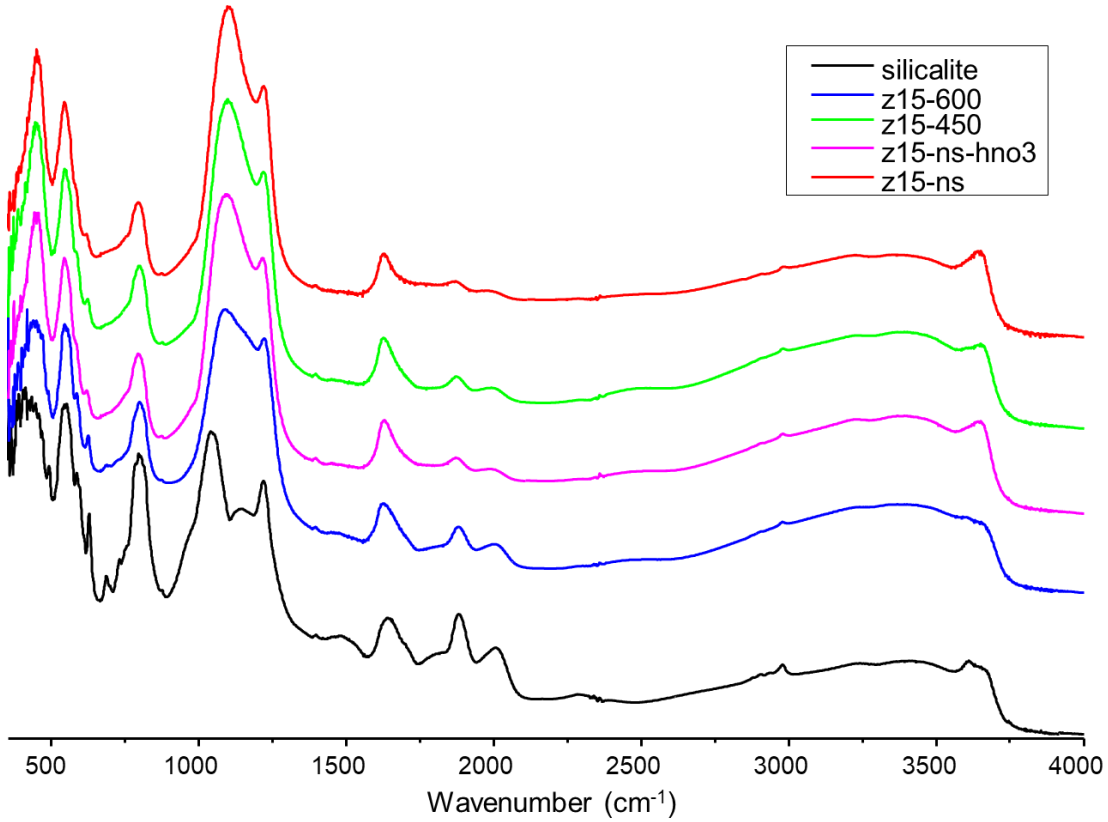

Figure 22. DRIFT spectra of the MFI samples.

Even though all samples have the same framework, their composition is quite diverse, containing different amounts of aluminium and in different forms, different extent of defects due to dealumination, etc. This means no band can be considered unchanged in all different spectra, not allowing spectral normalization and consequent band intensity comparison between the different materials. Even weighing the same amount of sample to try to directly compare the "raw" intensities is sketchy, as the samples have different chemical compositions, meaning that equal mass doesn't equate to the same amount of framework. Consequently, only shifts in band frequency can be compared between the different materials.

Analysing the spectra, the region between 400 and 1350 cm^{-1}, represented in **Figure 23**, contains the most prominent and distinct features. First, in the 900 to 1350 cm^{-1} region silicalite presents three bands alongside a shoulder, while all H-ZSM-5 only have two

distinct bands. This may seem confusing at first as silicalite is the more chemically simple material, not containing any EFAL species or aluminium atoms, and so one would expect more features in the H-ZSM-5 samples. However, as was previously mentioned, the presence of only Si in silicalite introduces higher symmetry in the structure, causing more of the vibrational modes to have similar frequencies and therefore a more well resolved spectra with more intense sharper bands. The inequivalent sites created by Al introduction will cause the various similar vibrational modes to diverge, creating broader bands that drown the finer details. This would also explain the various smaller bands present in silicalite that seem to disappear in the other samples, like the one around 685 cm^{-1}. Regarding the appearance of EFAL species, as band intensities can't be compared between spectra, their detection can only be made by the appearance of new bands with dealumination. That is not verified in any of the samples, in fact the opposite is true due to the symmetry argument, which means that EFAL species signal and concentration isn't high enough to cause the appearance of clear new bands.

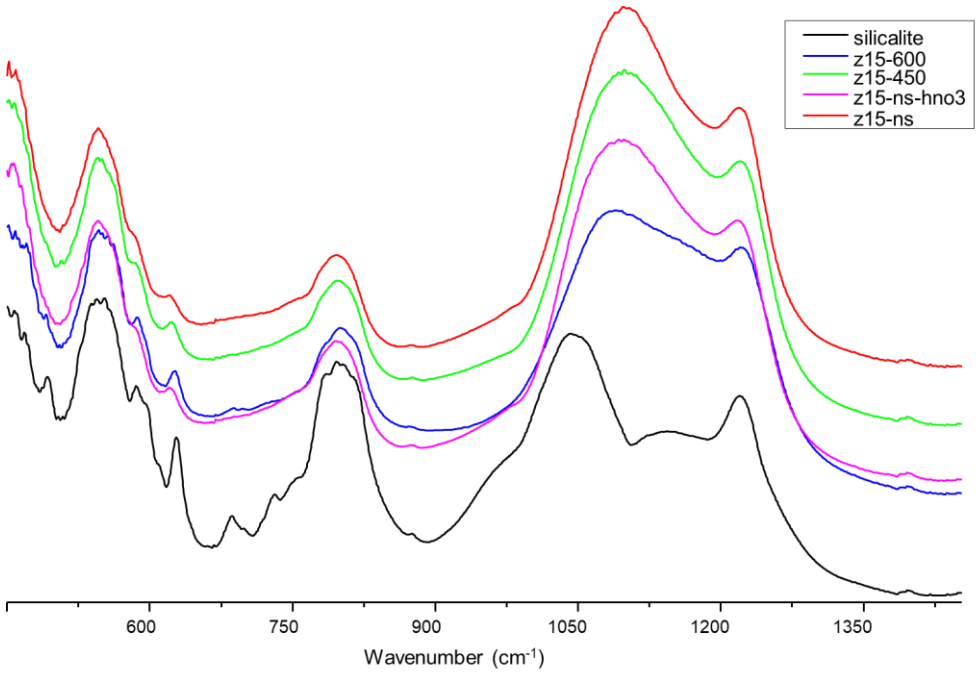

Figure 23. DRIFT spectra of the MFI samples in the 400 to 1400 cm^{-1} region.

Focusing on the frequency of the bands, a clear pattern can be identified. Taking the bands between 1040 to 1100 cm^{-1} as an example (better seen in **Figure 23**), silicalite and z15-ns bands differ the most, with a 60 cm^{-1} difference. In between these two, the vibrational peaks of the other samples seem to be shifting towards silicalite with increasing

dealumination, with z15-450 and z15-ns-hno3 presenting similar peak values, while z15-600's peak is even closer to silicalite's. This pattern, silicalite, z15-600, z15-450/z15-ns-hno3 and then z15-ns, can be interpreted as the removal of aluminium from the ZSM-5 framework moving the structure closer and closer to silicalite, causing the bands to start to shift towards silicalite's bands.

INS spectroscopy

Although a very powerful technique INS is also quite expensive, requiring a neutron beam and all the associated equipment, and so it should not be applied to a sample unless there is a strong argument behind it. INS intensities are proportional to the atomic scattering cross section, and since H has a large value (82.03 barn), spectra of H containing materials tends to be dominated by its vibrational modes. Zeolite samples are mainly composed of Si (2.78 barn), O (4.2 barn) and Al (1.503 barn), with a small amount of H from surface and defect silanols, and so the signals arising from framework H should be relatively weak [46]. Most of the proposed structures for EFAL however contain hydroxil groups, and so when EFAL are formed, their vibrational modes associated with H may become clearly visible, allowing for their detection [9], [64], [65]. Beyond simply detecting their formation, another reason for the use of INS is the accurate band intensity prediction, which allows to simulate the INS spectrum of various possible EFAL and compare them with the dealuminated experimental samples to determine their possible presence or absence based on the new dealumination bands.

For this purpose, the samples had to be previously dehydrated, as otherwise the signals arising from water would drown the EFAL species' bands, as well the framework bands. This is clearly visible in **Figure 24**, where the spectra of hydrated and dehydrated z15-600 samples are represented. For the dehydrated sample various bands can be identified, in contrast to the hydrated one, were the broad water band erases almost all spectral details.

With all this in mind, the spectra of the dehydrated MFI samples are presented in **Figure 25**.

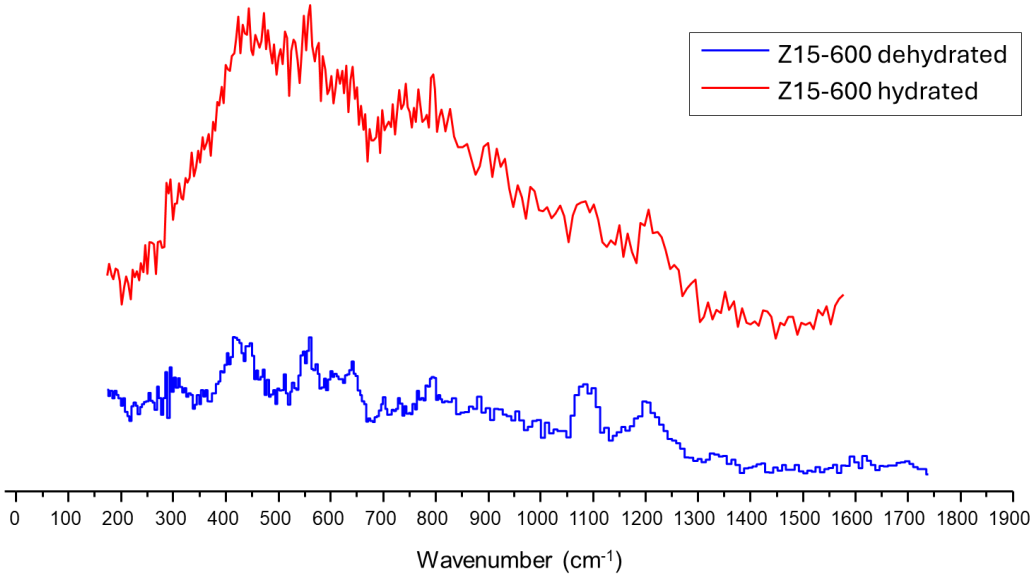

Figure 24. INS spectra of hydrated and dehydrated z15-600 samples.

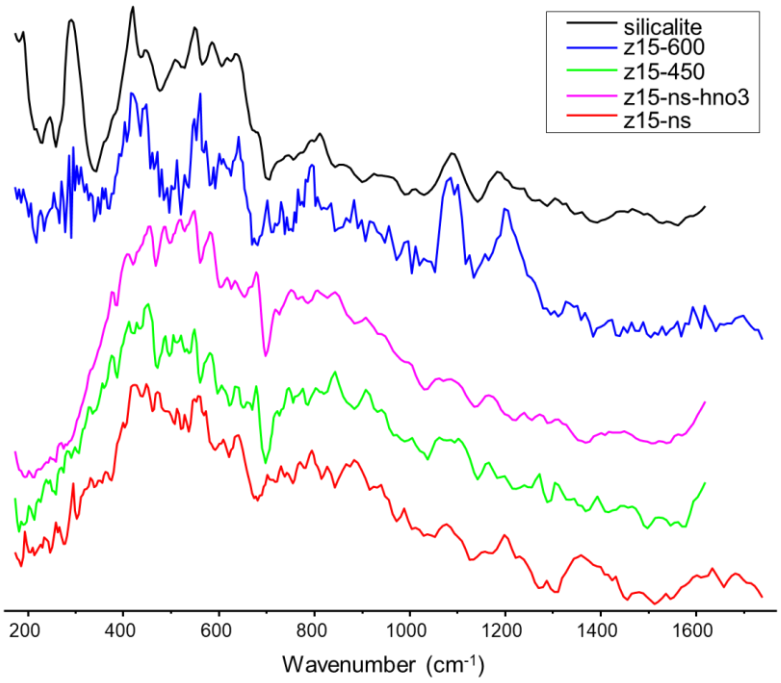

Figure 25. INS spectra of dehydrated MFI samples.

Similar to the DRIFT spectra, band intensities can't be compared between spectra of different samples, only frequency shifts can be analysed. Although all samples were dehydrated it is very difficult to clearly distinguish between noise and signal, apart from z15-

600 and silicalite. The broad “background” shape matches with the theoretical calculations, with the major bands being centred around 400, 600, 800 and the 1000-1200 cm^{-1} region, but the actual bands are ill defined, especially for z15-ns, z15-450 and z15-ns-hno3, and not seeming to follow any particular pattern. As an example, let the focus be on bands in the 1200 cm^{-1} region. In the infrared analysis a trend was identified where the bands were shifting from z15-ns to silicalite with dealumination removing framework Al. That doesn’t seem to be the case here, where band frequency seems to be decreasing in the order z15-600, z15-ns, silicalite, z15-450, z15-ns and z15-ns-hno3 as seen in **Figure 26**, seemingly a random order.

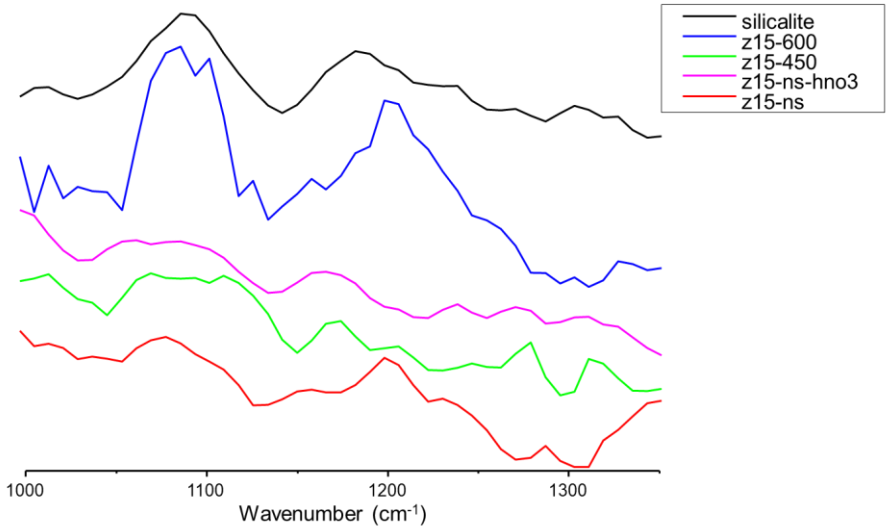

Figure 26. INS spectra of the MFI samples in the 1000 to 1300 cm^{-1} region.

This noise issue also makes the correlation of EFAL structures to features appearing with dealumination a fool’s errand, since the concentration and signal intensity of the EFAL species wasn’t high enough to create clearly observable new bands in the dealuminated samples’ spectra. The observed differences between spectra aren’t defined enough to be clearly identified as real sample signal and not noise, and so, just as in the DRIFT spectra, no EFAL bands could be identified and correlated with the simulated structures.

The most likely culprit of this signal to noise ratio problem is an incomplete dehydration process, following the information contained in **Figures 24** and **25**, indicating that samples z15-ns, z15-450 and z15-ns-hno3 still contain significant water content. This situation couldn’t be corrected due to limitations in the access to the neutron source.

One thing to note is that the various possible EFAL structures were optimized in isolation, but the path taken by most researchers seems to also include a small segment of

the zeolitic framework along the EFAL structure [81]–[83]. Although more computationally demanding, the inclusion of only a small framework segment will much more accurately describe and predict these structures as EFAL don't exist in vacuum, interacting with the surrounding framework. Double quantum ^{27}Al and double quantum ^{1}H NMR experiments support this approach, as they have shown that EFAL species not only have a tendency to be near Bronsted acid sites, but sometimes even near each other [81], [83], [84]. The available computational cluster and timeframe was not enough to follow this approach, however, an illustrative simulation was performed by adding a 4 SiO_2 chain alongside EFAL3, as can be seen in **Figure 27**, together with the respective infrared spectra.

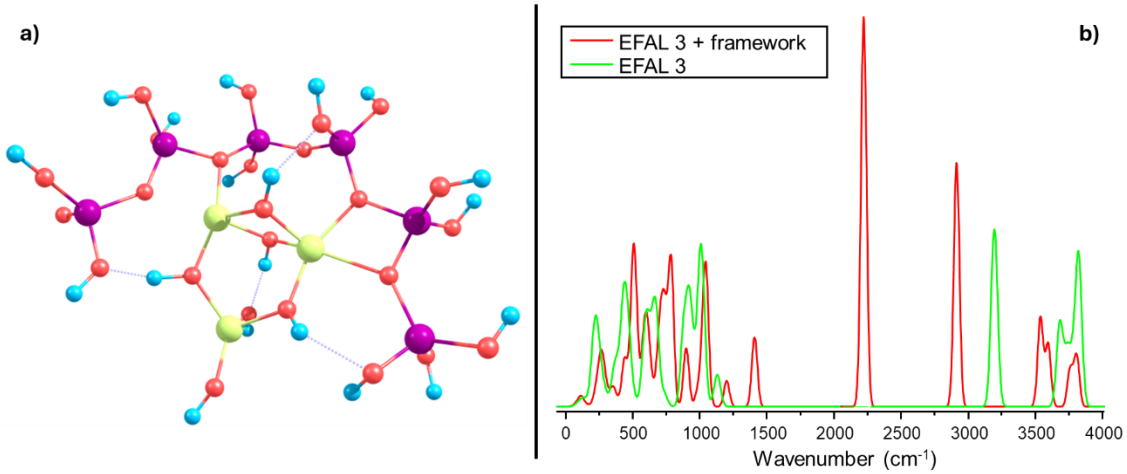

Figure 27. (a) EFAL 3 alongside four silicon SiO_2 chain. Yellow, purple, red and blue spheres represent aluminium, silicon, oxygen and hydrogen respectively. **(b)** Infrared spectra of EFAL 3 and EFAL 3 plus SiO_2 chain.

As can be seen, the EFAL is interacting with the framework not only through hydrogen bonds, but also through bonds with a more covalent nature, which will change its properties, clearly shown in the differences between the infrared spectra.

4.2.3. NMR spectroscopy results

1D ^{29}Si NMR

The main 1D (one dimensional) ^{29}Si NMR signals one would expect from these types of samples are from $Si(OSi)_4$, typically between -102 to -116 ppm, $Si(OSi)_3(OAl)$, between -107 to -96 ppm, and $Si(OSi)_3OH$, whose peak can be seen (though not always present) at higher chemical shift value than $Si(OSi)_3(OAl)$ peaks, but lower or overlapping with $Si(OSi)_2(OAl)_2$ [25], [26], [43] .

Looking at the spectra and at the literature, the interpretation is not so clear cut, starting with silicalite's spectra shown below.

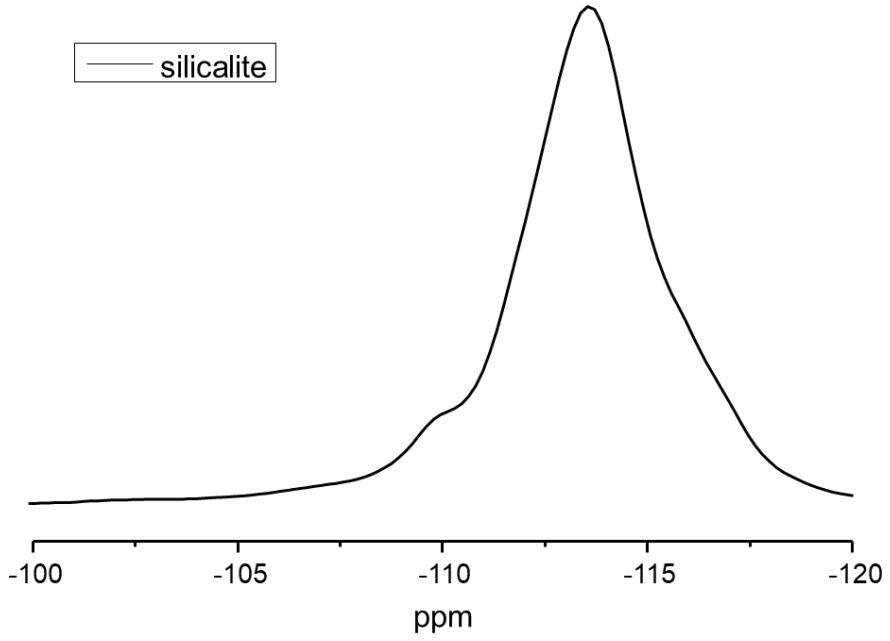

Figure 28. Silicalite's 1D ^{29}Si MAS NMR spectra.

It is expected that only $Si(OSi)_4$ and very few $Si(OSi)_3OH$ silicon are present, but two peaks and a shoulder are present in the typical $Si(OSi)_4$ region, at -116, -113 and -110 ppm. This isn't unexpected, as various inequivalent crystallographic Si sites (still chemically equivalent) have been identified in high resolution ^{29}Si NMR (line widths of 0.06 ppm, 6 Hz) by differentiating peaks in silicalite at room temperature [25], [85]. As such, the three signals arise from $Si(OSi)_4$ groups, with the two less prominent signals (- 110 and -116 ppm) corresponding to the more isolated $Si(OSi)_4$ peaks. This fits with my spectra, presenting a peak width at half height of 6.6 ppm, around 944 times higher than the resolution obtained in the referenced paper, which was achieved by measuring highly crystalline samples and careful optimization of all experimental parameters.

Moving now to the z15-ns spectra, three main peaks are seen at -116 -112 and -106 ppm, as illustrated in **Figure 29**.

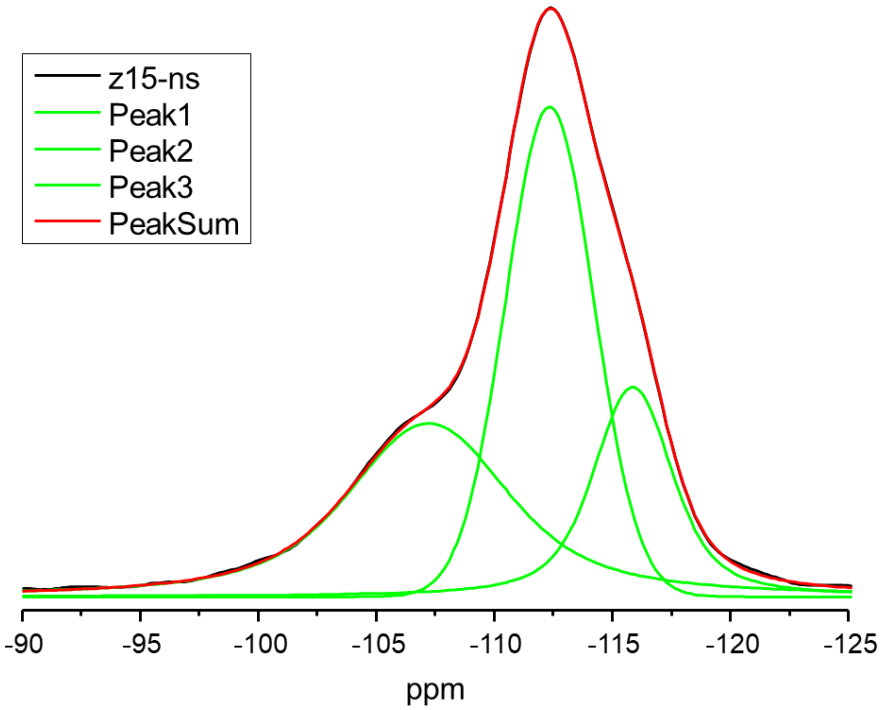

Figure 29. Z15-ns 1D ^{29}Si MAS NMR spectra.

Here the attribution of the -112 and -116 ppm peaks to $Si(OSi)_4$ and the -106 ppm peak to $Si(OSi)_3(OAl)$ is more straightforward. A signal corresponding to $Si(OSi)_3OH$ isn't visible in this spectrum, just like in silicalite, likely due to the high Si/Al ratio of 15 and micrometric crystals, meaning the number of $Si(OSi)_4$ and $Si(OSi)_3(OAl)$ groups is much higher than $Si(OSi)_3OH$. When the crystallites start acquiring nanometric dimensions, the surface area becomes much more relevant, and therefore the ratio of surface silanols to interior Si starts to become appreciable.

Unlike in the vibrational spectra where band intensity couldn't be compared between the different ZSM-5 samples, the $Si(OSi)_4$ signal intensity isn't expected to change, as dealumination only changes the number of $Si(OSi)_{4-n}(OAl)_n$ groups with n>0 (with Al being replaced by OH), as such spectral normalization based on the $Si(OSi)_4$, signal around -112 ppm is an acceptable approach, done in **Figure 30**.

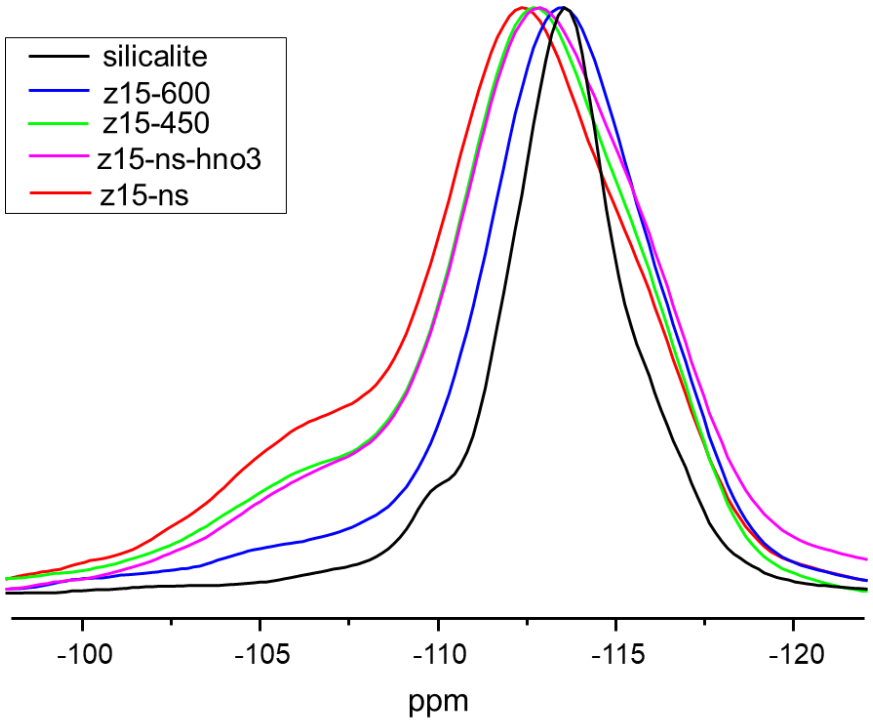

Figure 30. MFI's 1D ^{29}Si MAS NMR spectra after peak normalization.

Although -113 ppm peaks' intensity should be the same, with the possible exception of silicalite, peak position is different between samples, following a clear pattern. The samples with the biggest difference in aluminium content are silicalite (Si/Al=∞) and z15-ns (Si/Al=15), and it is expected that their signals differ the most, with Al introduction breaking the unit cell symmetry present in silicalite and generating more crystallographic and chemically inequivalent sites. Then, as dealumination removes Al from the framework, the samples' signal starts shifting towards silicalite, with dealumination severity coinciding with peak shift, z15-450 ≈ z15-ns-hno3 > z15-600. The higher variety of Si chemical environment in ZSM-5 is also seen in the broader peaks, with peak width decreasing due to increasing chemically and crystallographic equivalent sites as Al content decreases. The trend observed in the -106 ppm peaks is also expected, as its intensity decreases as the Al is expelled from the framework. This also allows to estimate the Si/Al ratio based on the signals peak intensity ((Si/Al)NMR= I4+ I3+ I2+ I1+ I0/(I4+ 0.75 I3+ 0.5 I2+ 0.25 I1)) yielding the following results.

Table 5. ^{29}Si NMR peak intensities and corresponding Si/Al rations.

	Si(OSi$_4$) [-116 ppm]	Si(OSi$_4$) [-113 ppm]	Si((OSi$_3$)(OAl$_1$)) [-106 ppm]	Si/Al
z15-ns	3267410.56	7579942.45	2712284.3	19.99737
z15-450	7741891.05	23094973.2	5834236.97	25.142
z15-ns-hno3	5816247.33	13700415.7	2791094.29	31.96991
z15-600	3344933.08	8812119.62	632484.807	80.88439

As expected, the aluminium content decreases from z15-ns > z15-450 > z15-ns-HNO_3 > z15-600 > silicalite≈0. Z15-ns by this metric presents a higher ratio than the expected value of 15, however, that corresponded to the commercial NH_4ZSM-5 sample, before calcination to convert to proton form, and even with very careful calcination some dealumination will occur, releasing Al from the framework. Further on, when analysing the ^{27}Al NMR spectra this will be confirmed by the presence of EFAl peaks in z15-ns's spectrum. One must be reminded however that these Si/Al ratios must be taken as qualitative values and not a quantitative accurate metric, since general error with instrumentation during quantification, peak fitting, and the fact that the equations is only accurate for samples with Si/Al lower than 10, all contribute to the associated error [25], [26], [36]. Acid leaching with 3 M HNO_3 seems to cause similar dealumination to 450 ºC steaming, both palling in comparison to the extent of the z15-600 sample.

1D ^{1}H NMR

Due to the low concentration of EFAL and bridging hydroxyl groups, samples must be dehydrated, so the H signals from these species can be detected. Spectra from hydrated samples were also obtained, as they provide useful information regarding the interaction of water with these species, in particular when compared with their dehydrated counterparts. The dehydration however was incomplete, visible by the presence of broad peaks, as exemplified by z15-ns's spectra in **Figure 31** [84], [86].

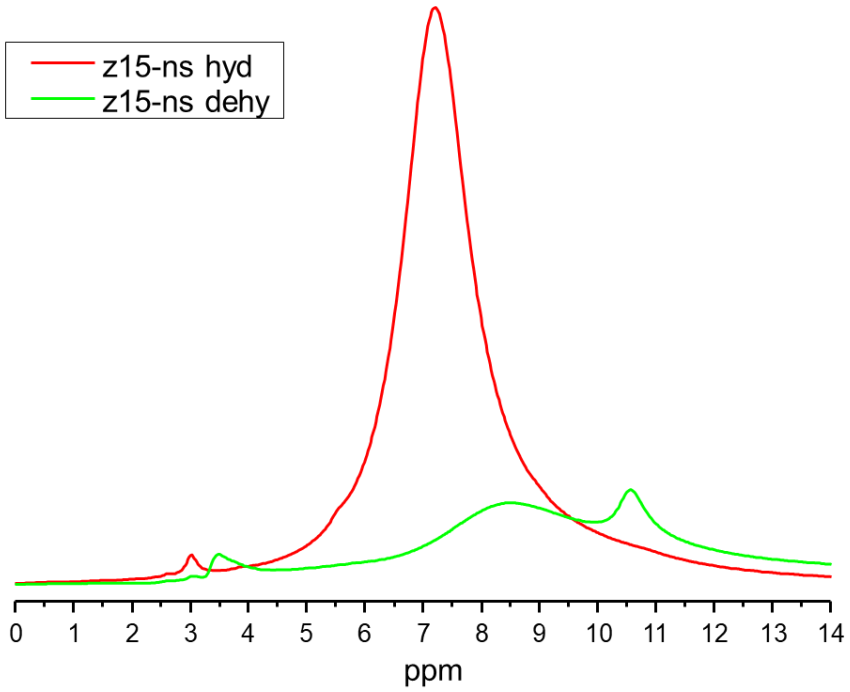

Figure 31. Z15-ns 1D ^{1}H MAS NMR spectra of dehydrated and hydrated samples.

In a study performed by C. Bornes *et al*, a H-ZSM-5 sample with 17 Si/Al was analysed, where ^{1}H NMR spectra and thermogravimetric studies of samples with varying degrees of dehydration were performed [86]. They found that dehydration at 100 ºC only partially removed water from the material, leaving around 1 water molecule for every framework aluminium. Dehydration had to be performed at 300 ºC to fully remove water from the samples. Since my samples were dehydrated at lower temperatures (90 ºC) and are more hydrophilic (Si/Al=15) they will most likely have a higher water content than the 1 water molecule for 1 framework aluminium found in the previous study, causing the broader water peaks. For this reason, dehydration at 300 ºC will be attempted in the future to fully dehydrate the samples.

1D ^{27}Al NMR

Let the focus now turn on the 1D ^{27}Al NMR spectra of the MFI samples (**Figure 32**). Silicalite's spectrum shows very small peaks around 60 ppm most likely due to some Al impurities. Focusing on ZSM-5, all spectra show a peak around 55 ppm from framework tetrahedral Al, with the peak intensity decreasing with dealumination extent, as expected, but it also seems to shift to highfield with steaming at 600 ºC. The peak at 30 ppm corresponds to pentacoordinated EFAL species, which only start to appear with steaming at 450 ºC, with its intensity increasing with dealumination severity, as expected. A peak

around 0 ppm corresponding to octahedral species is present in z15-ns, which isn't unexpected as the sample's preparation involved calcination, which, as careful as it can be done, will always cause some dealumination. With dealumination it becomes much broader, its intensity decreases and at higher temperatures starts to shift to downfield (higher ppm).

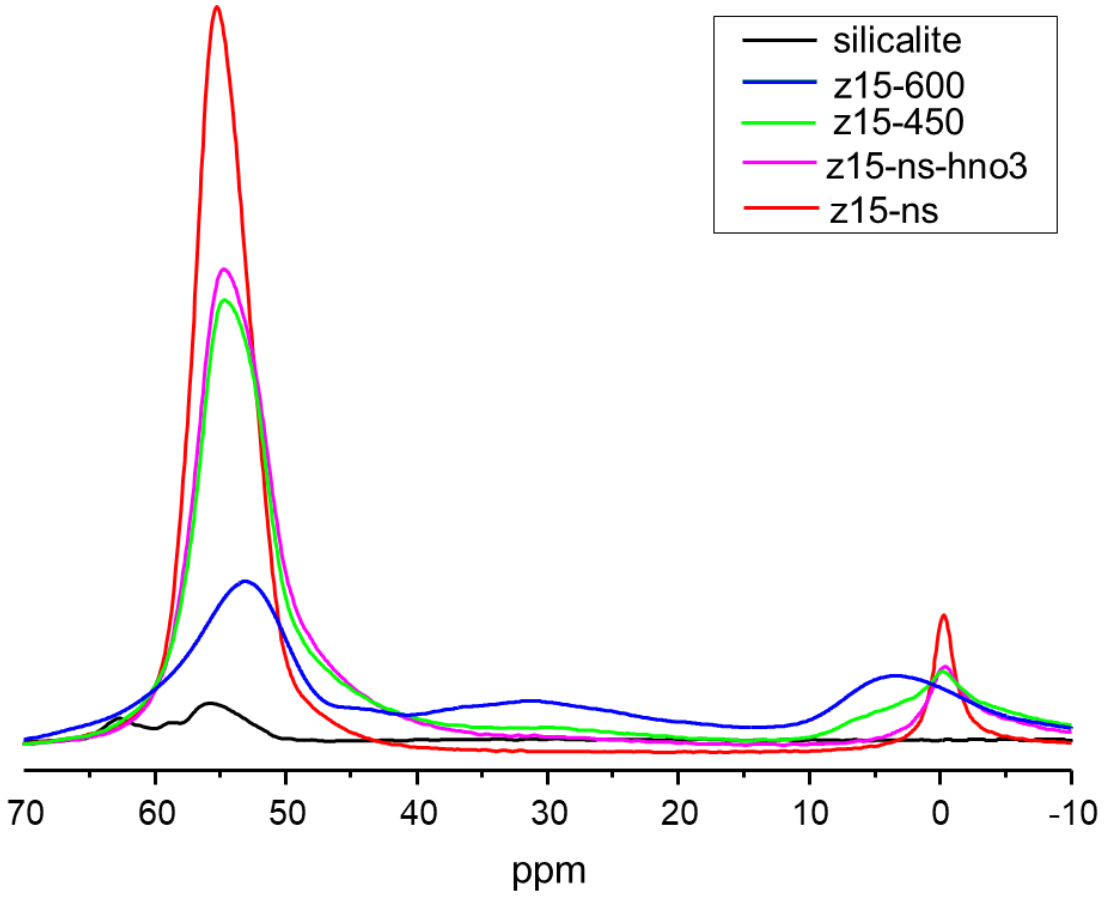

Figure 32. MFI's 1D ^{27}Al MAS NMR spectra.

Although most traditional Al NMR studies of zeolites stop here, various groups have performed studies about zeolite dealumination and EFAL formation utilizing theoretical calculations, as well as solid state NMR with 1D ^{29}Si, ^{1}H and ^{27}Al MAS-NMR; 2D DQ ^{1}H and ^{27}Al MAS-NMR and 2D 3Q ^{27}Al MAS-NMR experiments, mainly focusing on the Y zeolite, but also on modernite and ZSM-5 [81]–[84], [87]. Besides determining the origin of EFAL and Bronsted acid site synergy and EFAL proximities, they also proposed a dealumination mechanism [81], [83]. On mild dealumination conditions, such as calcination, it is expected that octahedral FAAL (framework associated aluminium) and octahedral EFAL are formed [83], [84]. Specifically, the Si-O(H)-Al bond is ruptured, forming $Al(OSi(OT)_3)_3$ (where T is either Al or Si) when the sample is dehydrated, and $Al(OSi(OT)_3)_3(H_2O)_3$ when the sample is hydrated, giving rise to the octahedral signal in ^{27}Al NMR (performed on hydrated

samples). These species can be further hydrolysed, releasing $Al(OH)_3$, which becomes $Al(OH)_3(H_2O)_3$ in hydrated samples. If dealumination occurs at harsher conditions (steaming instead of calcination, higher temperatures, etc) some of these $Al(OH)_3$ interact with the Bronsted acid sites, undergoing hydrolysis, releasing water and originating $Al(OH)_2^+$ EFAL ,which becomes five coordinated in hydrated samples, while also eliminating the acidic proton from acid site. The negative charge in the framework is stabilized by the $Al(OH)_2^+$ EFAL. In H-Y zeolite further hydrolysis steps were identified with the formation of $Al(OH)^{2+}$,tetracoordinated in hydrated samples, but for H-ZSM5 only 5 and 6 coordinated EFAL were identified [84]. No 4 coordinated species were visible in the ^{27}Al MAS, ^{27}Al DQ MAS and ^{27}Al MQ-MAS spectra of calcinated samples at 600 ºC.

These results are very promising and exciting and could offer some explanation to a few of the observed changes between my samples. ^{27}Al triple-quantum MAS NMR spectra of z15-ns and z15-600 were measured, being represented in **Figure 33.**

In the z15-ns spectra only two signals can be identified, one from tetrahedral framework aluminium around (56.0; 56.9) ppm and another from octahedral aluminium around (0.7; 1.3) ppm, most likely due to FAAL species, as dealumination extent in this sample is very low. In the z15-600 sample the signal from octahedral species becomes much broader, acquiring an oval shape, with its centre now being around (6.4; 10.2) ppm. This behaviour and the broadening and shift to downfield seen in the single quantum spectra could be due to the octahedral FAAL converting into octahedral EFAL with increasing dealumination extent, which might have a signal shifted to higher ppm with a higher quadrupolar constant. A new signal also appears near (36.2; 47.1) ppm, arising from pentahedral EFAL species. In the tetrahedral region the (56.1; 58.0) ppm signal is still present but now a new signal is starting to form around (60.3; 69.8) ppm. This behaviour and the 55.3 ppm peak shift to highfield with steaming at 600 ºC ,in the single quantum spectra, could be due to the formation of tetrahedral EFAL species. Although in the performed studies the tetracoordinated EFAL wasn't detected in H-ZSM-5 sample, its most intense dealumination was a calcination at 600ºC and it is possible that more extreme dealumination conditions could form $Al(OH)^{2+}$ [84]. In fact when steaming and calcination are performed at the same temperature, steaming has shown to cause more severe dealumination [87]. As such the decreasing concentration of framework aluminium, and the formation of the tetrahedral EFAL in significant amount in the 600 ºC steamed sample could cause the observed changes in the signals around the 60 ppm region.

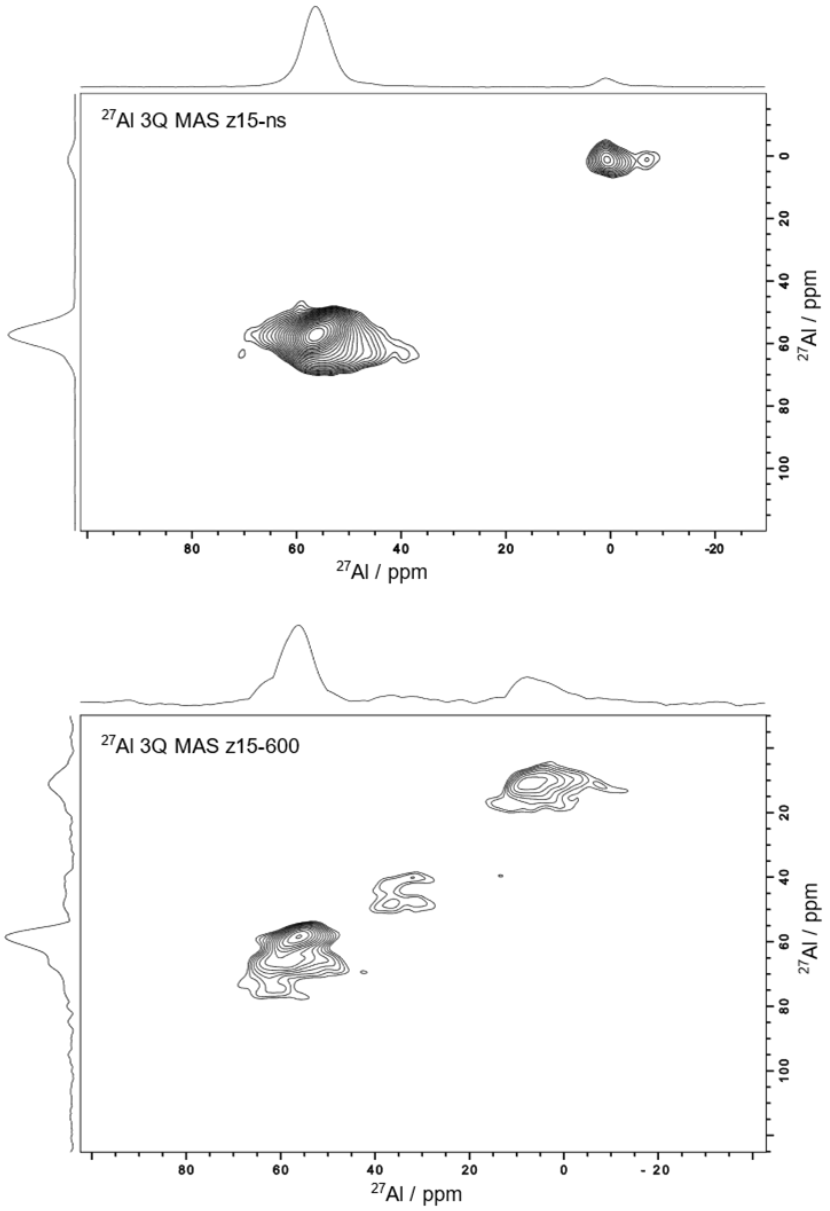

Figure 33. ^{27}Al triple-quantum MAS spectra of z15-ns and z15-600 recorded on hydrated samples at 16.4 T.

To emphasize, although promising these results don't confirm the presence of these specific EFAL species in the studied samples. They are a useful insight, requiring more experimentation, like performing ^{27}Al triple quantum experiments for other samples to have intermediary and more intense dealumination steps (the latter requiring a new sample steamed at higher temperatures), computational simulations of these species interacting with the framework to check if their spectra (NMR and vibrational) match, etc.

5. Conclusions

The synthesis of 2D layered surfactant templated zeolites and their corresponding gemini BSDA was attempted. Although the later batches of SDAs synthesis presented anomalous results and the zeolite synthesis using those compounds failed, zeolites presenting the typical XRD patterns of 2D nanosheets were obtained by utilizing 18-N_3-18 and 18-N_4-18 SDAs from earlier batches. Nitrogen physisorption experiments pointed to these materials' nanosheets being assembled in a unilamellar/disordered structure, but it also pointed to the fact that the resulting samples weren't pure 2D materials. The XRD data alongside pore volume and surface area values obtained from the nitrogen isotherms seem to indicate that the samples, besides the expected 2D layered nanosheet phase, also contain an additional silicate phase. In the case of the sample originated with 18-N_3-18 this phase is amorphous and appeared due to gel boiling and spilling during aging. For the sample originated with 18-N_4-18 the silicalite phase is crystalline, layered and non-porous, most likely arising from added SDA containing a significant amount of a single ammonium group surfactant molecule.

The structure optimization and vibrational spectra simulation of the MFI framework and possible EFAL structures was performed. However, analysis of experimental DRIFT and INS spectra of the various H-ZSM-5 samples with different dealumination extents was not able to detect bands arising from EFAL species. As such, the identification of specific EFAL geometries or features based on the comparison of experimental and theoretical spectra couldn't be performed. The most likely explanation is the low concentration of these species, having their signal drowned by the framework modes, although in the case of the INS spectra, where this was expected to be less problematic, the signal to noise ratio due to the presence of water was quite significant. This hindered not only this specific analysis, but also the study of framework changes by this technique. In the DRIFT spectra on the other hand, a clear pattern could be seen where with increasing dealumination the H-ZSM-5 spectra's bands started to shift closer towards silicalite's due to the increasing Si content. ^{29}Si NMR experiments corroborated that increasing dealumination degree, removed Al from the framework, moving the samples closer to silicalite. ^{1}H NMR was performed on hydrated and dehydrated samples, however as expected, the dehydration at 90 ºC was insufficient to completely remove water from the samples, leading to the observation of broad water peaks in both spectra. ^{27}Al NMR showed that with increasing dealumination, octahedral and pentacoordinated EFAL species are formed with the removal of aluminium from the framework. 2D triple quantum ^{27}Al MAS spectra seem to corroborate literature findings, where octahedral FAAL and tetracoordinated aluminium form alongside the aforementioned

species during the dealumination process following the order: framework aluminium, octahedral FAAL, octahedral EFAL, pentacoordinated EFAL and tetracoordinated EFAL (in hydrated species). These are not conclusive results, but encouraging points that warrant further investigation.

6. Future work

The study of 2D layered zeolites is still in its early stages, with much left to do. One of the more urgent topics to address is the high yield anomaly in the batches **iv** through **vi** of SDA synthesis. Since the SDA was not properly synthetized, there is no point in continuing with the zeolite synthesis and characterization. Thorough replications of the first steps should be made, and the resulting products analysed (by NMR, thin layer chromatography, etc) to determine the resulting structure and detect possible side products, contaminants, or competitive reactions.

Once the SDA issues are solved, the next step will be the synthesis of zeolite 18-N_5-18 and repetitions for 18-N_3-18 and 18-N_4-18 without the previously mentioned problems. These materials can then be characterized, by XRD and nitrogen physisorption, as well as inductive coupled plasma mass spectroscopy (ICP-MS) for chemical composition determination, in situ Fourier transform infrared spectroscopy (FTIR) to study acidic properties, and scanning and transmission electron microscopy (SEM and TEM respectively) for crystal morphology analysis, allowing to confirm the presence of the nanosheets and assessing how they assemble.

Another interesting topic to pursue is how the reaction conditions influence the resulting nanosheet assembly, as there isn't still a clear pattern. For example, although this reaction followed a protocol for hexagonal assembly of nanosheets, the nitrogen physisorption seems to indicate that a unilamellar structure was obtained.

Regarding the INS and ^{1}H NMR spectra of H-ZSM-5 zeolites, the incomplete dehydration hindered both studies. As such, repeat analysis with a more robust dehydration protocol of the samples would be helpful. In the case of INS, this would assist in determining whether this approach enables the detection and identification of the structure of EFAL species. For ^{1}H NMR, the study of the evolution of proton signals from zeolite's silanol groups, Bronsted acid sites and EFALs' silanols with increasing dealumination will give useful insights into the various species and their structures .

Regarding the simulations of possible EFAL structures, in the future the inclusion of a small segment of the zeolitic framework will much more accurately describe and predict these structures, seeming like the path forward taken by most researchers. Besides its

possible application with INS, the simulation of 1D and 2D NMR spectra also seems like a powerful tool to gain a better insight into the nature of these species.

Finally, 2D NMR experiments seem to be a promising tool to unravel the nature of EFAL species as well as their sitting and proximities in the framework. ^{27}Al 3Q MAS experiments, in particular should be performed on the remaining samples and on H-ZSM-5 samples steamed at even higher temperatures, to have further insight into the aluminium species formed at intermediary dealumination conditions as well as at more extreme ones respectively. ^{1}H DQ MAS and ^{27}Al DQ MAS should also be performed to analyse the proximities of EFAL species, Bronsted acid sites and framework silanols between each other and themselves.

7. Bibliography

[1] A. F. Masters and T. Maschmeyer, “Zeolites – From curiosity to cornerstone,” *Microporous Mesoporous Mater.*, vol. 142, no. 2–3, pp. 423–438, Jul. 2011, doi: 10.1016/j.micromeso.2010.12.026.

[2] Grand View Research, “Zeolite Market Size, Share & Trends Analysis Report By Application (Catalyst, Adsorbent, Detergent Builder), By Product (Natural, Synthetic), By Region (North America, Europe, APAC, CSA, MEA), And Segment Forecasts, 2022 - 2030.” https://www.grandviewresearch.com/industry-analysis/zeolites-market (accessed Sep. 26, 2023).

[3] A. A. Vasconcelos *et al.*, “Zeolites: A Theoretical and Practical Approach with Uses in (Bio)Chemical Processes,” *Appl. Sci.*, vol. 13, no. 3, p. 1897, Feb. 2023, doi: 10.3390/app13031897.

[4] H. A. Alalwan, A. H. Alminshid, and H. A. S. Aljaafari, “Promising evolution of biofuel generations. Subject review,” *Renew. Energy Focus*, vol. 28, no. 00, pp. 127–139, Mar. 2019, doi: 10.1016/j.ref.2018.12.006.

[5] C. M. P. Bornes, “NMR study of zeolites’ acid sites using molecular probes,” Universidade de Aveiro, 2023.

[6] E. G. Derouane *et al.*, “The Acidity of Zeolites: Concepts, Measurements and Relation to Catalysis: A Review on Experimental and Theoretical Methods for the Study of Zeolite Acidity,” *Catal. Rev.*, vol. 55, no. 4, pp. 454–515, Oct. 2013, doi: 10.1080/01614940.2013.822266.

[7] N. R. Simpson, “Cages to trap metals.” https://chembam.com/online-resources/gcse-resources/cages/ (accessed Sep. 27, 2023).

[8] X. Tang *et al.*, “Violation or Abidance of Löwenstein’s Rule in Zeolites Under Synthesis Conditions?,” *ACS Catal.*, vol. 9, no. 12, pp. 10618–10625, Dec. 2019, doi: 10.1021/acscatal.9b01844.

[9] M. Ravi, V. L. Sushkevich, and J. A. van Bokhoven, “Towards a better understanding of Lewis acidic aluminium in zeolites,” *Nat. Mater.*, vol. 19, no. 10, pp. 1047–1056, Oct. 2020, doi: 10.1038/s41563-020-0751-3.

[10] M. Rybicki and J. Sauer, “Acid strength of zeolitic Brønsted sites—Dependence on dielectric properties,” *Catal. Today*, vol. 323, pp. 86–93, Feb. 2019, doi:

10.1016/j.cattod.2018.04.031.

[11] H. Windeck, F. Berger, and J. Sauer, “Spectroscopic Signatures of Internal Hydrogen Bonds of Brønsted-Acid Sites in the Zeolite H-MFI,” *Angew. Chemie Int. Ed.*, vol. 62, no. 25, Jun. 2023, doi: 10.1002/anie.202303204.

[12] S. Bordiga, C. Lamberti, F. Bonino, A. Travert, and F. Thibault-Starzyk, “Probing zeolites by vibrational spectroscopies,” *Chem. Soc. Rev.*, vol. 44, no. 20, pp. 7262–7341, 2015, doi: 10.1039/C5CS00396B.

[13] C. Bornes, “Study of zeolites acidic properties using solid-state NMR,” Universidade de Aveiro, 2017.

[14] W. Chen *et al.*, “Acidity characterization of H-ZSM-5 catalysts modified by pre-coking and silylation,” vol. 154, 2004, pp. 2269–2274.

[15] M. Shamzhy, B. Gil, M. Opanasenko, W. J. Roth, and J. Čejka, “MWW and MFI Frameworks as Model Layered Zeolites: Structures, Transformations, Properties, and Activity,” *ACS Catal.*, vol. 11, no. 4, pp. 2366–2396, Feb. 2021, doi: 10.1021/acscatal.0c05332.

[16] J. Přech, P. Pizarro, D. P. Serrano, and J. Čejka, “From 3D to 2D zeolite catalytic materials,” *Chem. Soc. Rev.*, vol. 47, no. 22, pp. 8263–8306, 2018, doi: 10.1039/C8CS00370J.

[17] E. Schulman, W. Wu, and D. Liu, “Two-Dimensional Zeolite Materials: Structural and Acidity Properties,” *Materials (Basel).*, vol. 13, no. 8, p. 1822, Apr. 2020, doi: 10.3390/ma13081822.

[18] M. Choi, K. Na, J. Kim, Y. Sakamoto, O. Terasaki, and R. Ryoo, “Stable single-unit-cell nanosheets of zeolite MFI as active and long-lived catalysts,” *Nature*, vol. 461, no. 7261, pp. 246–249, Sep. 2009, doi: 10.1038/nature08288.

[19] K. Na *et al.*, “Directing Zeolite Structures into Hierarchically Nanoporous Architectures,” *Science (80-.).*, vol. 333, no. 6040, pp. 328–332, Jul. 2011, doi: 10.1126/science.1204452.

[20] W. Park *et al.*, “Hierarchically Structure-Directing Effect of Multi-Ammonium Surfactants for the Generation of MFI Zeolite Nanosheets,” *Chem. Mater.*, vol. 23, no. 23, pp. 5131–5137, Dec. 2011, doi: 10.1021/cm201709q.

[21] J.-C. Kim, R. Ryoo, M. V. Opanasenko, M. V. Shamzhy, and J. Čejka, “Mesoporous

MFI Zeolite Nanosponge as a High-Performance Catalyst in the Pechmann Condensation Reaction," *ACS Catal.*, vol. 5, no. 4, pp. 2596–2604, Apr. 2015, doi: 10.1021/cs502021a.

[22] K. Na, W. Park, Y. Seo, and R. Ryoo, "Disordered Assembly of MFI Zeolite Nanosheets with a Large Volume of Intersheet Mesopores," *Chem. Mater.*, vol. 23, no. 5, pp. 1273–1279, Mar. 2011, doi: 10.1021/cm103245m.

[23] J. Jung, C. Jo, K. Cho, and R. Ryoo, "Zeolite nanosheet of a single-pore thickness generated by a zeolite-structure-directing surfactant," *J. Mater. Chem.*, vol. 22, no. 11, pp. 4637–4640, 2012, doi: 10.1039/c2jm16539b.

[24] G. Rosa, "Study of the acidity of heterogeneous catalysts (zeolites) through vibrational and NMR spectroscopies using probe molecules." .

[25] A. G. Stepanov, "Basics of Solid-State NMR for Application in Zeolite Science," in *Zeolites and Zeolite-Like Materials*, Elsevier, 2016, pp. 137–188.

[26] K. J. D. MacKenzie and M. E. Smith, *Multinuclear Solid-State NMR of Inorganic Materials*, vol. 6. 2002.

[27] M. Lee and W. I. Goldburg, "Nuclear-Magnetic-Resonance Line Narrowing by a Rotating rf Field," *Phys. Rev.*, vol. 140, no. 4A, pp. A1261–A1271, Nov. 1965, doi: 10.1103/PhysRev.140.A1261.

[28] D. D. Laws, H.-M. L. Bitter, and A. Jerschow, "Solid-state NMR spectroscopic methods in chemistry.," *Angew. Chem. Int. Ed. Engl.*, vol. 41, no. 17, pp. 3096–129, Sep. 2002, doi: 10.1002/1521-3773(20020902)41:17<3096::AID-ANIE3096>3.0.CO;2-X.

[29] Y. Peleg, R. Pnini, E. Zaarur, and L. Johnson, *Schaum's Easy Outlines: Quantum Mechanics*. McGraw-Hill Education, 2006.

[30] J. Keeler, *Understanding NMR spectroscopy*. Wiley, 2006.

[31] P. Rinck, "Magnetic ressonance contrast agents," in *Magnetic Resonance in Medicine*, 14th ed., 2024.

[32] T. Polenova, R. Gupta, and A. Goldbourt, "Magic Angle Spinning NMR Spectroscopy: A Versatile Technique for Structural and Dynamic Analysis of Solid-Phase Systems," *Anal. Chem.*, vol. 87, no. 11, pp. 5458–5469, Jun. 2015, doi: 10.1021/ac504288u.

[33] T. Ukmar, V. Kaučič, and G. Mali, “Solid-state NMR spectroscopy and first-principles calculations: A powerful combination of tools for the investigation of polymorphism of indomethacin,” *Acta Chim. Slov.*, vol. 58, no. 3, pp. 425–433, 2011.

[34] A. E. Bennett, C. M. Rienstra, M. Auger, K. V. Lakshmi, and R. G. Griffin, “Heteronuclear decoupling in rotating solids,” *J. Chem. Phys.*, vol. 103, no. 16, pp. 6951–6958, Oct. 1995, doi: 10.1063/1.470372.

[35] J. S. Waugh, L. M. Huber, and U. Haeberlen, “Approach to High-Resolution nmr in Solids,” *Phys. Rev. Lett.*, vol. 20, no. 5, pp. 180–182, Jan. 1968, doi: 10.1103/PhysRevLett.20.180.

[36] L. Mafra and J. Klinowski, “Molecular Sieves: Crystalline Systems,” in *eMagRes*, vol. 2, no. 1, Chichester, UK: John Wiley & Sons, Ltd, 1996, pp. 89–108.

[37] Y. Jiang, J. Huang, W. Dai, and M. Hunger, “Solid-state nuclear magnetic resonance investigations of the nature, property, and activity of acid sites on solid catalysts,” *Solid State Nucl. Magn. Reson.*, vol. 39, no. 3–4, pp. 116–141, May 2011, doi: 10.1016/j.ssnmr.2011.03.007.

[38] L. E. Sandoval-Díaz, J. A. González-Amaya, and C. A. Trujillo, “General aspects of zeolite acidity characterization,” *Microporous Mesoporous Mater.*, vol. 215, pp. 229–243, 2015, doi: 10.1016/j.micromeso.2015.04.038.

[39] R. Banks, G. Sinha, and C. Chu, “Introduction to Vibrations.” https://chem.libretexts.org/Bookshelves/Physical_and_Theoretical_Chemistry_Textbook_Maps/Supplemental_Modules_(Physical_and_Theoretical_Chemistry)/Spectroscopy/Vibrational_Spectroscopy/Vibrational_Modes/Introduction_to_Vibrations (accessed Dec. 04, 2023).

[40] P. Ribeiro Claro, “Espectroscopia Vibracional,” *Rev. Ciência Elem.*, vol. 6, no. 2, pp. 1–5, 2018, doi: 10.24927/rce2018.040.

[41] P. Ribeiro Claro, “Espectroscopia,” *Rev. Ciência Elem.*, vol. 5, no. 4, pp. 1–4, Dec. 2017, doi: 10.24927/rce2017.052.

[42] S. M. Campbell, D. M. Bibby, J. M. Coddington, R. F. Howe, and R. H. Meinhold, “Dealumination of HZSM-5 Zeolites,” *J. Catal.*, vol. 161, no. 1, pp. 338–349, Jun. 1996, doi: 10.1006/jcat.1996.0191.

[43] A. Zachariou *et al.*, “Counting the Acid Sites in a Commercial ZSM-5 Zeolite Catalyst,” *ACS Phys. Chem. Au*, vol. 3, no. 1, pp. 74–83, 2023, doi: 10.1021/acsphyschemau.2c00040.

[44] S. F. Parker, A. J. Ramirez-Cuesta, and L. Daemen, “Vibrational spectroscopy with neutrons: Recent developments,” *Spectrochim. Acta - Part A Mol. Biomol. Spectrosc.*, vol. 190, pp. 518–523, 2018, doi: 10.1016/j.saa.2017.09.057.

[45] P. Vaz, “Espectroscopia de Difusão Inelástica de Neutrões,” *Rev. Ciência Elem.*, vol. 7, no. 1, pp. 1–5, 2019, doi: 10.24927/rce2019.009.

[46] NIST Center for Neutron Research, “Neutron scattering lengths and cross sections.” https://www.ncnr.nist.gov/resources/n-lengths/ (accessed Dec. 05, 2023).

[47] H. Jobic, A. Tuel, M. Krossner, and J. Sauer, “Water in Interaction with Acid Sites in H-ZSM-5 Zeolite Does Not Form Hydroxonium Ions. A Comparison between Neutron Scattering Results and ab Initio Calculations,” *J. Phys. Chem.*, vol. 100, no. 50, pp. 19545–19550, Jan. 1996, doi: 10.1021/jp9619954.

[48] D. H. Brouwer, I. L. Moudrakovski, R. J. Darton, and R. E. Morris, “Comparing quantum-chemical calculation methods for structural investigation of zeolite crystal structures by solid-state NMR spectroscopy,” *Magn. Reson. Chem.*, vol. 48, no. S1, pp. S113–S121, Dec. 2010, doi: 10.1002/mrc.2642.

[49] O. Lisboa, M. Sánchez, and F. Ruette, “Modeling extra framework aluminum (EFAL) formation in the zeolite ZSM-5 using parametric quantum and DFT methods,” *J. Mol. Catal. A Chem.*, vol. 294, no. 1–2, pp. 93–101, Oct. 2008, doi: 10.1016/j.molcata.2008.08.003.

[50] “Modern Computational Organic Chemistry.” 2014, [Online]. Available: https://baranlab.org/seminars/.

[51] F. Jensen, *Introduction to Computational Chemistry*. Wiley, 2007.

[52] A. Tomberg, “GAUSSIAN 09W TUTORIAL AN INTRODUCTION TO COMPUTATIONAL CHEMISTRY USING G09W AND AVOGADRO SOFTWARE.” pp. 1–34, 2013.

[53] J. Rouquerol, F. Rouquerol, and K. Sing, *Adsorption by Powders and Porous Solids: Principles, Methodology and Applications*. Elsevier Science, 1998.

[54] S. Lowell, J. E. Shields, M. A. Thomas, and M. Thommes, *Characterization of*

Porous Solids and Powders: Surface Area, Pore Size and Density, vol. 16. Dordrecht: Springer Netherlands, 2004.

[55] B. LIPPENS, “Studies on pore systems in catalysts V. The t method,” *J. Catal.*, vol. 4, no. 3, pp. 319–323, Jun. 1965, doi: 10.1016/0021-9517(65)90307-6.

[56] Paulo Ribeiro-Claro; Carlos Bornes; Marina Ilkaeva; JIMENEZ RUIZ Monica; MAFRA Luis; Mariela Nolasco; RODRIGUES Leonor and Pedro D. Vaz., “Unraveling the structure of Brønsted/Lewis acid sites using probe molecules and smart control of HZSM-5 zeolite (extra)framework composition,” 2021. doi: 10.5291/ILL-DATA.DIR-170.

[57] P. Ribeiro-Claro; *et al.*, “Unraveling the structure of Brønsted/Lewis acid sites using smart control of HZSM-5 zeolite EFAL composition (Continuation),” Institut Laue-Langevin (ILL), 2023. doi: 10.5291/ILL-DATA.DIR-290.

[58] “STFC Scientific Computing Department’s SCARF cluster.” .

[59] S. J. Clark *et al.*, “First principles methods using CASTEP,” *Zeitschrift für Krist. - Cryst. Mater.*, vol. 220, no. 5–6, pp. 567–570, May 2005, doi: 10.1524/zkri.220.5.567.65075.

[60] K. Refson, P. R. Tulip, and S. J. Clark, “Variational density-functional perturbation theory for dielectrics and lattice dynamics,” *Phys. Rev. B*, vol. 73, no. 15, p. 155114, Apr. 2006, doi: 10.1103/PhysRevB.73.155114.

[61] J. P. Perdew, K. Burke, and M. Ernzerhof, “Generalized Gradient Approximation Made Simple,” *Phys. Rev. Lett.*, vol. 77, no. 18, pp. 3865–3868, Oct. 1996, doi: 10.1103/PhysRevLett.77.3865.

[62] K. Dymkowski, S. F. Parker, F. Fernandez-Alonso, and S. Mukhopadhyay, “AbINS: The modern software for INS interpretation,” *Phys. B Condens. Matter*, vol. 551, pp. 443–448, Dec. 2018, doi: 10.1016/j.physb.2018.02.034.

[63] O. Arnold *et al.*, “Mantid—Data analysis and visualization package for neutron scattering and mu SR experiments,” *Nucl. Instruments Methods Phys. Res. Sect. A Accel. Spectrometers, Detect. Assoc. Equip.*, vol. 764, pp. 156–166, Nov. 2014, doi: 10.1016/j.nima.2014.07.029.

[64] X. Pu, N. Liu, and L. Shi, “Acid properties and catalysis of USY zeolite with different extra-framework aluminum concentration,” *Microporous Mesoporous Mater.*, vol.

201, pp. 17–23, Jan. 2015, doi: 10.1016/j.micromeso.2014.08.056.

[65] R. D. Shannon, K. H. Gardner, R. H. Staley, G. Bergeret, P. Gallezot, and A. Auroux, “The nature of the nonframework aluminum species formed during the dehydroxylation of H-Y,” *J. Phys. Chem.*, vol. 89, no. 22, pp. 4778–4788, Oct. 1985, doi: 10.1021/j100268a025.

[66] and D. J. F. M. J. Frisch, G. W. Trucks, H. B. Schlegel, G. E. Scuseria, M. A. Robb, J. R. Cheeseman, G. Scalmani, V. Barone, G. A. Petersson, H. Nakatsuji, X. Li, M. Caricato, A. V. Marenich, J. Bloino, B. G. Janesko, R. Gomperts, B. Mennucci, H. P. Hratchian, J. V., “Gaussian 16.” Gaussian, Inc., Wallingford CT, 2016.

[67] I. M. Alecu, J. Zheng, Y. Zhao, and D. G. Truhlar, “Computational Thermochemistry: Scale Factor Databases and Scale Factors for Vibrational Frequencies Obtained from Electronic Model Chemistries,” *J. Chem. Theory Comput.*, vol. 6, no. 9, pp. 2872–2887, Sep. 2010, doi: 10.1021/ct100326h.

[68] C. Lee, W. Yang, and R. G. Parr, “Development of the Colle-Salvetti correlation-energy formula into a functional of the electron density,” *Phys. Rev. B*, vol. 37, no. 2, pp. 785–789, Jan. 1988, doi: 10.1103/PhysRevB.37.785.

[69] National Institute of Standards and Technology, “Precomputed vibrational scaling factors,” 2022. https://cccbdb.nist.gov/vibscalejust.asp (accessed Jun. 06, 2022).

[70] K. Murakami, S. Fujioka, K. Mitani, M. Yamashita, and M. Taguchi, *Collection of Simulated XRD Powder Patterns for Zeolites*, vol. 4, no. 9. Elsevier, 2007.

[71] M. Thommes *et al.*, “Physisorption of gases, with special reference to the evaluation of surface area and pore size distribution (IUPAC Technical Report),” *Pure Appl. Chem.*, vol. 87, no. 9–10, pp. 1051–1069, Oct. 2015, doi: 10.1515/pac-2014-1117.

[72] R. Sabarish and G. Unnikrishnan, “A novel anionic surfactant as template for the development of hierarchical ZSM-5 zeolite and its catalytic performance,” *J. Porous Mater.*, vol. 27, no. 3, pp. 691–700, Jun. 2020, doi: 10.1007/s10934-019-00852-5.

[73] A. Orsikowsky-Sanchez, F. Plantier, and C. Miqueu, “Coupled gravimetric, manometric and calorimetric study of CO2, N2 and CH4 adsorption on zeolites for the assessment of classical equilibrium models,” *Adsorption*, vol. 26, no. 7, pp. 1137–1152, Oct. 2020, doi: 10.1007/s10450-020-00206-7.

[74] Z. Bao *et al.*, “Adsorption Equilibria of CO 2 , CH 4 , N 2 , O 2 , and Ar on High Silica Zeolites,” *J. Chem. Eng. Data*, vol. 56, no. 11, pp. 4017–4023, Nov. 2011, doi: 10.1021/je200394p.

[75] O. Šolcová, L. Matějová, P. Topka, Z. Musilová, and P. Schneider, “Comparison of textural information from argon(87 K) and nitrogen(77 K) physisorption,” *J. Porous Mater.*, vol. 18, no. 5, pp. 557–565, Oct. 2011, doi: 10.1007/s10934-010-9409-x.

[76] Q. Huo, D. I. Margolese, and G. D. Stucky, “Surfactant Control of Phases in the Synthesis of Mesoporous Silica-Based Materials,” *Chem. Mater.*, vol. 8, no. 5, pp. 1147–1160, Jan. 1996, doi: 10.1021/cm960137h.

[77] H. van Koningsveld, “High-temperature (350 K) orthorhombic framework structure of zeolite H-ZSM-5,” *Acta Crystallogr. Sect. B Struct. Sci.*, vol. 46, no. 6, pp. 731–735, Dec. 1990, doi: 10.1107/S0108768190007522.

[78] P. F. Corregidor, D. E. Acosta, and H. A. Destéfanis, “Green Synthesis of ZSM-5 Zeolite Prepared by Hydrothermal Treatment of Perlite. Effect of Chemical Composition and Characterization of the Product,” *Sci. Adv. Mater.*, vol. 6, no. 6, pp. 1203–1214, Jun. 2014, doi: 10.1166/sam.2014.1894.

[79] D. Scarano *et al.*, “Fourier-transform infrared and Raman spectra of pure and Al-, B-, Ti- and Fe-substituted silicalites: stretching-mode region,” *J. Chem. Soc. Faraday Trans.*, vol. 89, no. 22, p. 4123, 1993, doi: 10.1039/ft9938904123.

[80] R. F. Howe, P. A. Wright, I. Tuxworth, M. D. Frogley, and G. Cinque, “Synchrotron Infrared Micro-spectroscopy of Zeolite Catalysts,” *Johnson Matthey Technol. Rev.*, 2024, doi: 10.1595/205651324X17048925195038.

[81] S. Li *et al.*, “Brønsted/Lewis Acid Synergy in Dealuminated HY Zeolite: A Combined Solid-State NMR and Theoretical Calculation Study,” *J. Am. Chem. Soc.*, vol. 129, no. 36, pp. 11161–11171, Sep. 2007, doi: 10.1021/ja072767y.

[82] D. L. Bhering, A. Ramírez-Solís, and C. J. A. Mota, “A Density Functional Theory Based Approach to Extraframework Aluminum Species in Zeolites,” *J. Phys. Chem. B*, vol. 107, no. 18, pp. 4342–4347, May 2003, doi: 10.1021/jp022331z.

[83] Z. Yu *et al.*, “Insights into the Dealumination of Zeolite HY Revealed by Sensitivity-Enhanced 27 Al DQ-MAS NMR Spectroscopy at High Field,” *Angew. Chemie Int. Ed.*, vol. 49, no. 46, pp. 8657–8661, Nov. 2010, doi: 10.1002/anie.201004007.

[84] Z. Yu *et al.*, “Brønsted/Lewis Acid Synergy in H–ZSM-5 and H–MOR Zeolites Studied by 1 H and 27 Al DQ-MAS Solid-State NMR Spectroscopy,” *J. Phys. Chem. C*, vol. 115, no. 45, pp. 22320–22327, Nov. 2011, doi: 10.1021/jp203923z.

[85] C. A. Fyfe, H. Strobl, G. T. Kokotailo, G. J. Kennedy, and G. E. Barlow, “Ultrahigh-resolution silicon-29 solid-state MAS NMR investigation of sorbate and temperature-induced changes in the lattice structure of zeolite ZSM-5,” *J. Am. Chem. Soc.*, vol. 110, no. 11, pp. 3373–3380, May 1988, doi: 10.1021/ja00219a005.

[86] C. Bornes *et al.*, “Quantification of Brønsted Acid Sites in Zeolites by Water Desorption Thermogravimetry,” *Eur. J. Inorg. Chem.*, vol. 2020, no. 19, pp. 1860–1866, May 2020, doi: 10.1002/ejic.202000050.

[87] S. Li *et al.*, “Probing the Spatial Proximities among Acid Sites in Dealuminated H-Y Zeolite by Solid-State NMR Spectroscopy,” *J. Phys. Chem. C*, vol. 112, no. 37, pp. 14486–14494, Sep. 2008, doi: 10.1021/jp803494n.

Appendix

Appendix A: Gemini bifunctional structure directing agents' reaction schemes

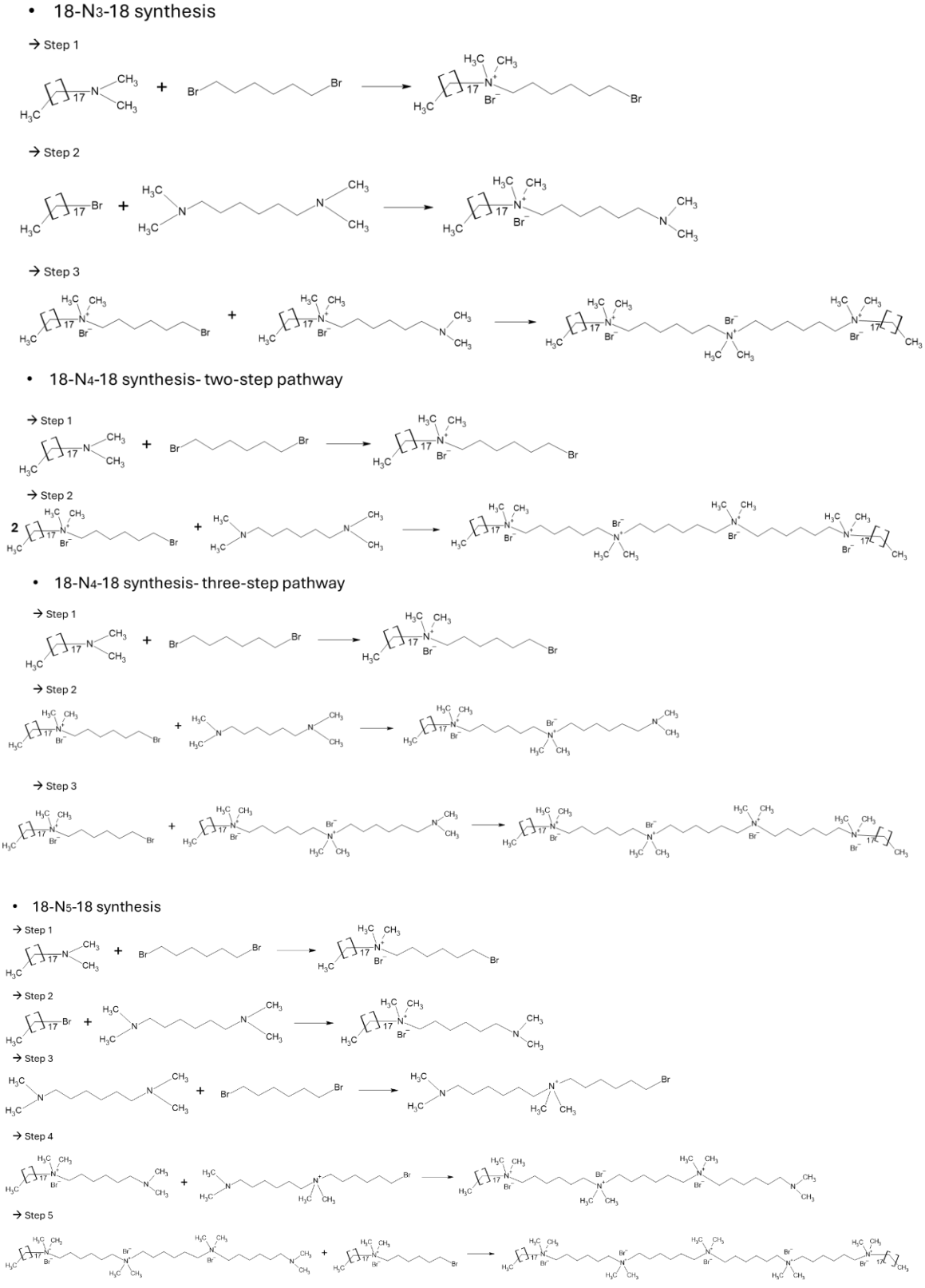

Figure s1. Gemini bifunctional structure directing agents' reaction schemes.

Appendix B: ^{1}H NMR spectra of 18-N-Br and 18-N-N from batches i and ii and 18-N_3-18 from batch i

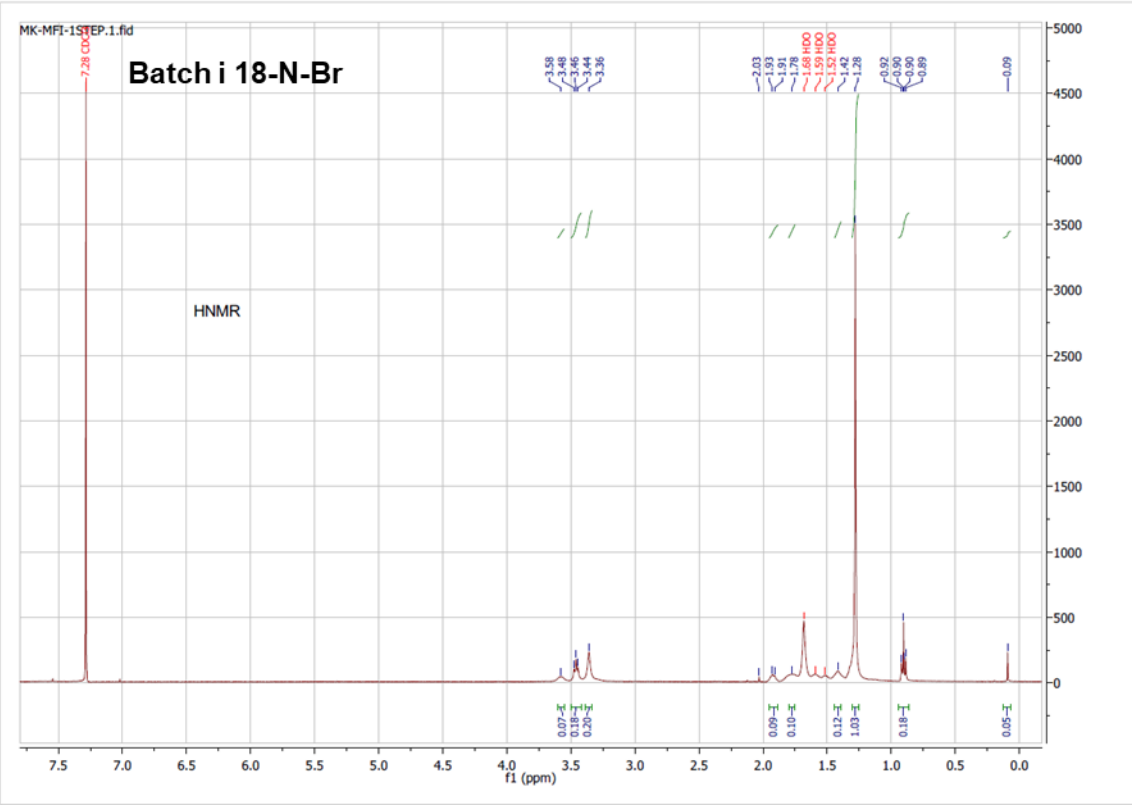

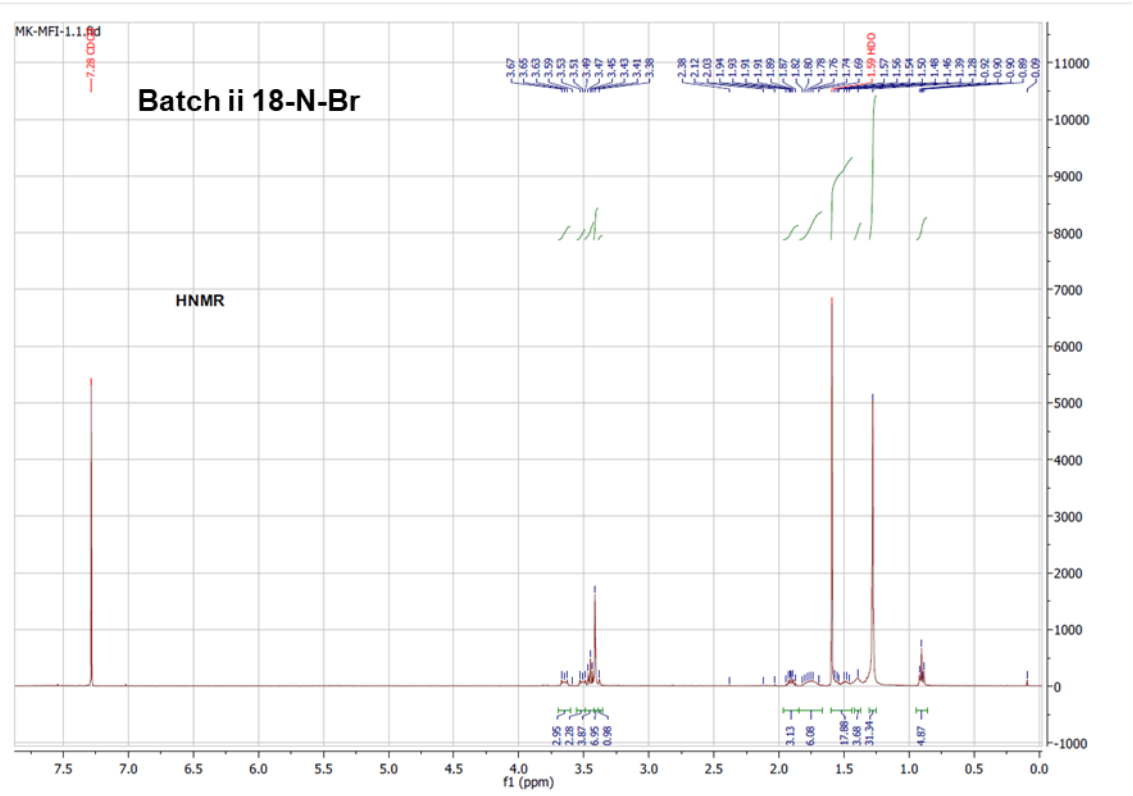

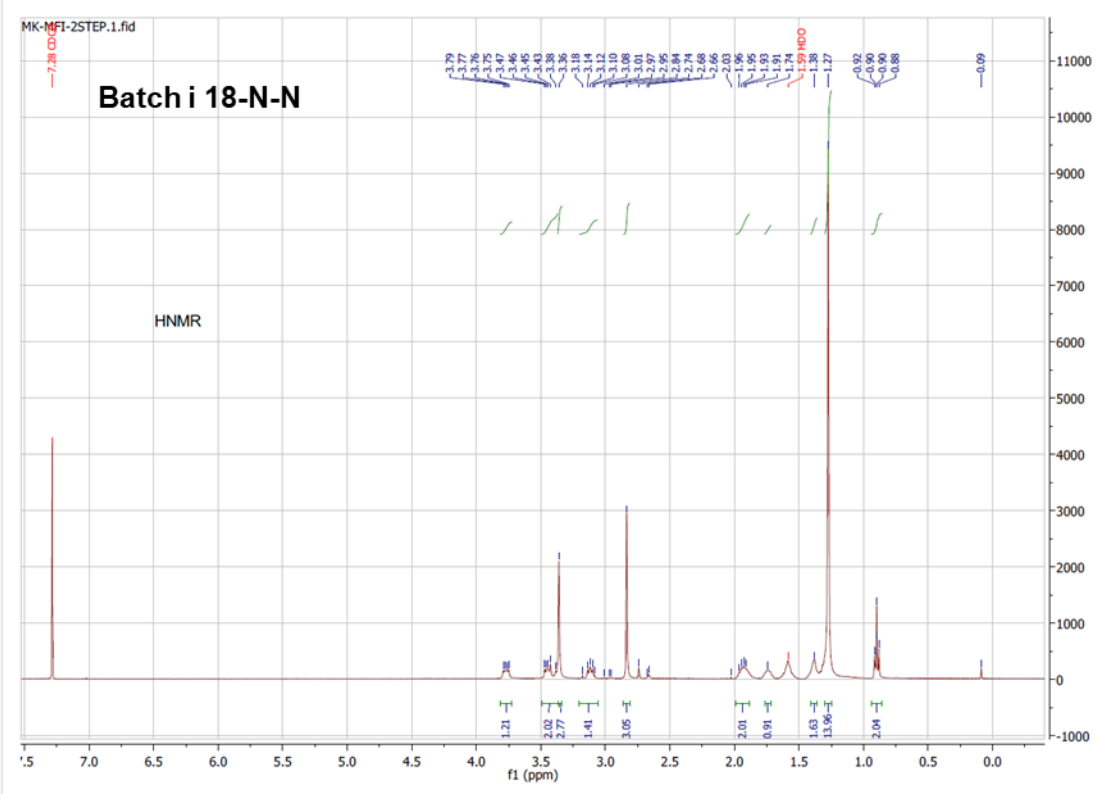
MK-MFI-2STEP.1.fid
Batch i 18-N-N
HNMR
f1 (ppm)

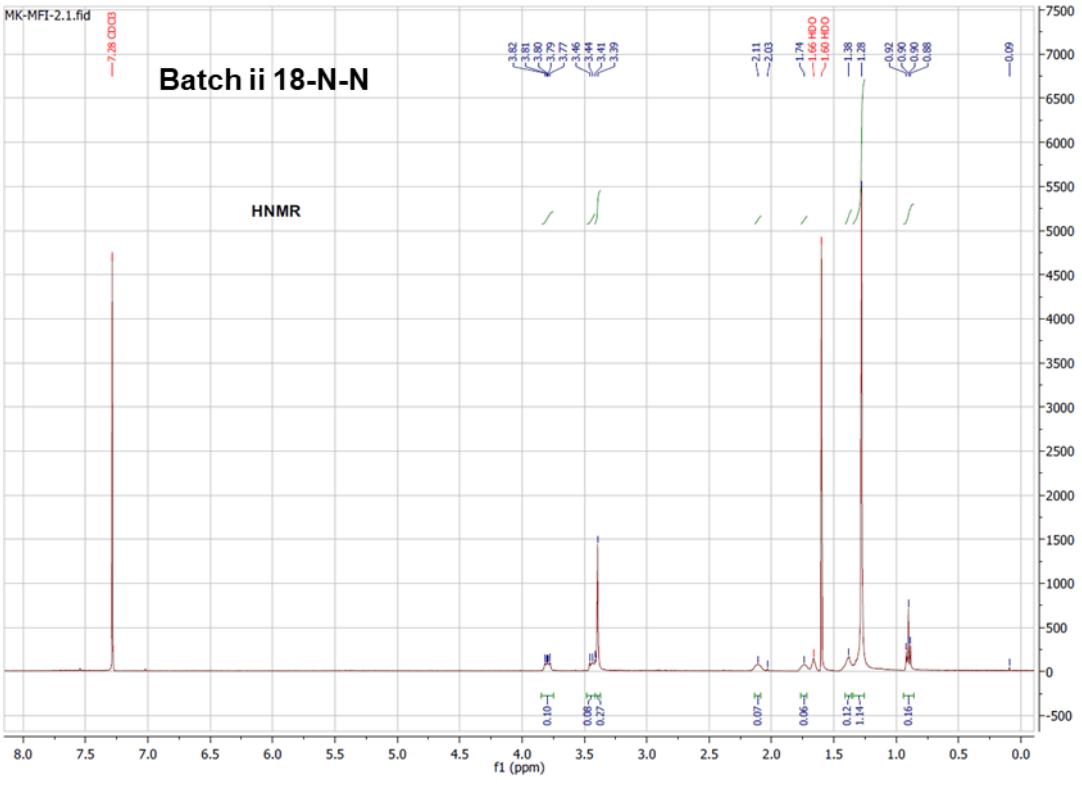
MK-MFI-2.1.fid
Batch ii 18-N-N
HNMR
f1 (ppm)

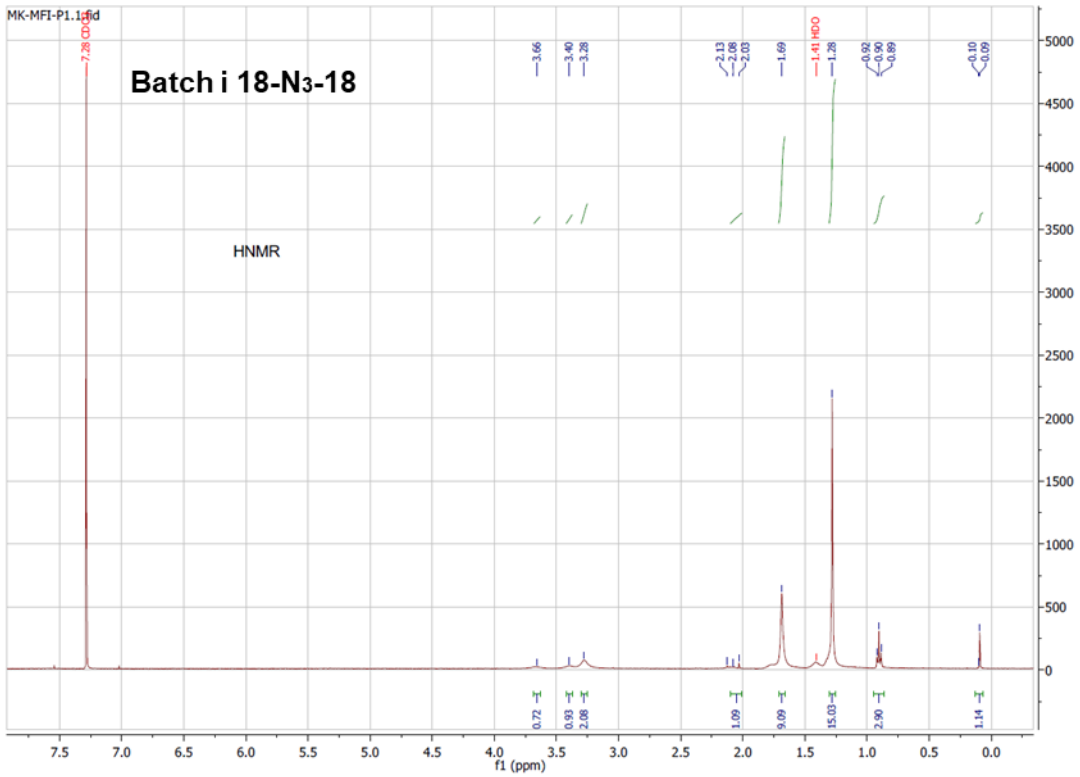

Figure s2. Liquid state ^{1}H NMR spectra of batch i and ii 18-N-Br and 18-N-N, as well as batch i of 18-N_3-18.

Appendix C: Optimized EFALs' calculated vibrational spectra

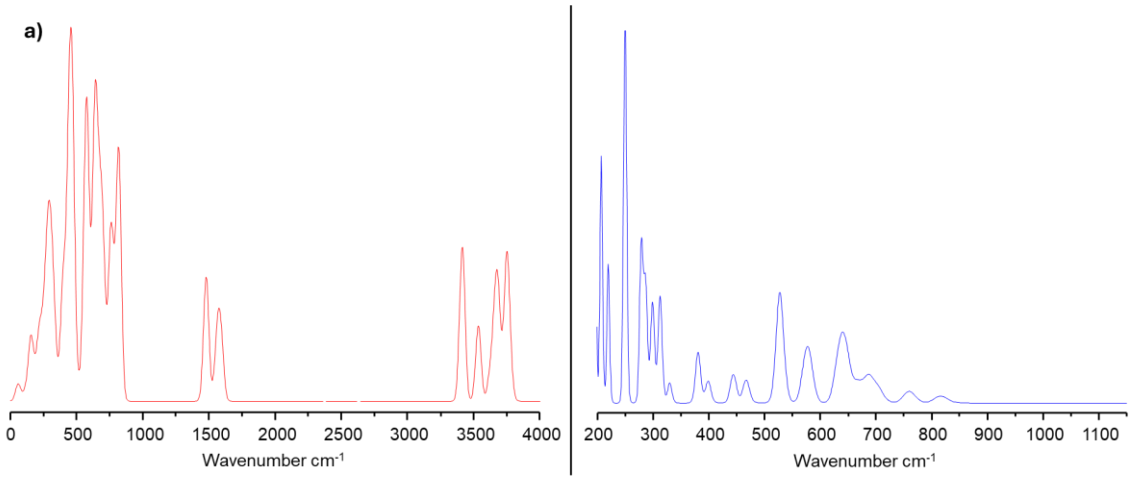

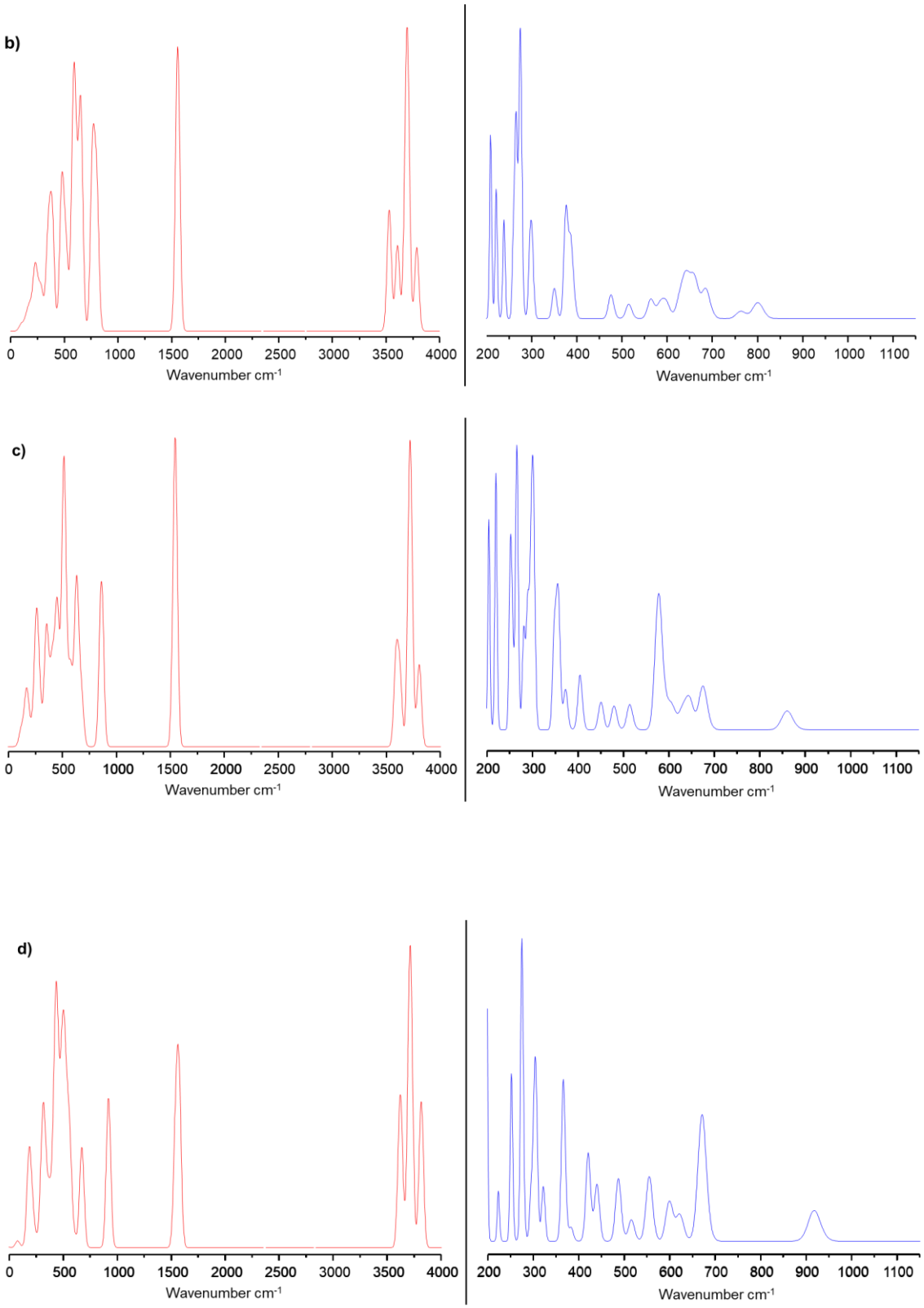
b)
0 500 1000 1500 2000 2500 3000 3500 4000
Wavenumber cm-1
200 300 400 500 600 700 800 900 1000 1100
Wavenumber cm-1
c)
0 500 1000 1500 2000 2500 3000 3500 4000
Wavenumber cm-1
200 300 400 500 600 700 800 900 1000 1100
Wavenumber cm-1
d)
0 500 1000 1500 2000 2500 3000 3500 4000
Wavenumber cm-1
200 300 400 500 600 700 800 900 1000 1100
Wavenumber cm-1

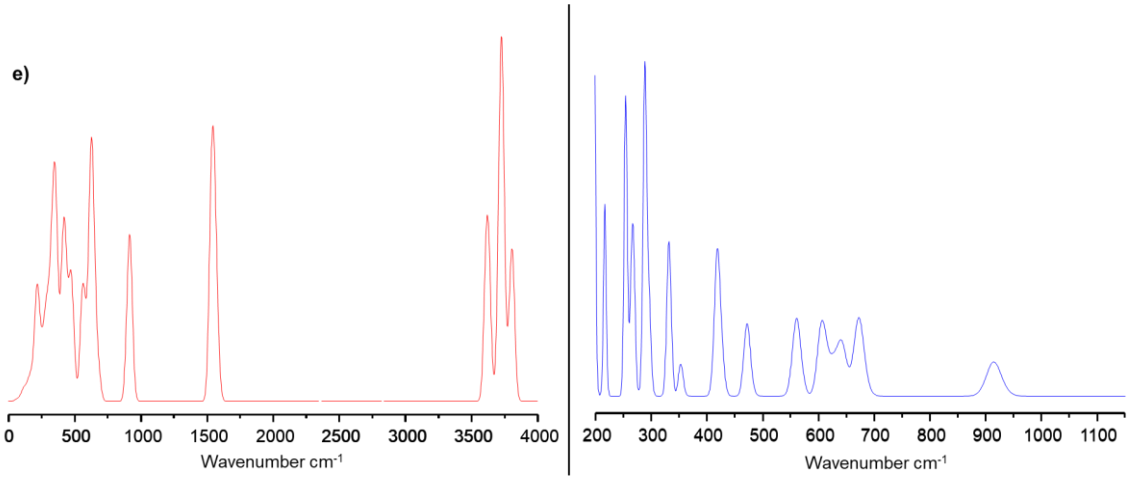
e)
0 500 1000 1500 2000 2500 3000 3500 4000
Wavenumber cm-1
200 300 400 500 600 700 800 900 1000 1100
Wavenumber cm-1

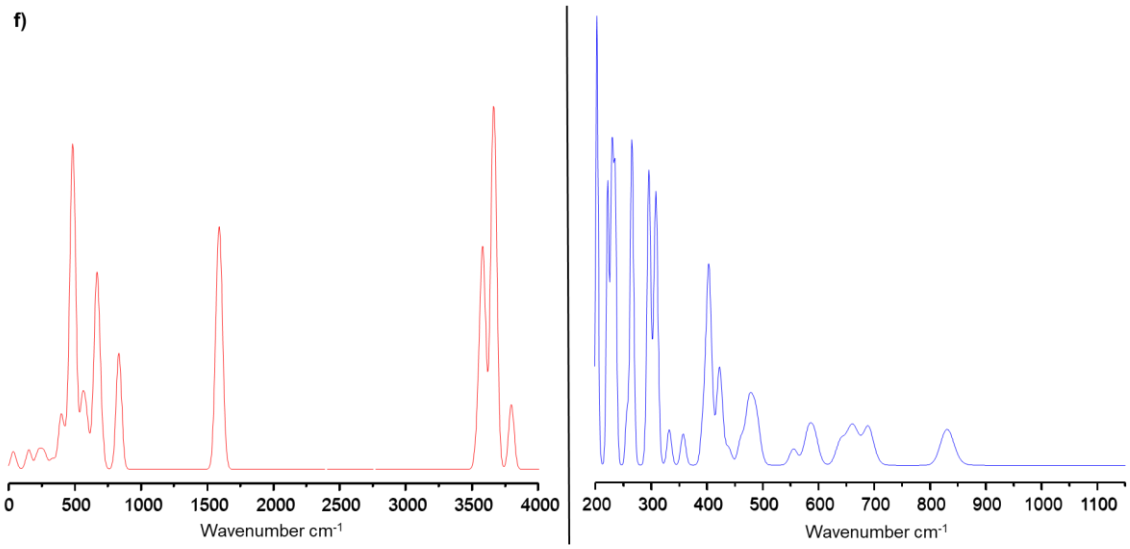
f)
0 500 1000 1500 2000 2500 3000 3500 4000
Wavenumber cm-1
200 300 400 500 600 700 800 900 1000 1100
Wavenumber cm-1

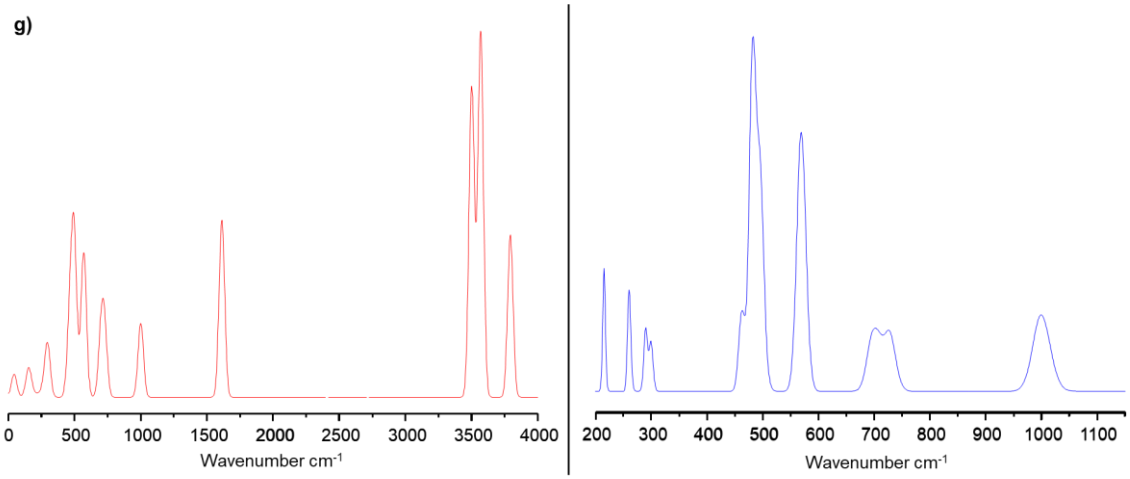
g)
0 500 1000 1500 2000 2500 3000 3500 4000
Wavenumber cm-1
200 300 400 500 600 700 800 900 1000 1100
Wavenumber cm-1

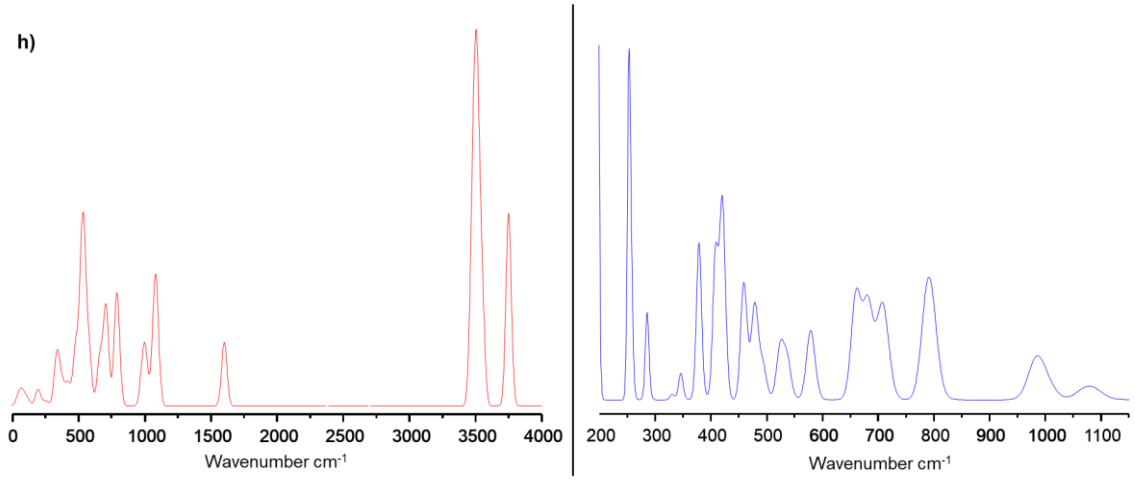

Figure s3. Calculated infrared (left side in red) and INS (right side in blue) of the EFAL structures: **a)** 0-octa**; b)** 1-octa**; c)** 1-octa trans**; d)** 1-penta**; e)** 1-penta trans**; f)** 2-octa**; g)** 2-tetra**; h)** 3